Determination of single molecule diffusion from signal fluctuations

Dissertation
zur Erlangung des Grades eines
Doktor der Naturwissenschaften

dem Fachbereich Physik der Universität Osnabrück
vorgelegt von

Susanne Hahne

Osnabrück, im Juni 2014

Contents

Chapter 1

Introduction

Functionalizing surfaces by deposition of adsorbates is a worthwhile method to improve a variety of components. Commonly known in this context are catalytic converters, which are mounted in every motor vehicle and steadily gain importance from an environmental point of view due to their capability to reduce exhaust fumes [1]. However, catalytic materials are often costly [2] and hence coating low cost bulk materials with effective adsorbates is a profitable alternative. While nanoparticles are usually sufficient for catalysis [3], full layers of adsorbate material can be utilized in other fields. The crucial factor during the miniaturization [4] of electronic components like organic thin film transistors [5] indeed was the ability to grow thin films with a thickness of only a few monolayers, which still have either insulating or conducting properties.

More recently, the self-assembly of single molecules has gained attention, especially in order to develop electronics based on molecular units. These include for instance molecular wires [6], junctions [7] and switches [8]. Such electronic devices are capable to overcome the physical limitations of conventional silicon technology [4] and furthermore increase computational speed [8]. Knowledge of the respective organic building blocks [9] improves the quality of the structures. In addition to experimental investigation of self-assembly of specialized structures [10] and molecules in general [11, 12], simulation techniques are widely used [13] to assist in finding fundamental properties.

Since adsorbates are usually deposited randomly on the surface in the first place [14], they have to undergo some kind of lateral rearrangement before they can shape the desired structures [15]. The necessary displacement can be caused by thermal activation [16, 17] or, for instance, be driven by variations in the particle concentration [18]. However, it will typically be a diffusive motion.

Apparently, lateral mobility of adsorbates in general and of molecules in particular is a vital property forming the basis of the described applications. Therefore, knowledge of diffusion properties, especially the diffusion coefficient and thus the activation energy, is indispensable for controlling and steering the adsorbates motion. Several methods are available to determine the diffusion coefficient of adsorbates on surfaces [19] and a short account of the most popular will be given in the following.

Common measurement methods

One of the first measurement techniques was the real time observation of a pointy metal tip surface via the field electron microscope (FEM) [20] yielding a spatial resolution of 25 Å [21]. Electrons are emitted from the tip and accelerated towards a fluorescent screen, due to a high electric field applied between both. Adsorbates on the tip significantly

change the local work function, causing shadows on the screen. Using the fluctuation method [22] instead of counting displacement steps by hand further increased the quality of the results.

Lateral resolution was further increased to 1 Å by introduction of the field ion microscope (FIM) [23]. The experimental setup is similar to the FEM, but the imaging is based on an inert gas in the apparatus. When a high electric field is applied, it ionizes preferably in the vicinity of surface atoms, where the electric field is stronger due to a locally higher curvature in the topography. The strength of the electric field is a delicate choice, because it has to be strong enough to ionize the gas, but must not detach the adsorbates. The measurement process itself is split into a recording phase, where the high electric field is applied, and a movement phase, where the electric field is turned off and the tip is heated allowing the adsorbates to move. The displacement can be tracked by subsequent images.

The Laser induced thermal desorbtion (LITD) technique [24] does not record the displacement directly. Here, a focused laser pulse is sent on a surface with a homogeneous concentration of adsorbates. In the area, where the laser beam irradiates the surface, adsorbates will desorb completely and the now empty area can only be reoccupied by neighboring adsorbates diffusing into it. After a certain idle period an identical second laser pulse again desorbs those particles, which entered the void zone in the meantime. The amount of desorbing particles depends on their diffusivity and is detected by a mass spectrometer [25].

Like all measurement techniques, the three methods described above are afflicted with certain weaknesses. Besides the risk of influencing the adsorbate's motion by the high electric fields, a drawback of the FEM as well as the FIM is the limited choice of probe materials, which are conducting, can be crafted into a tip and withstand high electrostatic fields. The LITD, though capable of investigating a variety of materials, is a rather invasive method, which can destroy the samples. With the dawn of the minimally invasive scanning tunneling microscopes (STM) [26] for conducting and atomic force microscopes (AFM) [27] for insulating samples, many of these problems were solved.

An STM consists of a point-like conducting tip, which is positioned at a fixed distance close to an also conducting surface. A small voltage is applied and though electrons can not cross the gap between tip and surface they can tunnel through the potential barrier. Since the tunneling probability is very sensitive to the gap width, the electronic topography of the surface will cause variations in the tunneling current. An alternative mode of operation is to set a constant tunneling current and reconstruct the electronic surface structure from the necessary adjustments of the positioning control.

The AFM technique uses a cantilever with a tip on one end, which is positioned close to the surface. In contact mode its bending due to attractive or repulsive interaction with the surface can be used to keep the cantilever at a constant height above the surface thus recording the surface topography via the necessary elevation adjustments. In non-contact mode the tip oscillates with its resonance frequency close to the surface without touching it. Different forces affecting the tip, i.e., variations in the surface structure, are then identifiable as changes in the resonance frequency.

When recording subsequent images of a surface with adsorbates the basic principle of counting the displacements can be directly applied to determine the diffusion coefficient [28]. An indirect approach is to employ the dependency of island sizes on flux, critical nucleus size and diffusion coefficient [29, 30] for determining the latter. This principle is also expandable to multicomponent systems [15, 31]. Yet, the evaluation of island sizes calls for large defect free areas on the surface allowing multiple islands to form.

State of the art STM techniques are capable of a video mode [32] and thus a real time tracking of adsorbate paths [33]. However, molecules in organic surface growth often have high mobilities causing noise instead of clear images [34, 35] due to the strongly limited time resolution of 25 frames per second for STM [32] and about 1 frame per second for AFM [36] in these modes of operation.

Recording of signal fluctuations with a locally fixed tip

A more convenient approach is the recording of temporal fluctuations with a locally fixed probe, for instance current fluctuations in an STM, which enables a strongly increased time resolution. The goal of this work is the development of evaluation methods that allow the determination of diffusion coefficients of non-point-like adsorbates on the basis of such signal fluctuations. This includes absolute values for isotropic translational as well as rotational diffusion coefficients. Furthermore, anisotropic translational diffusion should become identifiable.

Different means are conceivable to extract the diffusion coefficient from the detection events in a time series. Originally, the autocorrelation function of the recorded signal has been the focus of experimental [37] and theoretical [38] studies. However, diffusion coefficients of adatoms can only be determined up to a proportionality factor with these ACF methods. Therefore, no absolute values of the diffusion coefficients are accessible and only relative changes can be obtained, for instance when varying the temperature.

In this work, the autocorrelation function is adjusted to molecules with sizes larger than the step length of translational moves. This way absolute values of the diffusion coefficient become available. Furthermore, the distribution of peak widths [39] is revisited and a more detailed theoretical treatment is developed. The evaluation of the distribution of interpeak intervals is introduced as a third alternative here. It is based on the motion outside of the probes vicinity, while the former two approaches might be influenced by molecule probe interactions.

Considering the circular shapes of molecules widely used for self-assembly studies, see Fig. 1.1 (a)-(c), in chapter 3 a first account on the evaluation methods is given for translational movement of circular shaped molecules. However, other molecules can be better described by rectangular shapes, see Fig. 1.1 (d)-(f). Therefore, in chapter 4 adjustments to the methods accounting for rectangular molecules are presented.

Upon deposition, molecules are often spread with an arbitrary orientation on the surface. With increasing coverage they will eventually rotate to form an ordered layer [40, 41]. While these reorientation steps will be scarce for molecules with only two preferred orientations [42], there are material combinations that allow a strong rotational movement of the molecule around its center of mass [43, 44, 45]. For rectangular shaped molecules this additional degree of freedom causes different fluctuation patterns in the signal. To cope with the additional degree of freedom and possibly determine the rotational diffusion coefficient, the methods described above are further extended in chapter 5.

Diffusion in general can be anisotropic. For the investigated motion of molecules on surfaces reasons include for example an asymmetric molecule structure [46] or an anisotropic surface structure [47] amongst others. While this might be hindering in some cases, it can also be exploited for steering self-assembly of structures on the surface [48] or directional transport of material [49]. In any case it is helpful to quantify such a behavior. Since they do not contain information on the molecules' paths, abstract methods like the analysis of island size distributions or the laser induced thermal desorption are not

qualified to resolve anisotropic diffusion at all. Strobe like imaging of the surface and subsequent analysis of the displacement of single objects, would have to be extended to additionally record the direction of the displacement to get an impression of a molecule's preferred direction. The same applies to video-based evaluation methods, but in both cases it is expected to be rather extensive.

In this work it is discussed that also the recording of signal fluctuations from a locally fixed probe, which is convenient for resolving isotropic diffusion, is not universally suited to identify anisotropic motion. However, with different measurement setups, which can be simulated by letting a probe oscillate on simple trajectories, this deficit can be eliminated, as presented in chapter 6 along with the corresponding evaluation methods.

Application of methods

All evaluation methods are first validated against substitute kinetic Monte Carlo simulation data, according to the model described in chapter 2. The advantage of simulating a system is the possibility of choosing various parameter sets. As a result, experimental prerequisites can be defined in chapter 3 and the methods presented in this work can be tested thoroughly, even for extreme parameters, that would be difficult to obtain in an experiment.
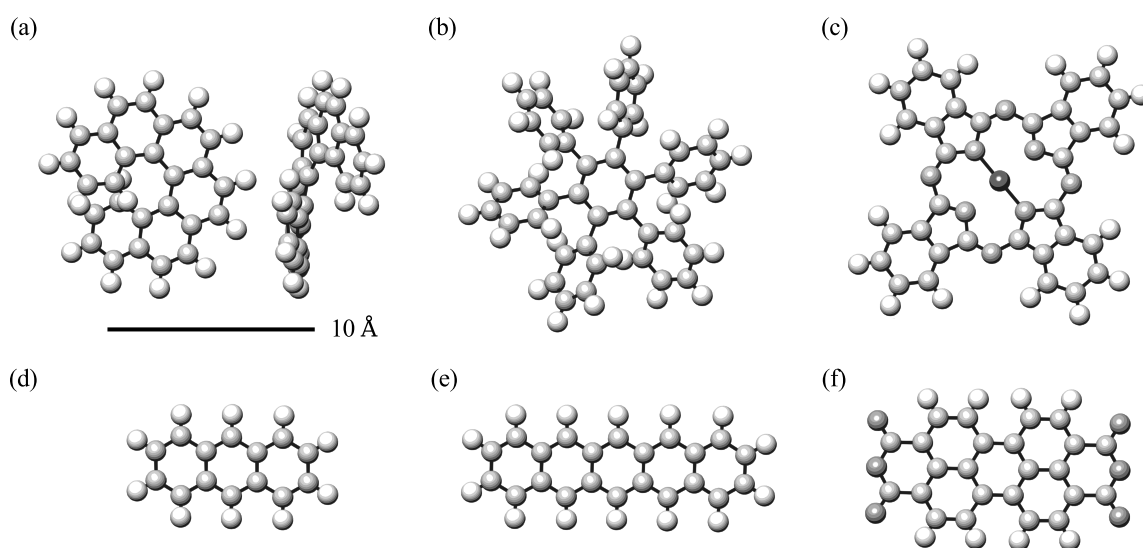
Figure 1.1: Ground-state vacuum structures obtained from density functional calculations of several molecules. They can be considered as representative for classes of derivates that are widely used in studies of molecular self-assembly on surfaces: (a) helicene [50] (top and side view), (b) hexaphenylbenzene [51], (c) (copper-) phthalocyanine [52], (d) pentacene [53], (e) anthracene [54, 55] and (f) the perylene derivate PTCDA [56]. Images of the molecules in the respective studies suggest, that their overall shape is not significantly distorted upon adsorption and that they often lie flat on the surface.

Eventually, the presented methods are successfully applied to determine the diffusion coefficients of copperphthalocyanine (CuPc) and PTCDA on Ag(100) from experimental measurement data [57] in chapter 7. Though STM and AFM are the obvious experimental choice, because they are most likely already present in every laboratory working in the field of surface science, the evaluation methods are deliberately kept on an abstract level and can in principle be applied to any point-like probe.

Chapter 2

Kinetic Monte Carlo simulation

The ongoing increase of available computing power allows to effectively simulate the behavior of even complex physical systems. However, it is still difficult to include all interactions and possible processes contributing to a system in a simulation. Therefore, the employed simulation technique is chosen according to the particular property of interest. For example, there are powerful tools to calculate the spatial and electronic structure of single [58] or multiple molecules, as well as periodic arrangements in crystal-like structures [59, 60]. In addition a variety of Monte Carlo simulations is available, which are well suited for simulating the dynamics of molecules on a surface. "Monte Carlo" is a category name for various simulation techniques, whose mutuality is that they change the status of a system in a stochastic manner. A prerequisite is that for any given state the transition rates to other states are known.

2.1   Model

In this work a Monte Carlo simulation of extended objects diffusing on a two-dimensional grid is employed to simulate molecules diffusing on a surface. Translated to this simulation a state of the system is an accumulation of molecule positions. A transition to another state is performed, whenever an object moves. To account for the time dependence, the simulation follows the the principle of a Kinetic Monte Carlo simulation [61], which assumes that the probability distribution of the time Δt from now, when the next transition will occur, i.e., $P_{\text{next}}(\Delta t)$, is given by a Poisson process

$$P_{\text{next}}(\Delta t) = \exp\left(-\omega_{\text{tot}}\Delta t\right) , \tag{2.1}$$

where ω_{tot} is the cumulative rate of all possible transitions. In case of diffusion the rates are proportional to the respective diffusion coefficient D_i [62]. The waiting time between two transitions is then defined as

$$\Delta t = -\frac{1}{\omega_{\text{tot}}} \log(z_{\text{time}}) , \tag{2.2}$$

and is randomly drawn via an equally distributed random number $z_{\text{time}}(\in \mathbb{R})$ between zero and one [61]. If the random number generator yields $z_{\text{time}} \in [0, 1[$, $\log(1 - z_{\text{time}})$ can be used to avoid the singularity at 0 without loss of generality. Generally, the transition rates could be different for each state. However, a fixed number of non-interacting objects will be considered here, hence the rates are constant.
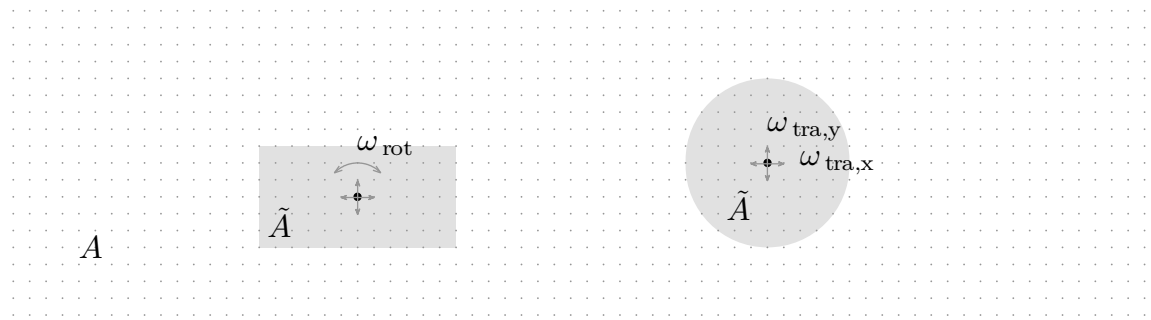
Figure 2.1: Sketch of the simulation's geometry: The square lattice of size A defines possible object center positions (small dots). Objects are defined by their center position (bold dots) and extent $\tilde{A}$ (shaded areas). Allowed transitions are indicated by the arrows.

The object's position is defined by its center coordinates, and in case of non-circular objects they are additionally given an individual orientation. The center positions of the objects in the simulation perform jumps between nearest neighbor lattice sites on a two-dimensional grid of size A, see Fig. 2.1. The lattice constant is set to $a = 1$ and the system proportions are kept by defining the object size as multiple of the lattice constant. For example, the simulation radius R of an object with radius $\tilde{R}$ is given by $R = \tilde{R}/a$. The number N of objects on the grid follows from the number density $c = N/A$. It is connected to the widely used surface coverage θ_0, given in percent of a monolayer, via the surface area covered by a single object $\tilde{A}$

$$c \equiv \frac{\theta_0}{\tilde{A}}. \tag{2.3}$$

The lattice used in the simulation should have a size large compared to the single object to avoid finite size effects. However, N linearly increases with the lattice size. To maintain a reasonable size of the whole system, a lattice of $A = 1000 \times 1000$ positions is chosen with periodic boundary conditions to emulate an even larger system.

In case of pure translational movement, which will be discussed in chapters 3 and 4, the objects are displaced on the square lattice with stepsize a and a rate of $\omega_{\text{tra}} = 4D/a^2$. Here, the objects orientation φ and its rate for rotational moves is set to zero by default. When including rotational movement as done in chapter 5, reorientation moves with a step size of a_φ and rate $\omega_{\text{rot}} = 2D_\varphi/a_\varphi^2$ are additionally taken into account. The anisotropic diffusion in chapter 6 is realized with different jump rates $\omega_{\text{tra},x} = 2D_x/a^2$ and $\omega_{\text{tra},y} = 2D_y/a^2$ along the principal axes of the diffusion tensor, which coincide with the x- and y-axes here. The total rate necessary to calculate the waiting time [cf. Eq. (2.2)] is derived from the sum over the rates of all contributing processes $\omega_{\text{tot}} = N \sum_i \omega_i$. The rates are weighted with N, because every object can perform every transition. The type of transition is chosen via another equally distributed random number $z_{\text{type}} \in [0, 1[(\in \mathbb{R})$:

$$
\begin{array}{rcll}
0 \leq & z_{\text{type}} & < \frac{N\,\omega_{\text{tra},x}}{\omega_{\text{tot}}} & \rightarrow \text{Translation in } x-\text{direction} \\[1mm]
\frac{N\,\omega_{\text{tra},x}}{\omega_{\text{tot}}} \leq & z_{\text{type}} & < \frac{N\,\omega_{\text{tra},x}+N\,\omega_{\text{tra},y}}{\omega_{\text{tot}}} & \rightarrow \text{Translation in } y-\text{direction} \\[1mm]
\frac{N\,\omega_{\text{tra},x}+N\,\omega_{\text{tra},y}}{\omega_{\text{tot}}} \leq & z_{\text{type}} & < 1 & \rightarrow \text{Rotation}
\end{array}
$$

Note that the first two cases merge if $\omega_{\text{tra},x} = \omega_{\text{tra},y}$. The direction of displacement is also set randomly between $\pm a_\varphi$ for rotation as well as $\pm \binom{a}{0}$ and $\pm \binom{0}{a}$ for translation.

Other orientations of the principle axes can be easily implemented by changing these displacement vectors.

Various sets of parameters, which will be called configurations in the following, were simulated for this work in order to test the simulation as well as the evaluation methods. Yet, only an assortment of those configurations, which characterize the investigated property best will be presented in respective discussions. The underlying parameter sets are filed in appendix C and will in the following be adressed as Conf. `C01`, for example.

It has to be noted that the assumption of non-interacting objects is a simplification, which nevertheless should be appropriate for freely diffusing molecules at low coverages. Formally, more than one object could cover the detection site in the simulation, due to the neglect of interactions. Since most probably their arrival and departure times will not be synchronous, the recorded peak width would be elongated. However, an overlap at the detection site is unlikely for small coverages and hence does not significantly falsify the simulation. Considering the probability $P_1 = \tilde{A}/A$ that a given object covers the detection site, the binomial distribution can be employed to calculate the probability $P_{>1}$ that more than one object will cover it $P_{>1} = 1 - \sum_{k=0}^{1} \binom{N}{k} P_1^k (1 - P_1)^{N-k}$.

In the simulations a coverage of $\theta_0 = 1\%$ is used, which is about the upper limit of effective coverage values found in experimental setups, cf. chapters 7.2 and 7.3. For example, Eq. (2.3) yields $N = 100$ particles of size $\tilde{A} = 10 \times 10$ on a $A = 1000 \times 1000$ grid. This results in a probability of $P_{>1} = 5 \times 10^{-5}$ to find more the one object at the detection site in the moment of observation. While recording 10^5 peaks the detection site is typically observed 5×10^7 times, of which the probe site is occupied by multiple objects 10^2 times according to $P_{>1}$. Assuming the worst case, where each of the 10^2 occurrences elongates another peak, this consideration results in a maximal error of $1\text{\textperthousand}$ falsified peaks. Due to lower coverages, this negligible error usually is even smaller, especially if not considering the worst case scenario.

2.2 Implementation

The simulation is implemented in C++ [63] following the principles of object-orientation. The Mersenne Twister [64] is used as the pseudo random number generator. It is very fast and passes most randomness tests [64]. Futhermore, the count of random number draws per simulation run (max. 1×10^{10} for Conf. `A00`) is well below the Mersenne Twister's periodicity of $2^{19937} - 1 \approx 10^{6001}$. One of its few disadvantages is, that depending on the initial value, several draws might be necessary before a sufficient randomness is achieved [64], which is considered in the implementation. Depending on whether circular or rectangular objects shall be investigated, the diffusing objects are instances of the `CircularObject` or the `RectangularObject` class. If not stated otherwise, the simulated signal is recorded at the position of a `FixedTip` instance.

After parameter declaration and initialization, N identical objects are spread randomly on the grid. The repeating part of the simulation consists of the following steps. First the time is increased by the waiting time [Eq. (2.2)]. Then an object is chosen randomly and moved as described in the model section. Afterward the moving object checks, if it covers the tip position. If so, the signal is set "on". Else, if none of the other objects covers the detection site, it is set "off". The pseudocode reads as follows:

```
while not enough events recorded
    increase time by waiting time
    choose random object
    move this object
    if tip position is covered
      set signal on
    else
      set signal off
    end if
    if signal toggled from 'on' to 'off'
      increase number of events
    end if
end while
```

In chapter 6 a modification is investigated, where the probing site is no longer locally fixed. Therefore, also the `CircularMovingTip` and `LinearMovingTip` classes have been implemented, which inherit from `FixedTip` and can additionally update their own position. The situation with moving tips is much more elaborate, because the signal is no longer toggled only by an object moving, but also by the tip entering or leaving a standstill object. This is best captured by strobe-like reading the system in constant time steps, rather than increasing the time by the current waiting time. It is very close to the experimental situation, where a discrete rather than a continuous time signal is recorded, compare for example [39]. One way to capture the objects' motion is to continuously compare the actual system time with the next event time and letting one random object move when the waiting time has passed. Another possibility is to let all objects move a corresponding fraction of the stepsize in every time step. Since there are no significant runtime differences between these two options, the first was used, because of its affinity to the static tip implementation. The pseudocode in this situation is altered to:

```
while not enough events recorded
    if any object covers tip position
      set signal on
    else
      set signal off
    end if
    if signal toggled from 'on' to 'off'
      increase number of events
    end if
    while next event time < next time step
      choose random object
      move this object
      update event time
    end while
    increase time step
    update tip position
end while
```

An illustration of the classes with their key attributes and all dependencies is given in the UML class diagram [65] depicted in Fig. 2.2.
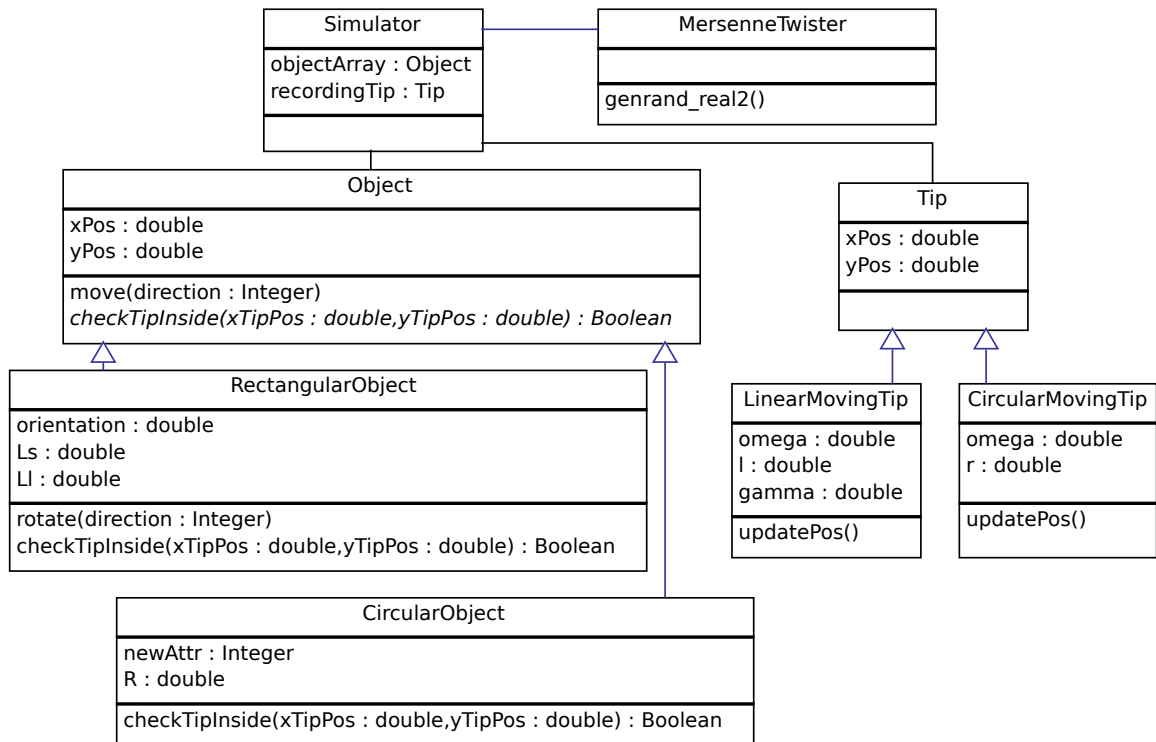
Figure 2.2: An UML class diagram of the simulation program. A molecule diffusing on a surface is represented by a two-dimensional `Object` randomly changing its center position on a grid. Time dependencies and random choices according to chapter 2 are controlled by the `Simulator` and its `MersenneTwister`. The signal is recorded at a well defined probe site marked by a `Tip`.

2.3 Optimization

Several optimizations are possible to increase the performance of the simulation. While mandatory improvements, like avoiding unnecessary branching and loops, will not be discussed in detail here, two steps to decrease memory load and runtime of the program to a fraction are to be singled out.

First, the size of the signal in terms of output data can be massively reduced, if only those times, when the signal toggles from "on" to "off" or vice versa, are written out. Regarding the evaluation via residence time distribution (cf. chapters 3.2 and 4.2) and interpeak time distribution (cf. chapters 3.3 and 4.3), the residence times and interpeak intervals respectively can even be directly written out.

Secondly, the simulation allows to position several tips in the system, which can each record a signal of its own. Residence times and interpeak intervals of all signals can be joined afterward. The autocorrelation function on the contrary must be calculated from a single signal. However, this is no hindrance, since compared to both distributions only a fraction of recorded events is necessary for a smooth autocorrelation function, cf. chapter 3.4. For an optimal simulation a balance has to be found between decreasing the runtime by parallel recording with multiple tips and increasing it, due to the additional hit tests. For the system size used throughout this work, four independent recording tips have turned out to deliver the best results.

Chapter 3

Circular shaped objects

As pointed out in the introduction, this work presents three different approaches to extract the diffusion coefficient from signal fluctuations of a locally fixed probe, regardless whether the signal was recorded in an experiment or consists of substitute simulation data. In the theoretical derivations the recording probe is considered as a fixed point on a two-dimensional surface called "probe site". Detailed information on the method of measurement method is not needed for the theoretical treatment in this work.

The surface is envisioned to be covered by N indistinguishable, non-interacting objects with a lateral extent $\tilde{A}$ representing the molecules. To begin with, a circle with radius R is assigned to the surface area $\tilde{A}$ covered by the object, compare sketch in Fig. 3.1, which is an appropriate geometric representation for many molecules used in surface science, see Fig. 1.1 (a)-(c). The signal recorded at the probe site is either "on" or "off", depending on whether it is covered by one of the diffusing objects or not. Until the effects of anisotropic motion are investigated in detail in chapter 6, the objects are presumed to diffuse isotropically with a diffusion coefficient D.

The evaluation methods are first validated against simulation data, according to chapter 2. Application of the three methods to real measurement data is presented in chapter 7.

Figure 3.1: Sketch of a circular object's geometry with its radius R in (a) the RTD and (b) the ITD setup. In both cases the dot marks the probing site and the shaded area is the so-called detection area, defined by those object center positions that turn the signal "on". The dotted line marks the initial probability distribution displaced by Δ_R from the absorbing boundary, see text, which is used for Eqs. (3.9) and (3.13).

3.1 Autocorrelation function

For the autocorrelation function (ACF) the fixed probe position marks the center of a two-dimensional x-y-coordinate system on the surface. Each of the objects (μ) diffusing on the surface can be addressed by its center position $\mathbf{r}_\mu(t) = [x_\mu(t), y_\mu(t)]$. The signal recorded at the probe site is the sum over the contributions of each object

$$S(t) = \sum_{\mu=1}^{N} s_\mu[\mathbf{r}_\mu(t)] \,, \tag{3.1}$$

where $s_\mu[\mathbf{r}_\mu(t)]$ can be interpreted as a "detection function", specifying how strong the probe will sense an object at this position. The autocorrelation function of the signal is given by

$$C(t) = \langle S(0)S(t) \rangle \,. \tag{3.2}$$

The objects are supposed to be independent. Furthermore, in the evaluation of the ACF only times $t \ll \tau_R \equiv R^2/D$ will be considered, where τ_R is comparable to the mean residence time of the object center at the probe site. This way, it can be assured that only one particle will contribute to the signal on this time scale and the cross-correlation terms between different objects become negligible. The ACF is then reduced to the self-correlator $C(t) = N \langle s(0)s(t) \rangle$, which can be expressed by

$$C(t) = \frac{c}{4\pi D t} \int \mathrm{d}\mathbf{r}_0 \int \mathrm{d}\mathbf{r}_1 \; s(\mathbf{r}_1) \; \exp\left(-\frac{(\mathbf{r}_1 - \mathbf{r}_0)^2}{4Dt} \right) \; s(\mathbf{r}_0) \,. \tag{3.3}$$

For details of the derivation, please consult appendix A.1.

The explicit form of the detection function depends on the measurement technique. Regarding an STM, for example, the change of the tunneling current by a foreign object in the tunneling gap between probe and surface has to be determined. The tunneling problem itself has long been treated, e.g., by Tersoff and Hamann [66]. Sumetskii and Kornyshev suggested a Gaussian shaped detection function for diffusing atoms [38]. If the diffusing object has a non-negligible lateral extent, which is the case for molecules, its detailed structure and electronic charge density need to be taken into account. This degree of detail, however, is not necessary for a reasonable evaluation of the ACF of a simplified signal.

It has turned out to be sufficient only to distinguish between "on" and "off" states in the signal [†]. The probe is turned "on" whenever part of any diffusing molecule covers the detection site and goes "off" as soon as this site is uncovered again. This concept results in a rectangular detection function

$$s[\mathbf{r}(t)] = \begin{cases} 1 & \text{if } \mathbf{r}(t) \in \mathcal{D}, \\ 0 & \text{else}, \end{cases} \tag{3.4}$$

where $\mathcal{D}$ is the set of those center positions, that cause the object to cover the probe site. $\mathcal{D}$ will be referred to as the detection area. Note that the overall signal [Eq. (3.1)] is also a rectangular signal with amplitudes either 0 or 1, because only one particle is in the vicinity of the probe on the examined time scales.

The autocorrelation function of a continuously recorded signal is given by the convolution

$$C(t) = (f * f)(t) = \int \mathrm{d}\tau f(\tau) f(\tau - t) \,, \tag{3.5}$$

which can be quite extensive to calculate. A more convenient method is to make use of the convolution theorem [67], which states that a convolution becomes a simple multiplication in the Fourier space

$$C(t) = \mathcal{F}^{-1}\left(\mathcal{F}\left(f * f\right)\right) = \mathcal{F}^{-1}\left(\mathcal{F}\left(f\right)\mathcal{F}\left(f\right)\right) . \tag{3.6}$$

This principle also applies to signals recorded in discrete and constant time steps. Here a Fast Fourier Transformation algorithm [68] can be used for the transformation steps.

For a quantitative evaluation of simulated data, the set $\mathcal{D}$ has to be adapted to the object's geometry. Here, circular objects are to be considered and hence a circle has to be assigned to $\mathcal{D}$. The right hand side of Eq. (3.4) then is given by $\Theta(R - |\mathbf{r}|)$ with the Heaviside jump function $\Theta(.)$ and the objects radius R. In this case Eq. (3.3) yields

$$C(t) = 4\pi c \int_0^R \mathrm{d}r_0 \ r_0 \int_0^R \mathrm{d}r_1 \ r_1 \frac{\exp\left(-\frac{r_0^2 + r_1^2}{4Dt}\right)}{4Dt} I_0\left(\frac{2r_0 r_1}{4Dt}\right) , \tag{3.7}$$

where $I_0(.)$ is the modified Bessel function of zeroth order. The function will approach the signal's expectation value $C(0) = c\pi R^2$ for $t \to 0$ and a power law $\propto t^{-1}$ in the long time limit, as is accounted for in appendix A.6.1. The latter, however, is irrelevant for the application, because it emerges for times larger than the mean residence time τ_R for a circular object, where the theory does not apply. The general behavior of the ACF is shown in Fig. 3.2.
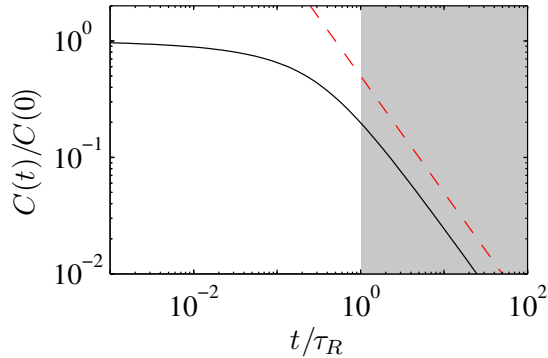
Figure 3.2: General behavior of the ACF [Eq. (3.7)] for a circular object with $R = 10$ and $D = 0.25$ (solid line). For $t \to 0$ it approaches the signal's expectation value $C(0)$ and for $t \gg \tau_R$ a power law $\propto t^{-1}$ emerges (indicated by the dashed line). The shaded area represents the time regime $t > \tau_R$, where Eq. (3.7) fails to apply and which hence is not used for evaluation in the following, see text.

Application to simulation data

The simulation, as described in chapter 2, writes out only those times, when the signal will change, hindering a direct calculation of the ACF via FFT. However, alternative means to determine the ACF are easily found as presented in appendix B.1. Since the time axis of the simulation results will scale with the input diffusion coefficient, simulation of different diffusion coefficients will yield no further information. Different object radii, e.g. $R = 5$ (Conf. C01) and $R = 10$ (Conf. C02), however, should influence the time series.

Non-linear least-square error fitting of Eq. (3.7) within the valid time regime $t \ll \tau_R$, $t \leq \tau_R/4$ to be precise, to the processed signals is done with a Levenberg Marquardt algorithm [69, 70], with the diffusion coefficient D as free parameter. As shown in Fig. 3.3 the fitting results (solid lines), match the simulation data (symbols) very well. The resulting diffusion coefficients are $D = 0.27 \pm 0.02$ and $D = 0.22 \pm 0.02$ respectively, which is in good agreement with the input value of $D_{\mathrm{in}} = 0.25$.

Figure 3.3: Two representative ACFs for objects of size (a) $R = 5$ (Conf. C01) and (b) $R = 10$ (Conf. C02) marked by symbols. The result of fitting Eq. (3.7) to the data is given by the solid lines. A good agreement within the time regime $t \leq \tau_R/4$ is visible. The resulting diffusion coefficients are (a) $D = 0.27 \pm 0.02$ and (b) $D = 0.22 \pm 0.02$.

3.2 Residence time distribution

The residence time distribution (RTD) is determined by sampling the time intervals between entrance and exit of an object's cente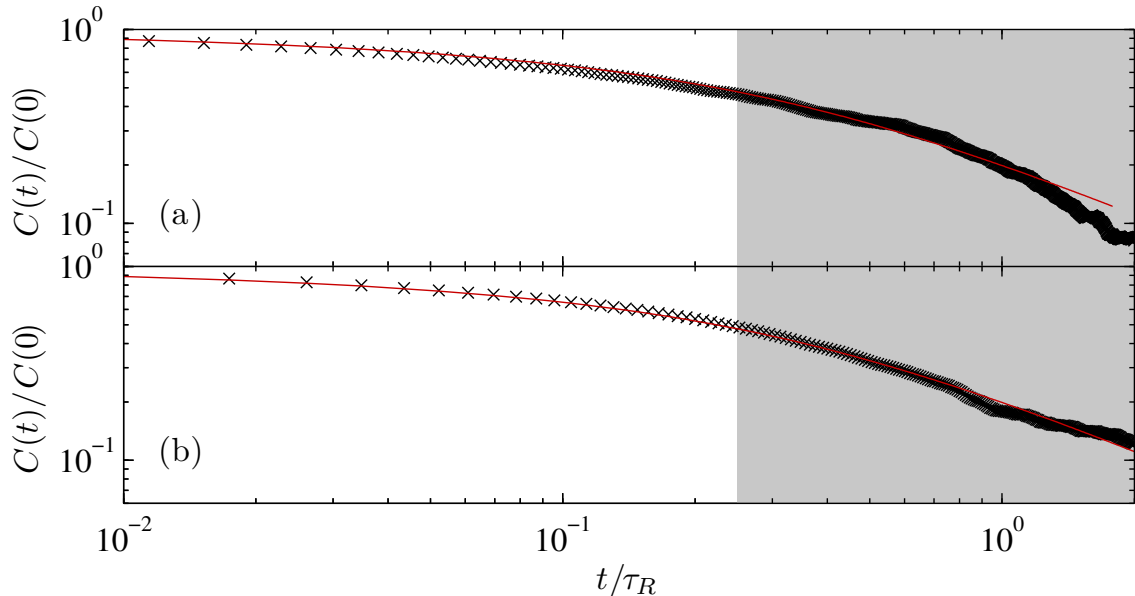r into the detection area $\mathcal{D}$. For its theoretical description here, the problem of a point-like particle diffusing inside a circle with absorbing boundaries, see Fig. 3.1 (a), has to be treated [†]. The initial probability density should be as close to the absorbing boundary as possible to represent the entering object. However, to get a non trivial solution it will be distributed along a circle at a distance Δ_R from the boundary in shape of a delta function $\delta(r - (R - \Delta_R))$. The length Δ_R could be associated to the elementary step size of the object. Due to the symmetrical initial condition in this case, the probability density for the objects center position $\mathbf{r}$ at time t depends on $r = |\mathbf{r}|$ only and is given by

$$p(\mathbf{r}, t) = \sum_{n=1}^{\infty} \frac{J_0(\chi_n r/R)}{\pi R^2} \frac{J_0[\chi_n(1 - \Delta_R/R)]}{J_1^2(\chi_n)} \exp\left(-\frac{\chi_n^2 t}{\tau_R}\right), \qquad (3.8)$$

where $J_\nu(.)$ are the Bessel functions of order ν, and the χ_n are the (positive) zeros of J_0, $J_0(\chi_n) = 0$ with $0 < \chi_1 < \chi_2 < ...$. Equation (3.8) as the solution of the diffusion equation with these particular initial and boundary conditions has been derived in the literature before using the Heaviside method [71]. A derivation based on separation of variables and eigenfunction expansions is given in appendix A.3.

With the probability distribution from Eq. (3.8) the calculation of the RTD follows standard techniques, as, for example, described in reference [72]. The probability that the object center has not left the circle until time t is $\Phi(t) = 2\pi \int_0^R \mathrm{d}r \, r p(\mathbf{r}, t)$. The probability that it leaves the circle in the time interval $[t, t + \Delta t]$ is $\Phi(t) - \Phi(t + \Delta t)$, implying that the probability density $\psi(t)$ for the residence time t is $\psi(t) = -2\pi \partial_t \int_0^R \mathrm{d}r \, r p(\mathbf{r}, t)$. With

Eq. (3.8) this yields

$$\psi\left(t\right) = \frac{2}{\tau_R} \sum_{n=1}^{\infty} \chi_n \frac{J_0\left[\chi_n\left(1 - \Delta_R/R\right)\right]}{J_1\left(\chi_n\right)} \exp\left(-\frac{\chi_n^2 t}{\tau_R}\right) . \tag{3.9}$$

Within the RTD distinct time regimes can be identified, as illustrated in Fig. 3.4. First note that with $\tau_{\Delta_R} \equiv \Delta_R^2/D$ there is a lower limit for the application of Eq. (3.9), because for smaller times the continuum treatment of the problem would have to be refined for discrete jump lengths. For larger times, that are still small compared to the typical time the object center needs to explore the detection area, a power law emerges

$$\psi\left(t\right) \propto \frac{1}{\tau_R} \left(\frac{t}{\tau_R}\right)^{-3/2} . \tag{3.10}$$

In this time regime, the ratio of the explored boundary section ($\propto t^{1/2}$) to the explored part of the detection area ($\propto t$) is proportional to the probability for the object center being next to the absorbing boundary. The (negative) time derivate of this probability $-\partial_t t^{-1/2} \sim t^{-3/2}$ then gives the time dependency of the efflux rate, which equals ψ. In Fig. 3.4 the ratio R/Δ_R is deliberately chosen high, so that the power law $\propto t^{-3/2}$ is well visible for $\Delta_R^2/D \ll t \ll \tau_R/\chi_1^2$. For parameters closer to experimental values, Δ_R and R are usually too close to fully unfold this time regime.

In the long time limit $t \gg \tau_R/\chi_1^2$, the functional behavior of Eq. (3.9) follows

$$\psi\left(t\right) \sim \frac{2}{\tau_R} \frac{\chi_1 J_0\left[\chi_1\left(1 - \Delta_R/R\right)\right]}{J_1\left(\chi_1\right)} \exp\left(-\frac{\chi_1^2 t}{\tau_R}\right) . \tag{3.11}$$

For those times, the occupation probability is spread over the whole circle and the efflux rate is essentially constant and given by the inverse of the typical time for the object center to reach the boundary. A Poisson process with this constant rate would yield $\psi(t) \sim \tau_R^{-1} \exp(-\text{const.}\, t/\tau_R)$. Derivations of the behaviors in the time regimes according to Eqs. 3.10 and 3.11 are given in appendix A.6.3
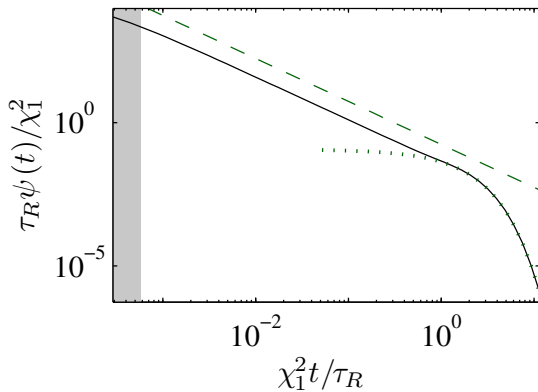
Figure 3.4: General behavior of the RTD [Eq. (3.9)] for a circular object with $R = 100, \Delta_R = 1$ and $D = 0.25$ (solid line). For $\tau_{\Delta_R} \ll t \ll \tau_R/\chi_1^2$ it follows a power law $\propto t^{-3/2}$ (indicated by the dashed line). For times $t \gg \tau_R/\chi_1^2$ the exponential decay used for fitting [Eq. (3.11)] is clearly visible (emphasized by the dotted line). The shaded area marks the lower limit τ_{Δ_R} for applicability of this theory.

Application to simulation data

In case of the simulation described in chapter 2, the residence times, i.e., the interval between an object center entering and leaving the detection area, are given out directly

and can be sampled subsequently. Since the residence times are spread over several orders of magnitude, a histogram with constant bin size is not the best for evaluation. More suitable approaches are the use of logarithmic spaced bins in the histogram or a sampling according to the procedure described in reference [73]. In the latter all residence times are sorted by their length and then a constant number n of events is combined per bin. The respective probability $p(t_i) = n/(N(t_{i+n} - t_i))$ of a bin follows from the normalization of the overall distribution.

The symbols in Fig. 3.5 show such distributions of residence times for two different object radii $R = 5$ (Conf. C01) and $R = 10$ (Conf. C02). To determine the diffusion coefficient D and the length Δ_R from a given RTD, Eq. (3.11) can be fitted to the exponential behavior for times $t \gg \tau_R/\chi_1^2$. In a self-consistency check it has been assured, that the tail regime used for fitting fulfills this requirement. The resulting diffusion coefficients are $D = 0.22 \pm 0.06$ (Conf. C01) and $D = 0.23 \pm 0.03$ (Conf. C02) for an input value of $D_{\text{in}} = 0.25$. For Δ_R a value of 1.8 is obtained for both Conf. C01 and Conf. C02, which is of the order of the lattice constant $a = 1$ used in the simulation. Inserting these D and Δ_R in Eq. (3.9) yields the full distribution, marked by the solid line in Fig. 3.5, which shows a good agreement with the underlying data in the time regime $t \geq \tau_{\Delta_R}$
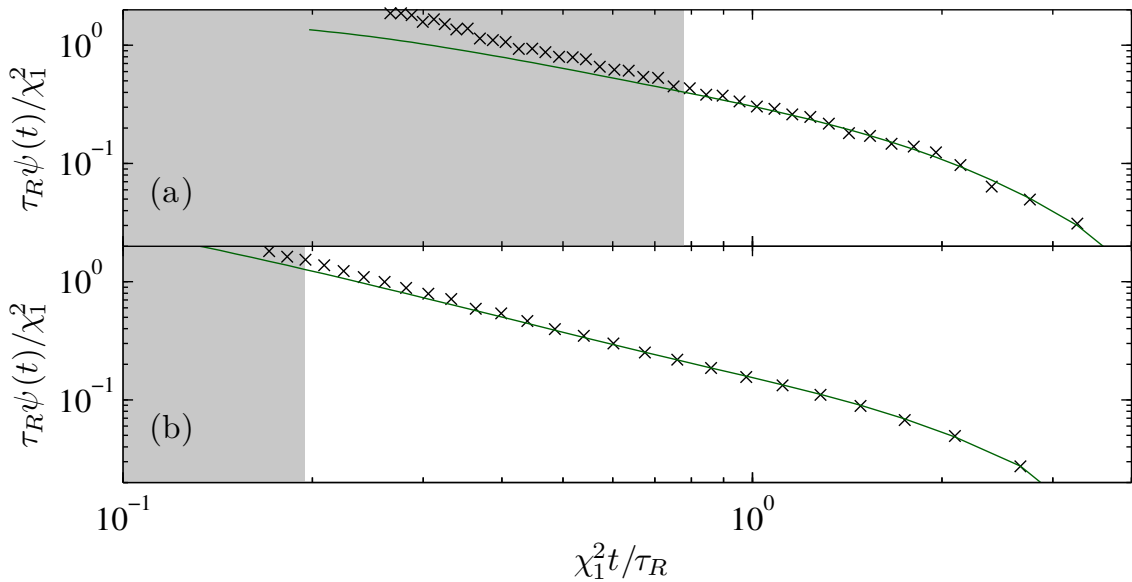
Figure 3.5: Representative RTDs (symbols) for two different object radii (a) $R = 5$ (Conf. C01) and (b) $R = 10$ (Conf. C02). Fitting of $t \geq \tau_R/\chi_1^2$ with Eq. (3.11) yields $D = 0.22 \pm 0.06$ and $\Delta = 1.8$ in (a) as well as $D = 0.23 \pm 0.03$ and $\Delta = 1.8$ in (b). The solid lines mark the full distributions according to Eq. (3.9), when using the fitted parameters. The shaded areas mark the short time regime $t \ll \tau_{\Delta_R}$, where the continuum treatment ceases to apply.

3.3   Interpeak time distribution

The interpeak time distribution (ITD) results from the sampling of the time intervals between the probe signal turning "off" and "on" again. The statistics of small interpeak times is dominated by exit and entrance of the same object into the detection area $\mathcal{D}$. For calculating the contribution of these return processes to the ITD, the diffusion of an

object center with initial distance Δ_R from an circular absorbing boundary with radius R, see Fig. 3.1 (b), has to be analyzed [†]. For the probability density of the object center to be at position $\mathbf{r}$ at time t

$$p\left(\mathbf{r}, t\right) = \int_0^\infty \frac{\mathrm{d}\chi}{2\pi R^2}\, \chi\, W_0\left(\frac{\chi r}{R}, \chi\right) \frac{W_0\left[\chi\left(1 + \Delta_R/R\right), \chi\right]}{J_0^2\left(\chi\right) + Y_0^2\left(\chi\right)}\, \exp\left(-\frac{\chi^2 t}{\tau_R}\right) \qquad (3.12)$$

is obtained with $W_0(x, y) \equiv J_0(x)Y_0(y) - J_0(y)Y_0(x)$, where $J_0(.)$ and $Y_0(.)$ are the Besselfunction of first and second kind. Details of the derivation are given in appendix A.3.

The ITD can be derived from the probability density analogously to the treatment of the RTD by taking the time derivate of the integral of $p(\mathbf{r}, t)$ over the outer area with respect to the circle. In the present case it is more convenient to take the flow through the absorbing boundary $\psi(t) = \oint \mathrm{d}\mathbf{s}[-D\nabla p(\mathbf{r}, t)]_{r=R}$, which, when making use of the Wronskian $[J_0'(x)Y_0(x) - J_0(x)Y_0'(x)] = 2/(\pi x)$ [74], yields

$$\psi\left(t\right) = \frac{2}{\pi\tau_R} \int_0^\infty \mathrm{d}\chi\, \chi\, \frac{W_0\left[\chi\left(1 + \Delta_R/R\right), \chi\right]}{J_0^2\left(\chi\right) + Y_0^2\left(\chi\right)}\, \exp\left(-\frac{\chi^2 t}{\tau_R}\right) \qquad (3.13)$$

Similar to the RTD, two distinct time regimes can be identified within the ITD. The asymptotic behavior for $t \to 0$ is

$$\psi(t) \sim \left(\tau_\Delta\sqrt{4\pi\left(1 + \Delta_R/R\right)}\right)^{-1} \exp\left(-\frac{\tau_\Delta}{4t}\right)\left(\frac{\tau_\Delta}{t}\right)^{3/2}, \qquad (3.14)$$

which gives a good approximation for times $t \ll \tau_R$. Note that the maximum of this distribution at $\tau_{\max} \equiv \Delta_R^2/(6D)$ again sets a lower limit, below which the continuum treatment is no longer a valid description. According to Eq. (3.14), $\psi(t)$ approaches a power law $\propto t^{-3/2}$ after its maximum at $\tau_{\max}$. This power law has an analogous origin as the power law in the RTD. Here, τ_R can be associated the typical time, when the diffusing object center realizes the finite extent of the detection area or, in other words, where the object realizes its size. For times smaller than τ_R, the object size R itself has only a minor influence on the prefactor of Eq. (3.14). For large times ($t \gg \tau_R$), Eq. (3.13) can be approximated by

$$\psi\left(t\right) \simeq \frac{2\ln\left(1 + \Delta_R/R\right)}{t\ln^2\left(t/\tau_R\right)}. \qquad (3.15)$$

The asymptotic behavior $\sim (t\ln^2 t)^{-1}$ follows from the fact that for large t, the detection area becomes very small with respect to the area explored by the object. Accordingly, $\psi(t)$ scales as the probability of the first return time of the origin of a two-dimensional random walk [72]. Details on the derivations of these approximations in the time regimes can be found in appendix A.6.5.

The behavior predicted by Eq. (3.15) for large interpeak times is, however, of limited use, because another object can enter the detection area before the object, which left the detection area last, returns. The memory to a object that leaves the detection area is lost on time scales of the order of $\tau_c \equiv 1/(cD)$. On these time scales, different objects can be regarded as entering and leaving the detection area with a constant rate. The rate of these exchange processes should scale with the inverse mean time $\tau_c^{-1} = cD$ for an object outside the detection area to enter it. Hence, in the limit of large t, an exponential distribution is expected,

$$\psi\left(t\right) \sim cD\exp\left(-\kappa\pi cDt\right), \qquad (3.16)$$

where κ is a constant of the order of unity.

The general behavior of the ITD and its approximations in the respective time regimes in the single particle domain, i.e., $t \ll \tau_c$, is shown in Fig. 3.6.
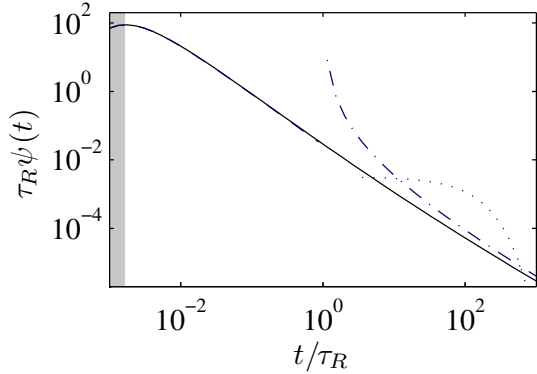
Figure 3.6: General behavior of the ITD [Eq. (3.13)] for a circular object with $R = 10, \Delta_R = 1$ and $D = 0.25$ (solid line). For times $\tau_{\max} \ll t \ll \tau_R$ it follows Eq. (3.14) with its transition into a power law $\propto t^{-3/2}$ (dashed line). The dotted line, indicating Eq. (3.16) for a coverage of $\theta = c\pi R^2 = 1\%$, illustrates that the logarithmic long time behavior according to Eq. (3.15) (dash-dotted line) can usually not be used for evaluation. The shaded area marks times $t < \tau_{\max}$, where the continuum treatment ceases to apply.

Application to simulation data

The time intervals between the signal turning off and on again, i.e., the interpeak times, are given out directly by the simulation described in chapter 2 and also should be sampled by one of the methods described in chapter 3.2. The ITDs of diffusing objects with two different radii $R = 5$ (Conf. C01) and $R = 10$ (Conf. C02) are displayed by the symbols in Fig. 3.7.

In case of the ITD there are two possibilities to obtain values for the diffusion coefficient. One is the consideration of the time regime $\tau_{\max} \ll t \ll \tau_R$, which will be presented first. As already mentioned, refinements would be necessary to describe the behavior of the ITD left to the maximum

$$\psi_{\max} = \frac{3\sqrt{6}D}{\sqrt{\pi(1 + \Delta_R/R)}e^{3/2}\Delta_R^2} \approx \frac{D}{a^2} \, . \tag{3.17}$$

However, they are not expected to yield larger values of the ITD. In fact, when considering jump dynamics of the molecules with a rate D/a^2 the ITD should behave as $\sim (D/a^2) \exp(-const. \times Dt/a^2)$ for short times, i.e., the largest value of the ITD should be of the order of D/a^2. Due to matching with the continuum treatment, $\psi_{\max}$ can be identified with the maximum seen in Fig. 3.7. This is a convenient way to determine D/Δ_R^2, and knowing this value to extract D by fitting the part right to the maximum predicted by Eq. (3.14). Again the limits of the time regime boundaries need to be checked self consistently. The resulting values in both cases are $D = 0.23 \pm 0.01$, which is in good agreement with the input value $D_{\text{in}} = 0.25$, and $\Delta_R = 0.8$, which is again of the order of the lattice constant $a = 1$. Using these values in Eq. (3.13) yields the solid lines in the main plots of Fig. 3.7.

The other possibility for obtaining values for D is to use the distribution in the particle exchange time regime $t \gg \tau_c$. However, adjustments on the interpeak time sampling might be necessary for this approach. The problem is that the interpeak times as well as their probabilities are spread over several orders of magnitude, so that even the sampling method described in reference et $al.$ [73] reaches its limits, see the main plots in Fig. 3.7. To resolve the exponential tail expected for times $t \gg \tau_c$, either the number of elements per bin has to be chosen rather small, or only interpeak times that lie in this time regime have to be considered for the sampling. The first approach results in a strong noise for

smaller times, the second has a uncertainty in setting the lower limit of this regime, when, in the beginning, no information is known about the system's parameters. Because the short interpeak times are irrelevant for this fitting anyway, the first approach should be the method of choice.

If a suitable distribution is available, the exponential decay can be fitted straight-forwardly with Eq. (3.16). Evaluating the long time regime for the presented configurations yields $D = 0.25 \pm 0.02$ (Conf. C01) and $D = 0.22 \pm 0.02$ (Conf. C02), when assuming $\kappa = 1$. This good agreement with the input value $D_{\text{in}} = 0.25$ reassures the choice of $\kappa = 1$. The number concentration c of objects is an input parameter in case of the simulation, but it is also easy to obtain from measurement data as the ratio of cumulative time, when the tip is occupied, to the overall measurement time. This will be used in chapter 7 for the analysis of experimental data. Information for Δ_R cannot be obtained here, because memory of the objects geometry is lost on this time scale.
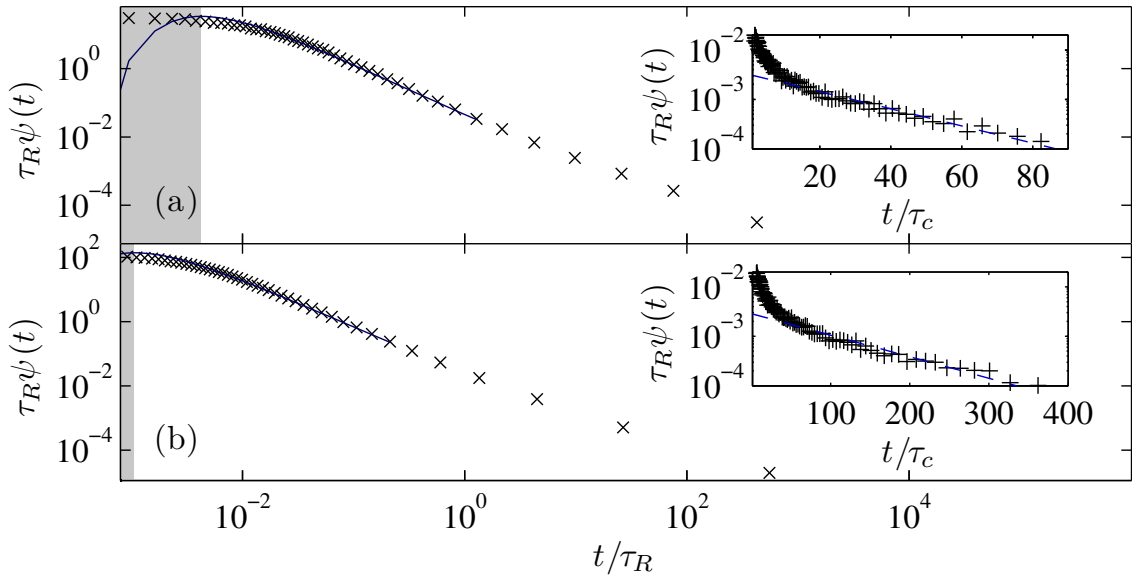
Figure 3.7: ITDs (symbols) of two representative object radii (a) $R = 5$ (Conf. C01) and (b) $R = 10$ (Conf. C02). The main plots show fitting of $t \ll \tau_R$ with Eq. (3.14), which yields $D = 0.23 \pm 0.01$ and $\Delta_R = 0.8$ in (a) as well as $D = 0.23 \pm 0.01$ and $\Delta_R = 0.8$ in (b). Solid lines mark the full distributions according to Eq. (3.13), when using the fitted parameters. Dashed lines in the insets show evaluation of $t \gg \tau_c$ with Eq. (3.16), which yields $D = 0.25 \pm 0.02$ in (a) and $D = 0.22 \pm 0.02$ in (b). The shaded areas mark the respective short time regime $t < \tau_{\text{max}}$ excluded from fitting.

3.4   Prerequisites for experiments

In this chapter it was shown that the diffusion coefficient can be reliably extracted from a simulated fluctuating signal with all three methods. The obtained diffusion coefficients in most cases agree with the input value of the simulation within error margins or are very close, as summarized in Tab. 3.1. This is not surprising for the evaluation of simulation data, where external error sources are not present. This ideal situation can now be used to check certain prerequisites for a real experiment [‡].

R	D_{in}	ACF	RTD	ITD (front)	ITD (tail)
5	0.25	0.27 ± 0.02	0.22 ± 0.06	0.25 ± 0.02	0.23 ± 0.01
10	0.25	0.22 ± 0.02	0.23 ± 0.03	0.22 ± 0.02	0.23 ± 0.01

Table 3.1: D values of circular molecules determined from substitute simulation data.

For instance, all presented theories base on objects with a finite lateral extent. But it has to be investigated, whether the theoretical description will fail in the transition to point-like objects. And if so, how small the objects can become, before the description fails. For the ACF the limit $R \to 0$ can be readily given, resulting in the classical t^{-1} behavior for point-like particles [75]. Also the exponential decay for $t \gg \tau_c$ in the ITD is independent of the actual object size. But its short interpeak time regime and especially the RTD strongly depend on the object geometry, because here the object size R and the length Δ_R, which is typically associated with the object's jump length, are entering the theory. A step size large compared to the object's size ($R \leq \Delta_R$) is physically meaningless in the description of the RTD, but also $R \gtrsim \Delta_R$ causes problems. Both would result in a small amount of valid positions inside the detection area and therefore rather a "jump in" and "jump out" scenario than a diffusive motion. In the ITD for times $t \ll \tau_R$ the same reasoning applies.

Figure 3.8 (a) and (b) show the RTDs and ITDs for small object radii $R = 1$ (Conf. C03) and 4 (Conf. C06). The data is described very well for all radii with Eq. (3.9) and (3.13) using the respective fitting values, see the solid lines in Fig. 3.8 (a) and (b), though the input diffusion coefficient D_{in} is not reproduced, see Fig. 3.8 (c). The diffusion coefficients obtained by fitting are summarized in Fig. 3.8 (c), together with those from the evaluation of further object radii (Conf. C01-C06). To avoid finding misleading diffusion coefficients $\tilde{R}/a = R = 3$ is set as a lower limit for the object size in terms of applicability of these evaluation methods to simulated as well as experimental measurements.
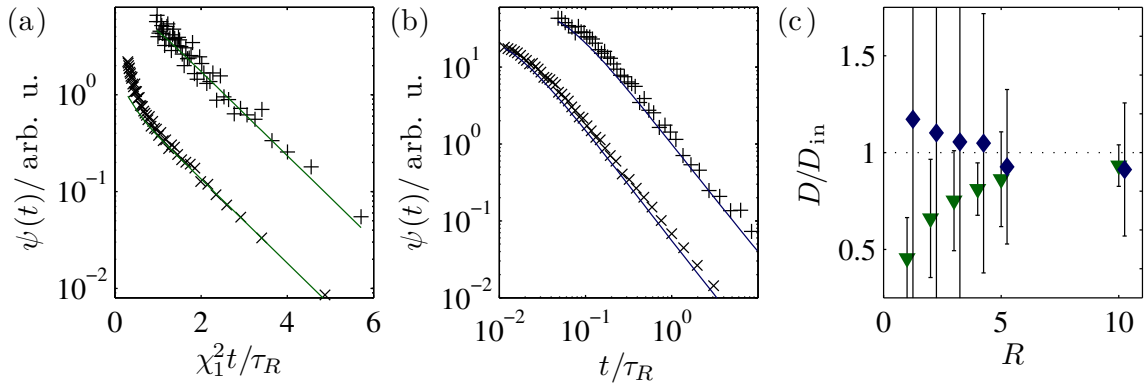
Figure 3.8: (a) RTDs for object radii $R = 2$ ($+$) and $R = 4$ ($\times$). Diffusion coefficients resulting from fitting are $D = 0.16 \pm 0.08$ and $D = 0.20 \pm 0.08$ respectively. (b) ITDs for the same object radii. Fitting of the short time regime yields $D = 0.28 \pm 0.3$ and $D = 0.26 \pm 0.16$. Solid lines show the theoretical curves according to Eq. (3.9) and Eq. (3.13) with the respective fitting values. Graphs in (a) and (b) were vertically shifted for better visibility. (c) Summary of diffusion coefficients resulting from the RTD and short time regime of the ITD for these and further object radii (Conf. C01-C06). Non-misleading diffusion coefficients can be obtained for $R \geq 3$.

Naturally, the quality of the evaluations increases with the number of recorded events. While the simulation can run until enough events have been recorded, it may be problematic in an experiment. Therefore, by means of the simulation a minimum number M of recorded events for a sufficient determination of the diffusion coefficient shall be given. With the ACF already a total number of 10^2 events is enough to reproduce the input diffusion coefficient within error margins, see squares in Fig. 3.9 (d). Larger number of events improve the ACF only outside of the time regime relevant for fitting.

For evaluation of the RTD the exponential decay for $t \gg \tau_R/\chi_1^2$ is relevant. The diamonds in Fig. 3.9 (d) show, that a total of 10^3 events is necessary to determine the given diffusion coefficient within error margins. The ITD for 10^2 is too noisy for evaluation, therefore at least 10^3 events should be recorded. Concerning the evaluation in the particle exchange time regime $t \gg \tau_c$, recording of 10^3 events is recommended analogously to the RTD. As follows from $\int_{\tau_{\max}}^{\tau_c} dt \, \psi(t)$ [with $\psi(t)$ from Eq. (3.13)], depeding on R and c, maximal 15% of the interpeak intervals are larger than τ_c, compare Fig. B.3 in the appendix. This leaves only a fraction of the recorded events relevant for fitting. This argumentation can be analogously used to explain the relatively large number of events necessary for an RTD evaluation, where maximal 25% of the events are relevant for fitting ($t \geq \tau_R/\chi_1^2$).

Keeping in mind the further uncertainties in an experiment, the recommendation is to perform measurements that record at least $M = 10^3$ events for an ACF evaluation and $M = 10^4$ events for an analysis of the distributions.
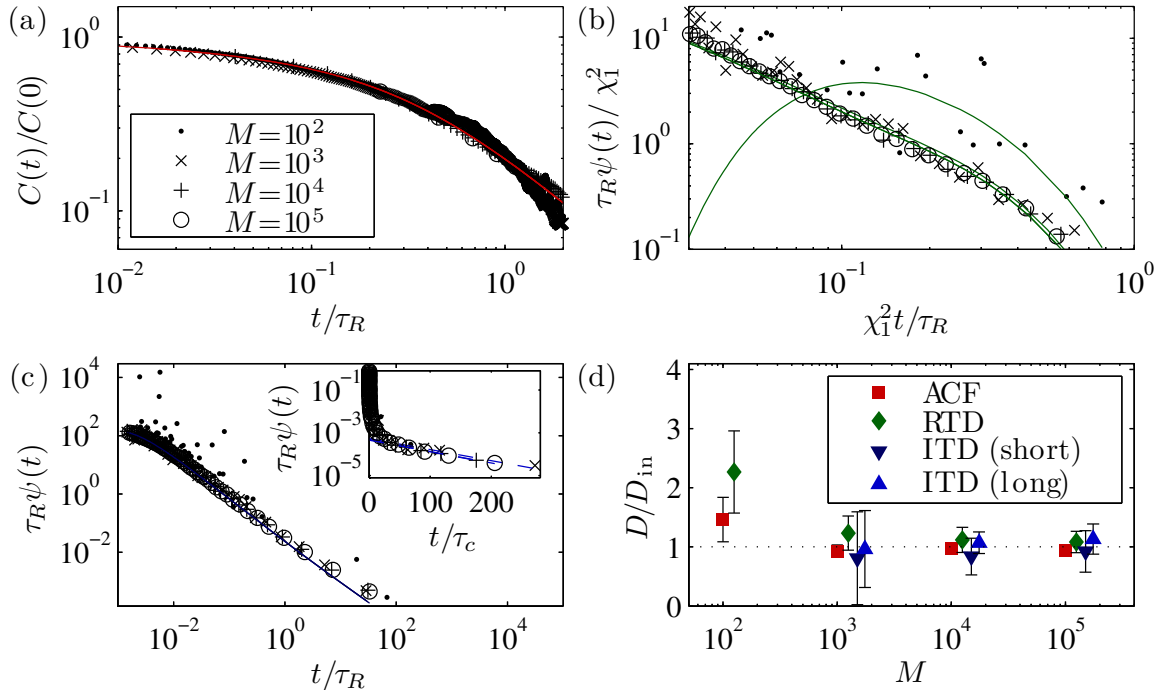
Figure 3.9: (a) ACFs, (b) RTDs, (c) ITDs for $R = 10$ (Conf. C02) with different numbers of events between $M = 10^2$ and $M = 10^5$ used for the analysis. (d) Diffusion coefficients obtained from respective fittings. Evaluation of the ITD was not reasonable for $M = 10^2$ events. Data points have been horizontally shifted for better visibility here. For all methods $M = 10^3$ events are enough for a sufficient accuracy.

Chapter 4

Rectangular shaped objects

So far the focus of this work lay on objects with a circular shape. However, rectangles are a more appropriate geometric representation for several of the molecules used in surface science, see Fig. 1.1 (d)-(f). Therefore, the treatment in chapter 3 has to be modified for objects with rectangular shape of size $L_\mathrm{s} \times L_\mathrm{l}$, where, without loss of generality, the shorter edge is addressed by L_s and the longer one by L_l, as shown in Fig. 4.1 (a). Significant changes in the functional behavior of the distributions and autocorrelation function are expected for aspect ratios $\alpha \equiv L_\mathrm{l}/L_\mathrm{s} \gg 1$. In this chapter the necessary adjustments are made to the treatment in chapter 3 to cover the different object shape. This includes the choice of a Cartesian instead of a polar coordinate system. The measurement setup itself is not affected.

The evaluation methods are again validated against simulation data in the first place. Implications of the object shape will also be addressed upon applying the evaluation methods to real measurement data in chapter 7.
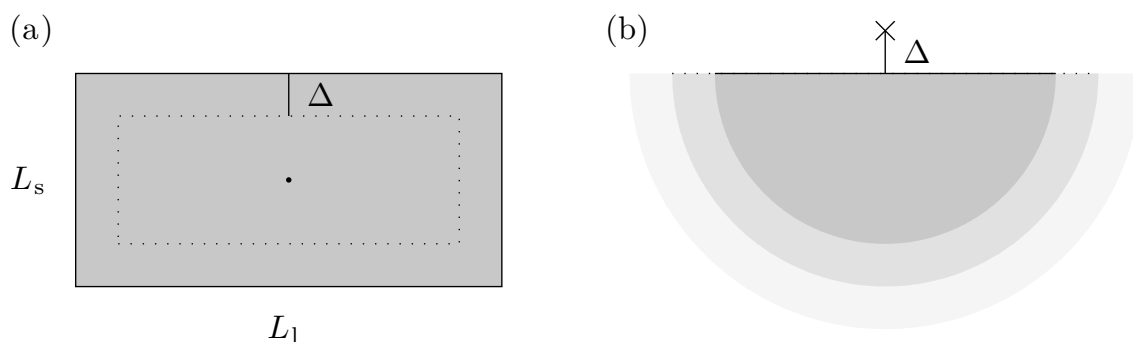
Figure 4.1: (a) Sketch of a rectangular object's geometry used for ACF and RTD with its defining lengths: The edges L_s and L_l, as well as the minimal penetration depth Δ. The dot marks the probing site and the shaded area is the detection area, defined by those object center positions that turn the signal "on". (b) Sketch of the substitute situation for the ITD at short times. A point-like object diffuses in front of a infinite extended absorbing wall after starting in distance Δ from it.

4.1 Autocorrelation function

Adjustments on the autocorrelation function are marginal, since the object's shape does not enter the general derivation in the previous chapter [Eq. (3.3)]. For a quantitative evaluation of simulated data only the detection area has to be adapted to a rectangular objects geometry. If a rectangle is assigned to the set $\mathcal{D}$ of object center positions, that give rise to a signal, Eq. (3.4) is a combination of Heaviside jump functions $s[\mathbf{r}(t)] = [\Theta(x + L_l/2) - \Theta(x - L_l/2)][\Theta(y + L_s/2) - \Theta(y - L_s/2)]$ with the object edge lengths L_l and L_s. Eq. (3.3) then yields

$$C(t) = \frac{c}{\pi} \left[-\sqrt{4Dt} \left(1 - e^{-\frac{\tau_{L_l}}{4t}} \right) + L_l \sqrt{\pi} \operatorname{erf} \left(\sqrt{\frac{\tau_{L_l}}{4t}} \right) \right]$$
$$\left[-\sqrt{4Dt} \left(1 - e^{-\frac{\tau_{L_s}}{4t}} \right) + L_s \sqrt{\pi} \operatorname{erf} \left(\sqrt{\frac{\tau_{L_s}}{4t}} \right) \right], \tag{4.1}$$

with the two typical times $\tau_{L_l} \equiv L_l^2/D$ and $\tau_{L_s} \equiv L_s^2/D$, representing the mean time an object needs to cross the detection area in the respective direction.

These two times separate three distinct time regimes in the ACF. It gives $C(0) = cL_lL_s$ for $t \to 0$, which is the expectation value of the signal. For intermediate times $\tau_{L_s} \ll t \ll \tau_{L_l}$ the ACF will follow a power law $\propto t^{-1/2}$ and in the long time limit again the power law $\propto t^{-1}$ known from the circular solution in chapter 3.1 is dominant. Derivations of these approximations are given in appendix A.6.2. The general behavior of the ACF for rectangular shaped objects with two different aspect ratios is displayed in Fig. 4.2. It shows, that the intermediate time regime will only be visible for very high aspect ratios, i.e. rodlike objects.
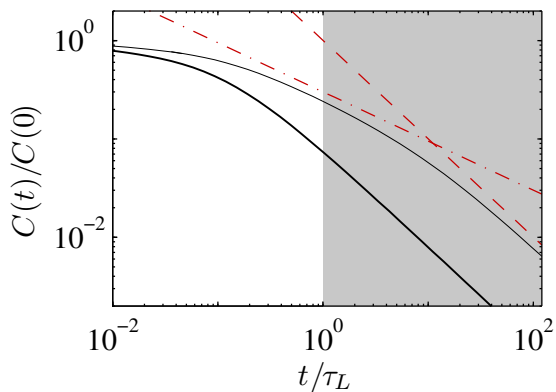
Figure 4.2: General behavior of the ACF [Eq. (4.1)] for rectangular objects with sizes (a) 10×10 (bold line) and (b) 10×100 (thin line), both with $D = 0.25$. For $t \to 0$ the expectation value $C(0)$ is approached and for large times $t \gg \tau_{L_l}$ the ACF shows a power law $\propto t^{-1}$ (indicated by the dashed line). The intermediate time regime, which would follow a power law $\propto t^{-1/2}$ (indicated by the dash-dotted line), can only be guessed, even for an aspect ratio of $\alpha = 10$. The time regime $t \geq \tau_{L_s}/4$ (shaded area) is excluded from evaluation.

Application to simulation data

A non-linear least square fit was used to exemplarily fit Eq. (4.1) to the autocorrelation function of simulated fluctuating signals, generated by rectangular diffusing molecules of different aspect ratio, see Fig. 4.2. The raw simulation data was again prepared as described in appendix B.1. To ensure the exclusion of cross correlation events, which

are not accounted for in the theory, only times $t \ll \tau_{L_s}$ ($t \leq \tau_{L_s}/4$) are considered for for evaluation. This condition is checked repeatedly during the fitting process. The obtained diffusion coefficients are $D = 0.25 \pm 0.03$ for a 10×10 [Conf. R01, Fig. 4.3 (a)] and $D = 0.26 \pm 0.03$ for a 10×20 [Conf. R02, Fig. 4.3 (b)] object and agree very well with $D_{in} = 0.25$ used in the simulation.
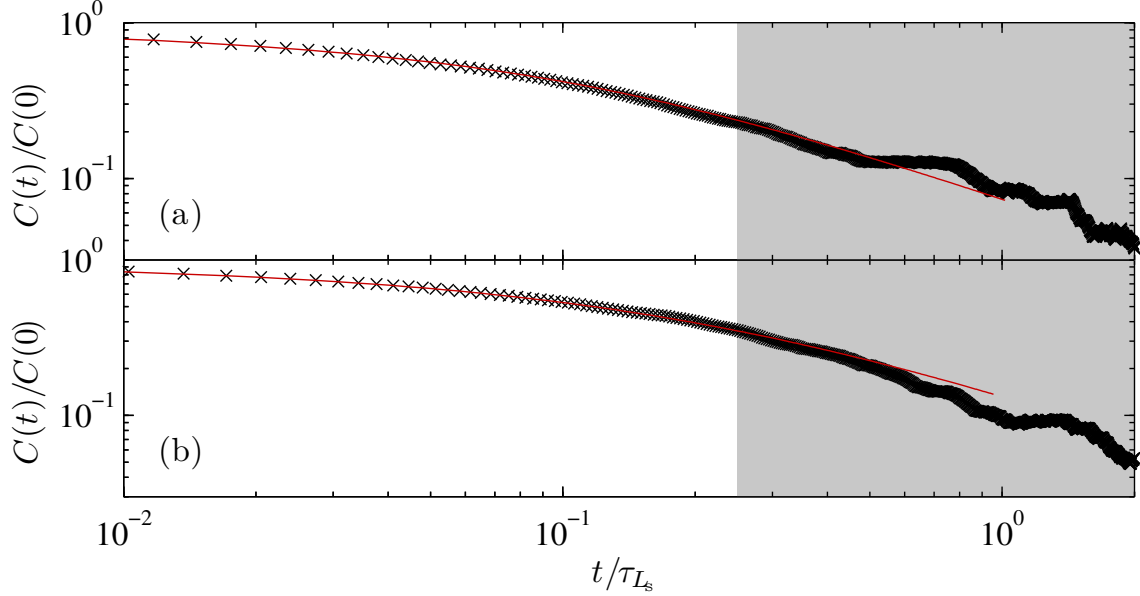
Figure 4.3: Representative ACFs of (a) 10×10 (Conf. R01) and (b) 10×20 (Conf. R02) sized objects. Evaluation of the short time regime yields $D = 0.25 \pm 0.03$ in(a) and $D = 0.24 \pm 0.03$ in (b) matching the input value of $D_{in} = 0.25$. Times $t > \tau_{L_s}/4$, marked by the shaded area, are excluded from fitting. Solid lines result from Eq. (4.1) using the respective fitting values.

4.2 Residence time distribution

The principle for the derivation of the residence time distribution (RTD) in case of rectangular shaped object is analogous to chapter 3.2 [‡]. The diffusion propagator $p(\mathbf{r}, t)$ of an object center diffusing inside a closed absorbing boundary, which is now formed by the edges of a rectangle, has to be determined. A uniform distribution of the object center on an inner rectangle contour, displaced by Δ from the absorbing boundary, is used as initial condition.

Expansion of $p(\mathbf{r}, t)$ in terms of the eigenfunctions $f_{\mu,\nu} = \sin(\mu\pi x/L_l)\sin(\nu\pi x/L_s)$, with $\mu = 2m + 1$, $\nu = 2n + 1$ and $m, n = 0, 1, \dots$ of the Laplacian yields

$$p(\mathbf{r}, t) = \sum_{m,n=0}^{\infty} c_{\mu,\nu} f_{\mu,\nu} \exp\left(-D\lambda_{\mu,\nu}^2 t\right) \tag{4.2}$$

with $\lambda_{\mu,\nu}^2 = \pi^2[(\mu/L_l)^2 + (\nu/L_s)^2]$ and coefficients

$$c_{\mu,\nu} = \frac{8\left[\frac{L_s}{\nu}\sin\left(\frac{\mu\pi}{L_l}\Delta\right)\cos\left(\frac{\nu\pi}{L_s}\Delta\right) + \frac{L_l}{\mu}\sin\left(\frac{\nu\pi}{L_s}\Delta\right)\cos\left(\frac{\mu\pi}{L_l}\Delta\right)\right]}{\pi L_l L_s (L_l + L_s - 4\Delta)} \tag{4.3}$$

from the boundary conditions.

The RTD follows from the established procedure $\psi(t) = -\partial_t \int_0^{L_l} \mathrm{d}x \int_0^{L_s} \mathrm{d}y \, p(\mathbf{r}, t)$, yielding

$$\psi(t) = \frac{4DL_lL_s}{\pi^2} \sum_{m,n=0}^{\infty} \frac{c_{\mu,\nu}\lambda_{\mu,\nu}^2 \exp\left(-D\lambda_{\mu,\nu}^2 t\right)}{\mu\nu} . \tag{4.4}$$

Not surprisingly, this RTD shows the same functional time dependence as the RTD for circular shaped objects discussed in chapter 3.2. Again a lower time limit for applicability of the method is given by $\tau_\Delta \equiv \Delta^2/D$, see discussion in chapter 3.2. A power law decay occurs at intermediate times $\tau_\Delta \ll t \ll \tau_{\lambda_{1,1}} \equiv 1/\lambda_{1,1}^2 D$ and an exponential decay

$$\psi(t) \sim \frac{4DL_lL_s}{\pi^2} c_{1,1}\lambda_{1,1}^2 \exp\left(-D\lambda_{1,1}^2 t\right) \tag{4.5}$$

for $t \gg \tau_{\lambda_{1,1}}$, that can be readily used for the fitting. Details of the derivation of the approximations in the single time regimes can be found in appendix A.6.4.

The general behavior of this RTD [Eq. (4.4)] and its approximations in the corresponding time regimes is given in Fig. 4.4.
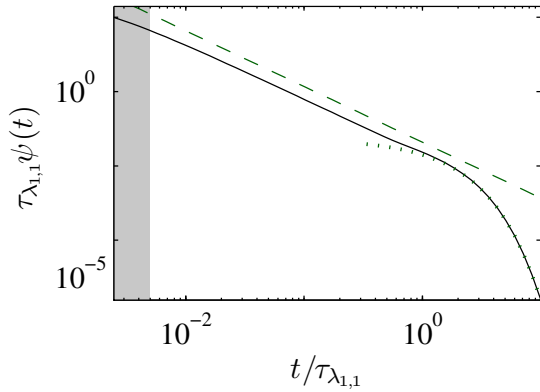
Figure 4.4: General behavior of the RTD [Eq. (4.4)] for rectangular objects of size 50×100 with $\Delta = 1$ and $D = 0.25$ (solid line). Note that proportions of L_l, L_s and Δ are again chosen deliberately extreme in this example, to enhance the power law $\propto t^{-3/2}$ in the intermediate time regime $\tau_\Delta \ll t \ll \tau_{\lambda_{1,1}}$ (indicated by dashed line). For times $t \gg \tau_{\lambda_{1,1}}$ the exponential decay used for fitting is clearly visible (emphasized by dotted line). The shaded area marks times $t < \tau_\Delta$.

Application to simulation data

This theory for the RTD of rectangular shaped objects was validated against two exemplary simulations of diffusing rectangular objects with different aspect ratio (Conf. R01 and Conf. R02). The exponential decay at times $t \gg \tau_{\lambda_{1,1}}$ together with Eq. (4.5) was employed for the evaluation. The lower time limit was subsequently revised during the fitting. The resulting diffusion coefficients are $D = 0.24 \pm 0.04$ for a 10×10 and $D = 0.27 \pm 0.05$ for a 10×20 rectangle. Both agree very well with the input value $D_{\mathrm{in}} = 0.25$ used in the simulation. Again these values can be used in a further step to determine $\Delta \approx 2.5$ for both sets, which are slightly larger than comparable values in the circular approach, but still of the order of the step length. Fig. 4.5 shows, that putting the respective fitted parameters into Eq. (4.4) gives a good account on the overall RTD.

Figure 4.5: Symbols illustrate the RTDs generated by two representative rectangular object sizes (a) 10×10 (Conf. `R01`) and (b) 10×20 (Conf. `R02`). Evaluation of the time regime $t \gg \tau_{\lambda_{1,1}}$ with Eq. (4.5) yields $D = 0.24 \pm 0.04$ in (a) and $D = 0.27 \pm 0.05$ in (b), which match the input value of $D_{\mathrm{in}} = 0.25$. The minimal penetration depth is $\Delta \approx 2.5$ for both. The solid lines mark the full distributions according to Eq. (4.4) when using the fitted parameters.

4.3   Interpeak time distribution

To give the interpeak time distribution (ITD) of a rectangular object, the problem of the object center diffusing outside a rectangular absorbing boundary would have to be solved. The initial probability should be spread on a outer rectangle displaced by Δ with respect to the absorbing boundary. It was not possible for the author to derive a closed form expression for the diffusion propagator in this situation or to find a derivation of this problem in the literature. Therefore, only a qualitative description of the ITD is available.

For small times $t \ll L_{\mathrm{s}}^2 / D$ the object has not realized its own size and the situation can be compared to that of a point-like particle diffusing in front of a infinite extended absorbing wall, after starting in a distance Δ from the boundary, see Fig. 4.1 (b). The free propagator of this setup is $p(x, y, t | x_0, y_0) = \exp\{-[(x_0 - x)^2 + (y_0 - y)^2]/(4Dt)\}/(4\pi Dt)$, compare Eq. (A.6) in the appendix. The absorbing boundary can be incorporated by subtracting the propagator of the point mirrored at the boundary [76]. Arbitrarily setting the x-axis as absorbing boundary, the propagator reads $\tilde{p}(x, y, t | x_0, y_0) = p(x, y, t | x_0, y_0) - p(x, -y, t | x_0, y_0)$. This gives the time distribution

$$\psi(t) = \left(\tau_\Delta \sqrt{4\pi}\right)^{-1} \exp\left(-\frac{\tau_\Delta}{4t}\right) \left(\frac{\tau_\Delta}{t}\right)^{3/2} \tag{4.6}$$

according to $\psi(t) = \int_0^\infty \mathrm{d}y \int_{-\infty}^\infty \mathrm{d}x\, \tilde{p}(x, y, t | 0, \Delta)$. The maximum at $t_{\max} \equiv \Delta^2 / 6D$ again gives a lower limit for the applicability of this theory, for the previously discussed reasons, cf. chapter 3. Eq. (4.6) shows the same functional behavior as Eq. (3.14). The prefactor is slightly different, but in the limit of $\Delta_R \ll R$, Eq. (3.14) becomes Eq. (4.6). It follows, that the functional behavior of the return time for a single object on suitable time scales is

independent on the objects actual shape, if $\Delta \ll R$. Another possibility to approximately deal with this time regime, will be discussed in chapter 4.4.

As previously discussed in chapter 3.3, the long time regime $t \gg \tau_c$, which is dominated by exchange processes of different objects, is independent of their shape, because the detection area is considered as point-like here. This time regime will follow Eq. (3.16).

Application to simulation data

The ITDs of objects with two differet aspect ratios with $D_{\mathrm{in}} = 0.25$ (Conf. R01 and Conf. R02) are shown in Fig. 4.6. The interpeak intervals were sampled as described in Chap. 3.2. In principle, the single-particle short time regime as well as the particle exchange long time regime can be used separately for determining the diffusion coefficient from the ITD. However, so far only the evaluation of the long time regime $t \gg \tau_c$ is reliable. Exemplarily, a linear regression of the exponential decay (dashed line in the inset of Fig. 4.6) yields $D = 0.25 \pm 0.02$ for a 10×10 and $D = 0.24 \pm 0.05$ for a 10×20 rectangle, when assuming $\kappa = 1$.

Nevertheless an evaluation with Eq. (4.6) in the short time regime is executed, to investigate the quality of the rough treatment. In order to do so, a Levenberg-Marquardt fit with three free parameters is employed. The first two are the diffusion coefficient D and penetration depth Δ. The third is a prefactor replacing $(\tau_\Delta \sqrt{4\pi D})^{-1}$ in Eq. (4.6) to compensate the error of neglecting the object size. The results are $D = 0.26 \pm 0.07$ (Conf. R01) and $D = 0.24 \pm 0.07$ (Conf. R02) as well as $\Delta \approx 1.0$, which indeed agrees very well with the input parameters, although the uncertainty increases slightly. The findings are visualized by the solid line in the main plot of Fig. 4.6.
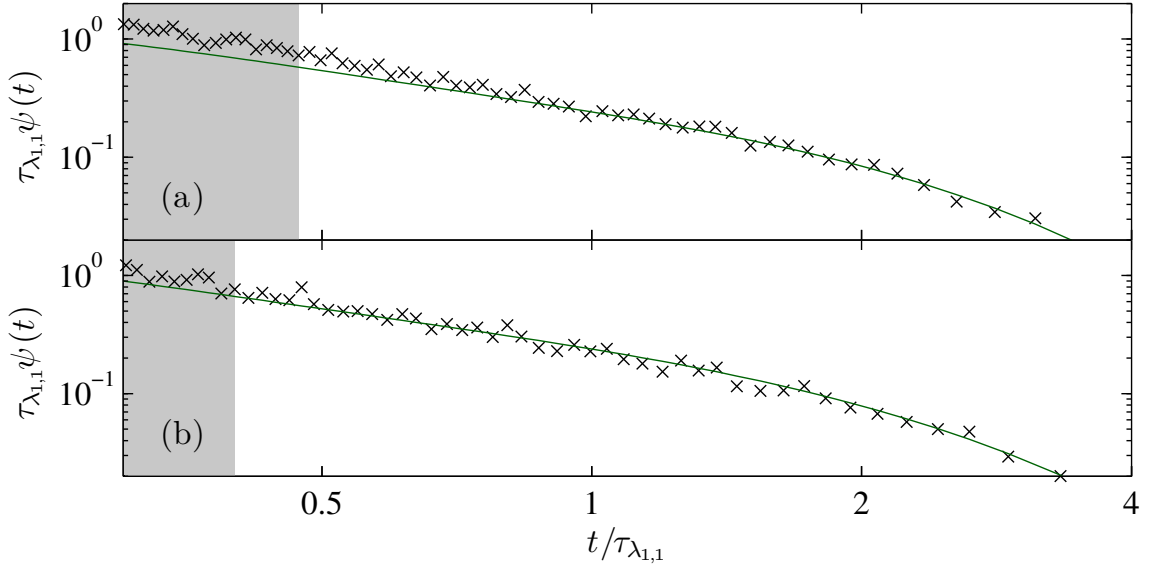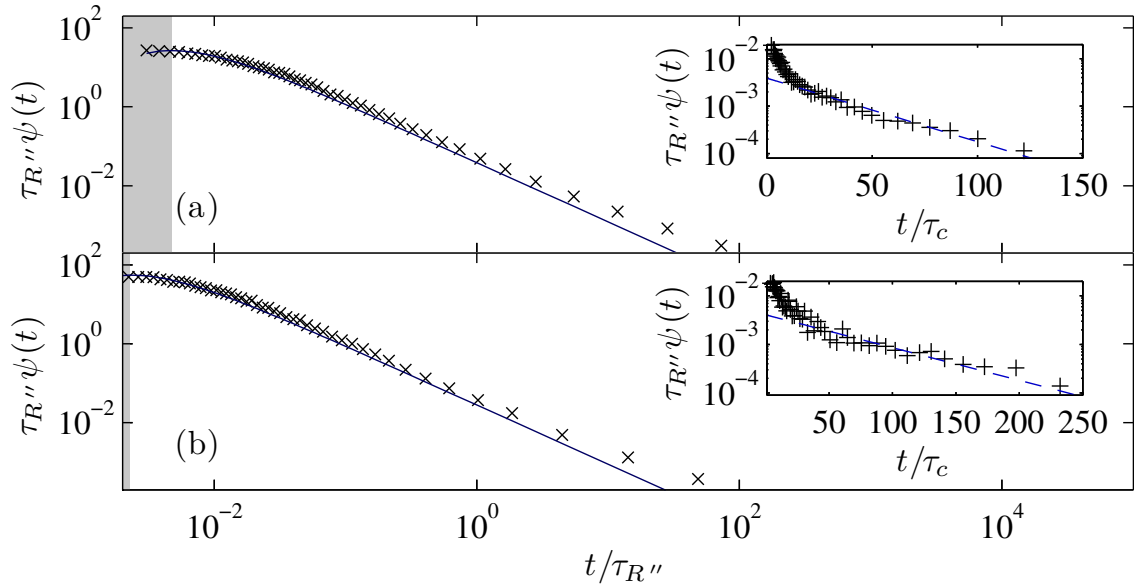

Figure 4.6: Symbols illustrate the ITDs generated by two representative rectangular object sizes (a) 10×10 (Conf. R01) and (b) 10×20 (Conf. R02). Semilogarithmic plots of the respective exponential tails can be found in the inset. Evaluation of the time regime $t \gg \tau_c$ with Eq. (3.16) yields $D = 0.25 \pm 0.02$ in (a) and $D = 0.24 \pm 0.06$ in (b) (dashed lines in the insets). The solid lines in the main plots indicate the approximate treatment according to Eq. (4.6), which yields $D = 0.26 \pm 0.07$ in (a) and $D = 0.24 \pm 0.07$ in (b) as well as $\Delta \approx 1.0$ for both.

4.4   Similarities to circular approach

After implementing the necessary modifications, also for rectangular molecules the input diffusion coefficients used in the simulation were reliably reproduced independent of the applied method, as displayed in Tab. 4.1.

$L_s \times L_l$	D_{in}	ACF	RTD	ITD (front)	ITD (tail)
10×10	0.25	0.25 ± 0.03	0.24 ± 0.04	$0.26 \pm 0.07^*$	0.25 ± 0.02
10×20	0.25	0.26 ± 0.03	0.27 ± 0.05	$0.24 \pm 0.07^*$	0.24 ± 0.05

Table 4.1: Overview of D values for rectangular molecules determined from substitute simulation data ($*$: approximate treatment).

Upon incorporating rectangular objects into the three evaluation methods, it turns out that the functional behavior, known from circular objects, is mostly preserved. This is not very surprising and leads to the question, if the differentiation according to the object shape is really necessary.

Assuming that the rectangular solutions were unknown, one could try to assign a circle to the rectangular object, for example by preserving its edge length $R_{edge} = (L_s + L_l)/\pi$ or area $R_{area} = (L_s L_l/\pi)^{1/2}$ or by using its area gyration radius $R_{gyr} = 12^{-1/2}(L_s + L_l)$. Using these radii in Eq. (3.7) to fit the ACF of rectangular shaped objects, however fails to reproduce the input diffusion coefficient used for simulation [Fig. 4.7 (b)], though the fit itself agrees very well with the correlation, see Fig. 4.7 (a). This leads to the conclusion, that even for aspect ratios close to 1 the ACF strongly depends on the objects shape. When choosing the rectangular ACF [Eq. (4.1)] for evaluation, the obtained diffusion coefficients match the input values very well, as can be seen by the rectangles in Fig. 4.7 (b).

Figure 4.7: (a) ACFs of the signal from diffusing rectangular objects with different aspect ratios $\alpha = 1$ (+, Conf. R01), 2 (×, Conf. R02), 3 (*, Conf. R03) and 4 (●, Conf. R04). They have been shifted vertically for better visibility. (b) Diffusion coefficients resulting from an evaluation with the circular ACF solution [Eq. (3.7)] with different definitions of R as well as with the rectangular ACF [Eq. (4.1)]. Respective fitting curves are congruent solid lines in (a).

In case of the RTD circular as well as rectangular objects show an exponential decay for large residence times, which is relevant for the fitting. For evaluating the RTD of

rectangular objects, one could therefore again try to use the circular RTD [Eq. (3.9)] with one of the above mentioned radii. Fig. 4.8 summarizes the fitting of the RTD of rectangular objects with different aspect ratios α with the rectangular as well as the circular approach. Both fits agree very well with the data, see Fig. 4.8 (a). But while for $\alpha \approx 1$ all obtained D match the one used in the simulation, a listing of diffusion coefficients obtained at higher α reveals that those obtained with the circular approach disagree with the input and the discrepancy increases with the aspect ratio, see Fig. 4.8 (b).

Evidently, arbitrarily chosen radii yield erroneous results. However, with the knowledge of the exact rectangular solution Eq. (4.4) an abstract radius

$$R' \equiv \frac{\chi_1}{\pi} \left(L_{\mathrm{l}}^{-2} + L_{\mathrm{s}}^{-2} \right)^{-1/2} \tag{4.7}$$

can be defined, by comparing the long time limits Eq. (3.11) and Eq. (4.5) of both approaches. Using this radius in the circular solution [Eq. (3.9)], the fit agrees very well with the simulation data [Fig. 4.8 (a)].
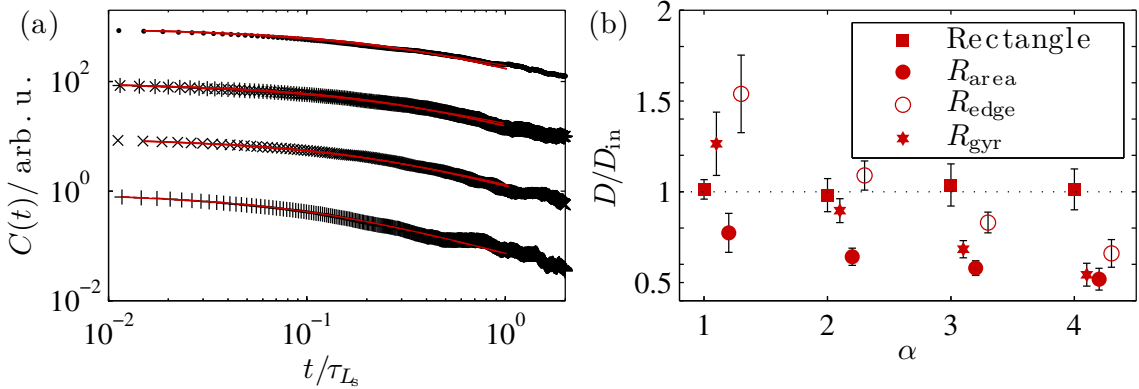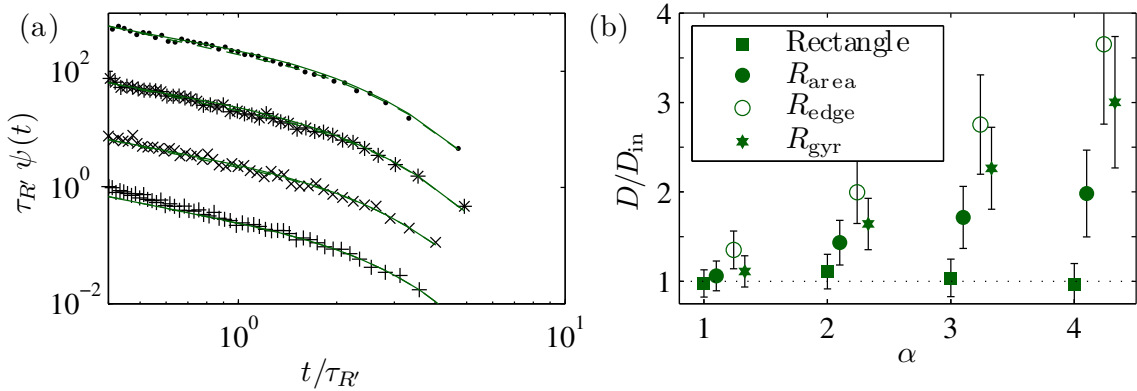

Figure 4.8: (a) RTDs of the signal from diffusing rectangular objects with different aspect ratios $\alpha = 1$ (+, Conf. R01), 2 (×, Conf. R02), 3 (∗, Conf. R03) and 4 (●, Conf. R04) as well as corresponding fits with Eq. (3.9) (dashed lines) and Eq. (4.4) (solid lines, nearly congruent). They have been shifted vertically for better visibility. (b) Diffusion coefficients resulting from an evaluation of the exponential decay with the circular RTD solution [Eq. (3.11)] and different definitions of R as well as with the rectangular RTD solution [Eq. (4.5)].

As mentioned in chapter 4.3, the attempt to derive a closed form for the ITD in the presence of a rectangular detection area was not successful. However, with the finding, that the RTD for rectangular shapes can be well approximated by the RTD for circular shapes by using an appropriate radius, one can follow a corresponding route here to find an approximate solution for the ITD. At long times, the ITD is governed by exchange processes of different objects, yielding an exponential decay with characteristic time $\propto 1/cD$. The number density $c = \theta_0/\tilde{A}$ indirectly contains the object geometry due to its relation to the coverage θ_0 of freely diffusing objects. So supposedly, the object area $\tilde{A}$ rather than the shape itself is relevant here and a circle with the same area can be assigned to the rectangle by defining

$$R'' = R_{\mathrm{area}} \equiv \left(L_{\mathrm{s}} L_{\mathrm{l}} / \pi \right)^{1/2}. \tag{4.8}$$

Inserting this R'' in the exact solution for circular objects [Eq. (3.13)] one could expect that it provides a good account of the ITD of rectangular shaped objects. Indeed, a good agreement with the simulation data for $t \leq \tau_{R''} \equiv R''^2/D$ can be asserted, see Fig. 4.9.
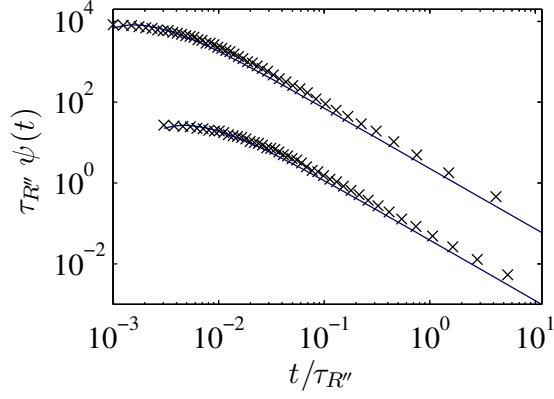
Figure 4.9: ITDs of obtained from diffusing object of aspect ratio $\alpha = 1$ (+, Conf. R01) and 5 (×, Conf. R05). The short time regime $t < \tau_{R''}$ of both curves can be described very well with Eq. (3.13), when using R'' [Eq. (4.8)] as substitute radius.

Concluding, for aspect ratios $\alpha \approx 1$ the actual object shape is secondary in the RTD and ITD methods, but for higher aspect ratios it has to be taken into account. Nevertheless, there are strong similarities between approaches using a rectangle or circular detection area. In the RTD and ITD, these can be utilized to define abstract radii [Eqs. (4.7) and (4.8)], which enable to approximately transform the solutions into another.

Chapter 5

Rotational diffusion

When an object can rotate around its center of mass, new possibilities arise to enter or leave the detection area, that are not accounted for in the previous treatments. Their influence will be negligible for individual reorientation moves. In case of a steady rotational movement, the implications on the signal can be exploited to quantify the rotational dynamics, as will be demonstrated in the following.

To approach the difficulty of incorporating an additional degree of freedom into the theory a simple model is considered here. Discrete rotational moves are supposed to occur independent of translational moves, i.e., there is no coupling between rotation and translation. In this model, rectangular shaped objects of size $L_\mathrm{s} \times L_\mathrm{l}$ perform transitions between n possible orientations separated by an angle $a_\varphi = 2\pi/n$, with $n = 10$ in the following. The transitions occur between neighboring orientations around the object center with a constant rate $\omega_\varphi = 2D_\varphi/a_\varphi^2$, where D_φ is the rotational diffusion coefficient. The measurement setup remains unchanged with a locally fixed point-like probing site, where an "on" signal is recorded, whenever the probing site is covered, and "off" otherwise.

(a) (b) (c)
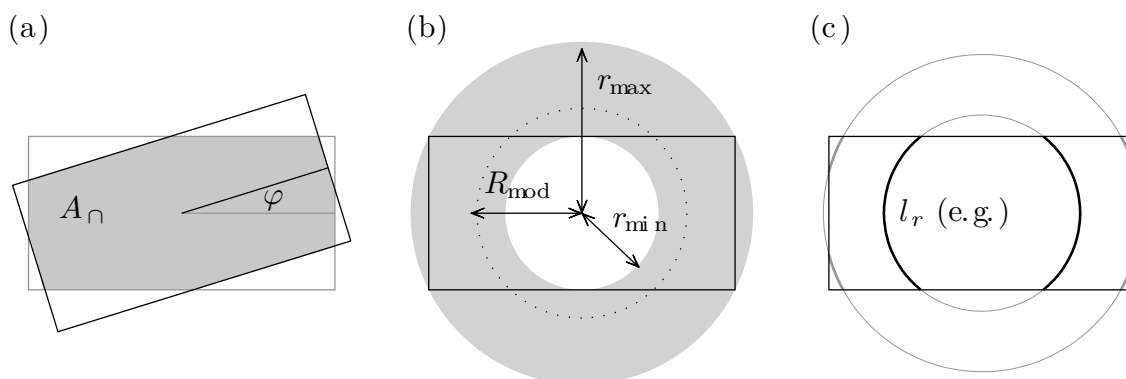
Figure 5.1: (a) Different orientations of starting (gray boundary) and target (black boundary) detection area. The displacement is characterized by φ. The shaded area marks the overlap $A_\cap(\varphi)$ relevant for the ACF. (b) Classification of distances between the object center (center of figure) and probe tip: The signal is influenced by rotation only in the shaded area. (c) Detection lines in case of pure rotational diffusion: If the center of a rectangular object sets the origin of a corotating coordinate frame, rotational diffusion leads the probe to diffuse along concentric circles. The intersection set of these circles with the rectangle yields arcs that define detection lines of length l_r (inner arcs for the RTD and outer arcs for the ITD).

5.1 Autocorrelation function

When incorporating rotational diffusion in the treatment of the autocorrelation function, one has to be aware that the starting and target detection area, i.e., the set of positions that give rise to a signal at $t = 0$ and those at t, are no longer inevitably identical. Since the object could have taken rotational steps in the meantime, the definition of the detection area has to additionally contain the angular orientation of the object here, see Fig. 5.1 (a). Knowing this, an expression for the ACF can be given as described in appendix A.2. As an alternative to the extensive treatment of this full solution, a much more convenient approximate approach for the short time regime $t \ll \tau_{L_\mathrm{s}}$ will be presented here.

The typical time to cross the detection area via translational motion is $\tau_{R'} = R'^2/D$ and the typical time it takes the object to change its orientation by φ is $\tau_\varphi = \varphi^2/D_\varphi$. Comparison of these times allows an estimation of $\varphi = (R'^2 D_\varphi/D)^{1/2}$ on how an objects orientation usually changes in the time it takes to leave the detection area by translational motion. As a result, if $D_\varphi/a_\varphi^2 \ll D/a^2$ rotational steps will scarcely occur on these time scales and a translational ACF following Eq. (4.1) will emerge. If $D_\varphi/a_\varphi^2 \gg D/a^2$, on the other hand, the object will almost exclusively rotate. In the limiting case, i.e., when the object will experience no translational displacements at all, only those starting positions contribute to the ACF, that are also contained in the target detection area, see shaded area in Fig. 5.1 (a). Following Eq. (A.7), the ACF for purely rotational diffusion is then given by

$$C(t) = c \int_0^{2\pi} \frac{A_\cap(\varphi)}{\sqrt{4\pi D_\varphi t}} \exp\left(-\frac{\varphi^2}{4D_\varphi t}\right) , \qquad (5.1)$$

where $p(\varphi) = \exp(-\varphi^2/4D_\varphi t)(4\pi D_\varphi t)^{-1/2}$ is the free azimuthal rotational diffusion propagator and $A_\cap(\varphi)$ the intersection between starting and target detection area. For small t the diffusion propagator becomes the Dirac Delta function $\delta(\varphi)$ and $A_\cap(\varphi = 0) = L_\mathrm{s} \times L_\mathrm{l}$ the full rectangular detection area, resulting in $C(0) = cL_\mathrm{s}L_\mathrm{l}$.

Application to simulation data

The autocorrelation functions of simulated time series, that contained uncoupled translational and rotational displacements, for three different rotational diffusion coefficients D_φ and fixed $D_\mathrm{in} = 0.10$ (Conf. M00-M03) are shown by the symbols in Fig. 5.2. As long as $D_\varphi/a_\varphi^2 \ll D/a^2$ the ACF is consistent with the solution of Eq. (4.1), resulting in $D = 0.10 \pm 0.01$. For the values underlying the ACF displayed by squares $(D/a^2 = 20 D_\varphi/a_\varphi^2)$ the object will typically rotate by only $\varphi = 0.5$ before leaving the detection area due to translation. With increasing rotational diffusion coefficients, starting with $D_\varphi/a_\varphi^2 \approx D/a^2$, a kink becomes visible in the ACF, indicating implications of rotational diffusion. While the short time regime is governed by rotational and translational motion equally here, for $D_\varphi/a_\varphi^2 \gg D/a^2$ rotational diffusion gains dominance and the kink steadily becomes more distinctive. For the ACF represented by diamonds $(D/a^2 = 0.5 D_\varphi/a_\varphi^2)$ the suggested comparison of typical times yields a rotation by $\varphi = 3.5$, i.e., a half turn, in the time it takes to leave the detection area by translation. In case of the circles $(D/a^2 \approx 0.06 D_\varphi/a_\varphi^2)$ this value has increased to more than a full turn $(\varphi = 10.4)$ and therefore the rotation is dominant to such an extent, that the kink can be described by Eq. (5.1). A non-linear Levenberg-Marquardt fit with this approximation yields a rotational diffusion coefficient of $D_\varphi = 0.809 \pm 0.002$, which is in quite good agreement with the input value of $D_{\varphi,\mathrm{in}} = 0.711$.

When handling experimental data, the course of action is straightforward. As long as no kink is visible in the ACF $D_\varphi/a_\varphi^2 \ll D/a^2$ can be safely assumed and by using Eq. (4.1) the translational diffusion coefficient can be determined. Whenever the kink is visible a fit with Eq. (5.1) can be attempted. Should the rotational and translational diffusion coefficient be comparable even the best fit with Eq. (5.1) will not match the data, because the approximation is not valid yet, cf. the dotted line in Fig. 5.2 for the diamonds. Here, one would have to resort to the cumbersome full solution [Eq. (A.7) in the appendix]. If the slopes match on both sides of the kink the regime of $D_\varphi/a_\varphi^2 \gg D/a^2$ is reached and a non-linear fit with the approximation Eq. (5.1) will give the rotational diffusion coefficient.
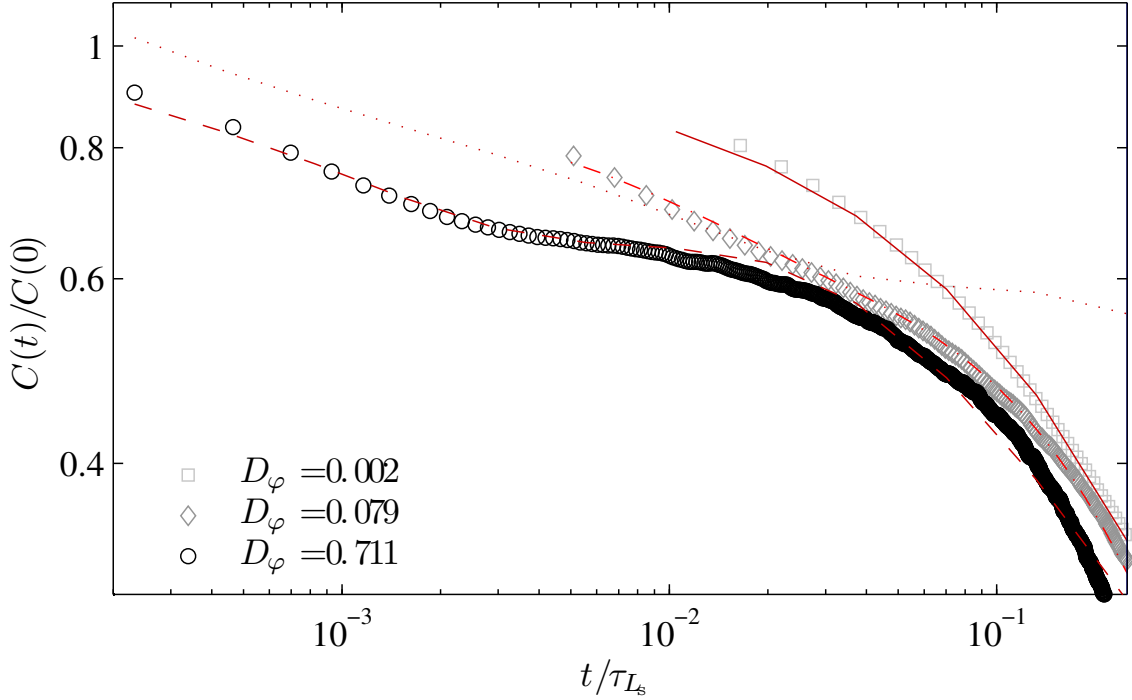
Figure 5.2: Autocorrelation functions for uncoupled rotational and translational diffusion with different D_φ and constant $D = 0.1$ (Conf. M00-M03). For $D_\varphi/a_\varphi^2 \ll D/a^2$ (□) rotational diffusion has no influence on the ACF and it can be described by Eq. (4.1) (solid line). If $D_\varphi/a_\varphi^2 \geq D/a^2$ (◇), a kink appears at approximately a_φ^2/D_φ. If $D_\varphi/a_\varphi^2 \gg D/a^2$ (○), the behavior can be described using the approximation in Eq. (5.1) (dashed line). The dash dotted line marks the full solution [Eq. (A.7) in the appendix] when using the input parameters for ◇ (Nearly congruent with the other lines for □ and ○).

5.2 Residence time distribution

To get an insight, how the rotational diffusion will affect the residence time distribution [‡], first solely rotational movements of a single object at distance r from the probe will be studied. For the analysis for this situation it is convenient to consider the equivalent problem of a fixed molecule center and a probe performing jumps of size ra_φ on a concentric circle around the center. Clearly, considering the inner and outer circle in Fig. 5.1 (b) the signal is always "on", if $r < r_{\min} \equiv L_s/2$, while for $r > r_{\max} \equiv (L_s^2 + L_l^2)^{1/2}/2$ it is alway

off. For radii $r_{\min} < r < r_{\max}$, a signal alternating between "on" and "off" states can be obtained. For a given r, the "on" status refers to the probe being located on certain arcs of the circle with radius r. As sketched in Fig. 5.1 (c), two opposing arcs of equal length are present, if $r_{\min} < r \le L_l/2$, while for $L_l/2 < r < r_{\max}$ four equivalent arcs close to the vertices of the rectangle appear. In analogy to the detection areas considered before for the translational diffusion, the arcs form detection lines with length l_r, that can be obtained by simple geometric reasoning:

$$l_r = \begin{cases} 2r \; \arcsin\left(\frac{L_s}{2r}\right), & r_{\min} < r \le L_l/2, \\ r \left[\arcsin\left(\frac{L_s}{2r}\right) - \mathrm{acos}\left(\frac{L_l}{2r}\right)\right] & L_l/2 < r < r_{\max}. \end{cases} \tag{5.2}$$

For jump lengths ra_φ much smaller than l_r the problem of a diffusing tip on a line of length l_r with absorbing boundaries can be considered for calculating the RTD. The initial distribution is concentrated on two points at distance $r\Delta_\varphi$ from the boundaries. After determination of the the respective one-dimensional diffusion propagator $p(x, t)$, see appendix A.5, the first passage time distribution under the condition of a fixed object-probe-distance r is calculated, as usual, by $\psi_{\mathrm{rot}}(t|r) = -\partial_t \int_0^{l_r} \mathrm{d}x \; p(x, t)$ yielding

$$\psi_{\mathrm{rot}}(t|r) = \frac{4D_\varphi}{\pi} \sum_{n=0}^{\infty} \frac{q_n^2 \sin(q_n \Delta_\varphi)}{(2n+1)} \exp\left(-q_n^2 D_\varphi t\right), \tag{5.3}$$

where $q_n = q_n(r) = (2n+1)\pi r/l_r$. After averaging over all positions between $r_{\min}$ and $r_{\max}$, taking into account that 2 equivalent arcs exist for $r_{\min} < r < L_l/2$ and four equivalent arcs for $L_l/2 < r < r_{\max}$, the RTD

$$\psi_{\mathrm{rot}}(t) = \mathcal{N}^{-1} \left[\int_{r_{\min}}^{L_l/2} \mathrm{d}r \; r \; \psi_{\mathrm{rot}, l_r}(t|r) + 2 \int_{L_l/2}^{r_{\max}} \mathrm{d}r \; r \; \psi_{\mathrm{rot}, l_r}(t|r) \right] \tag{5.4}$$

is obtained, with the normalization factor $\mathcal{N} = \pi L_l^2/4$. Analogously to the previous treatment of translational diffusion Eq. (5.4) is based on a continuum theory. Therefore, $\tau_{\Delta_\varphi} \equiv \Delta_\varphi^2/D_\varphi$ again defines a lower limit for its applicability. To account for the effect of the finite jump length for detection lines with small length l_r, one would have to deal with a rather complex situation, among others, with very small numbers of just $1 - 2$ probe positions, whose precise location depends on r and Δ_φ. After averaging of r these effects of the discreteness of the jump length are, however, washed out.

In the presence of both rotational and translational diffusion, it is difficult to obtain exact analytical results for the RTD, because the problem cannot be described as a diffusion problem with a time-independent geometry of the absorbing boundary. Fortunately, in the situation, where rotational diffusion is relevant in the RTD, the results obtained for pure translation and pure rotation are sufficient to account for the overall behavior.

As discussed above, the signal can turn from "on" to "off" due to rotational moves, only if the molecule center is in the shaded area $r_{\min} < r < r_{\max}$ in Fig. 5.1 (a). A typical arc in this area has an angle of about $\pi/4$ to $\pi/2$, compare Fig. 5.1 (c), which results in a typical time $\tau_\varphi \equiv (\pi/4)^2/2D_\varphi$ for the object to to leave the detection area by rotation. The typical time for an object to center to traverse the shaded area in in Fig. 5.1 (b) is $\tau_{\mathrm{tr}} \equiv (L_l/2 - L_s/2)^2/4D$. Hence, if $\tau_\varphi \gg \tau_{\mathrm{tr}}$, the decay of the RTD should be governed by translational diffusion as described in chapter 4.2. However, if $\tau_\varphi \ll \tau_{\mathrm{tr}}$, the rotational diffusion should become significant. It governs the the RTD for short times $t \ll \tau_{\mathrm{tr}}$, while for $t \gg \tau_{\mathrm{tr}}$ the dominant events are those, where the object center enters the core

area $r \leq r_{\min}$ and leaves it by translational diffusion. Accordingly, the RTD becomes decomposable into one part given by pure rotational diffusion [Eq. (5.4)] and a second part given by pure translational diffusion [Eq. (3.11) with $R = r_{\min}$]. The lower limit for applicability, caused by the continuum approaches for translational as well as for rotational diffusion, will be given by the process reigning the short time regime. Excluding the indefinite cases, where $D_\varphi/a_\varphi^2 \approx D/a^2$, it can be assessed by $t \geq \min(\tau_\Delta, \tau_{\Delta_\varphi})$.

Application to simulation data

In Fig. 5.3 representative RTDs in the presence of both rotational and translational diffusion are displayed for a rectangular object of size 10×5 for three $a^2 D_\varphi/a_\varphi^2 D$ ratios (Conf. M00-M03). For $a^2 D_\varphi/a_\varphi^2 D = 0.05$ ($\tau_\varphi/\tau_{\mathrm{tr}} = 10 \gg 1$) rotational diffusion indeed has no influence and the RTD can be described by Eq. (4.4) (dashed line). For $a^2 D_\varphi/a_\varphi^2 D = 18$ ($\tau_\varphi/\tau_{\mathrm{tr}} = 0.03 \ll 1$), a double shoulder characterizes the distribution. This reflects the separation into the two time regimes governed by rotational and translational diffusion, as demonstrated by the the curves corresponding to Eq. (5.4) (solid line) and to Eq. (3.9) with $R = r_{\min}$ (dashed line). The relative weight of the two contributions was determined in the following way: By making the ansatz $\Psi(t) = B_1 \psi_{\mathrm{rot}} + B_2 \psi_{\mathrm{trans}}(t)$, the coefficient B_2 was first determined by fitting $\Psi(t) \approx B_2 \psi_{\mathrm{trans}}(t)$ to the long time regime, with ψ_{trans} taken from Eq. (3.11). Thereafter, the coefficients B_1 followed from the normalization of $\Psi(t)$. The small full symbols in Fig. 5.3 represent the distribution of residence times, during which the object center has entered the core area. These distributions are normalized to the overall fraction of the corresponding events. Their good agreement with the long time behavior of the overall RTD is further proof that this time regime is dominated by translational diffusion in the core area.

Generally, the influence of the rotational diffusional motion on the long time regime can always be captured by defining an effective radius R_{eff}, which follows from fitting the exponential decay in the long time regime to Eq. (3.11). The behavior of this effective radius as a function of $a^2 D_\varphi/a_\varphi^2 D$ is shown in the inset of Fig. 5.3. For $a^2 D_\varphi/a_\varphi^2 D = 0$, i.e., no rotational diffusion, $R_{\mathrm{eff}} = R'$ from Eq. (4.7) as discussed in chapter 4.4. With increasing $a^2 D_\varphi/a_\varphi^2 D$, R_{eff} decreases and rapidly approaches $R_{\mathrm{eff}} = r_{\min}$. When $R_{\mathrm{eff}} = r_{\min}$, the rotational moves are so fast that, if an object center leaves the core area, the recorded signal will almost immediately be turned "off". The radii $R_{\mathrm{eff}} > r_{\min}$ for $a^2 D_\varphi/a_\varphi^2 D \lesssim 1$ can be assigned to an effective circular detection area, which takes into account, that an object, when leaving the core area, typically diffuses over a certain distance before the signal is turned off because of a rotational move.

In this paragraph instructions will be given, how these findings can be applied to extract rotational and translational diffusion coefficients, if both types of motion are present. As discussed above, if $\tau_\varphi \gg \tau_{\mathrm{tr}}$ only translational diffusion coefficients can be determined from the RTD. When a double shoulder appears in the RTD for $\tau_\varphi \lesssim \tau_{\mathrm{tr}}$, the rotational diffusion coefficient should be determinable. In fact, using a non-linear Levenberg-Marquardt fitting of Eq. (5.4) to the shoulder in the short time regime, $D_\varphi = 0.080 \pm 0.001$ for the diamonds and $D_\varphi = 0.720 \pm 0.001$ for the circles are obtained, which agree well with the respective input values of $D_{\varphi,\mathrm{in}} = 0.079$ and $D_{\varphi,\mathrm{in}} = 0.711$. Simultaneously, by fitting Eq. (3.11) to the shoulder on the long time regime, $\tilde{D}$ values are determined. Initially, $R_{\mathrm{eff}} = r_{\min}$ can be chosen for this analysis. If the resulting $a^2 D_\varphi/a_\varphi^2 \tilde{D}$ turns out to be larger than one, $\tilde{D}$ should have a reliable value. However, if $a^2 D_\varphi/a_\varphi^2 \tilde{D} \lesssim 1$, the $\tilde{D}$ value is underestimated, because the effective radius R_{eff} is larger than $r_{\min}$. For the data pre-

sented in Fig. 5.3 $\tilde{D} = 0.06 \pm 0.00$ for the diamonds and $\tilde{D} = 0.07 \pm 0.01$ for the circles were obtained, which in connection with the determined D_φ values give $a^2 D_\varphi / a_\varphi^2 D = 3.4$ and 26.1, respectively. Both D agree quite well with the input $D_{\mathrm{in}} = 0.1$, with a bigger difference in case of $a^2 D_\varphi / a_\varphi^2 D \approx 1$. Like indicated by this example the deviation usually is small, because it was observed that R_{eff} and $r_{\min}$ do not differ much, as soon as the double shoulder can be clearly identified. In practice it will be generally unlikely to encounter this deviation, because of the narrow regime $a^2 D_\varphi / a_\varphi^2 D$, where rotational effects are visible and R_{eff} is larger than $r_{\min}$. If the problem is nevertheless present, the experimentalist may shift the $a^2 D_\varphi / a_\varphi^2 D$ value to the favorable regime by changing the temperature. An similar evaluation for a translational diffusion coefficient of $D = 0.25$ is given in reference [‡].
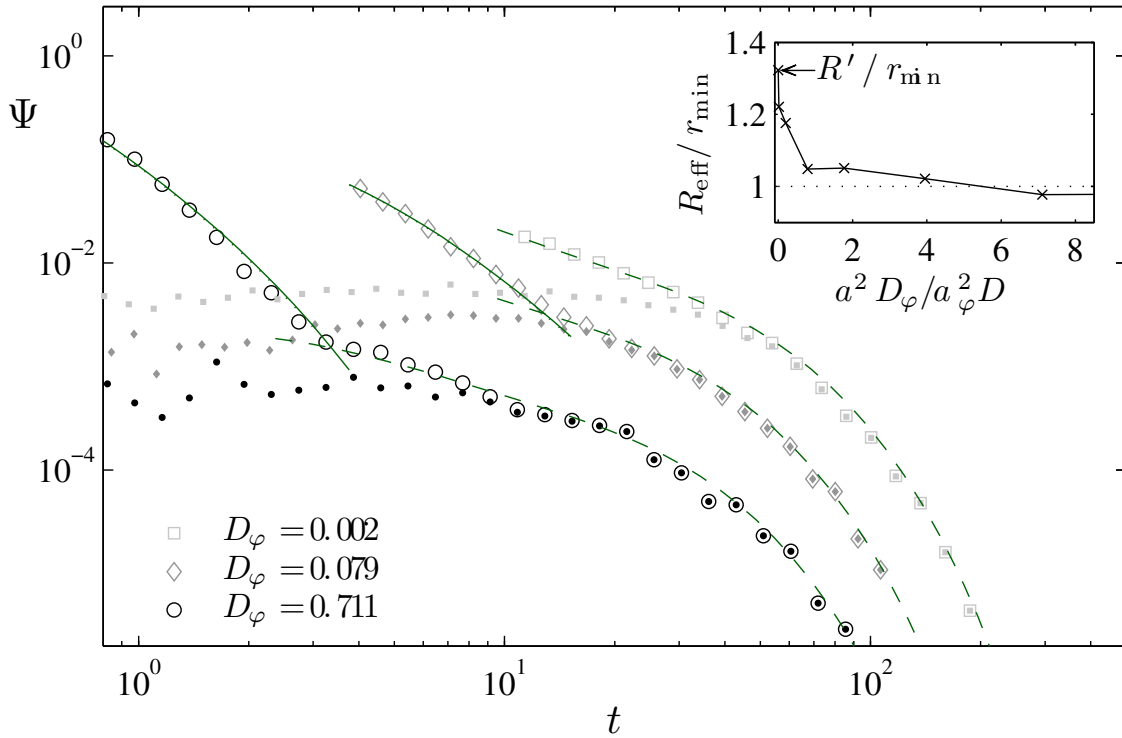
Figure 5.3: Residence time distributions for uncoupled rotational and translational diffusion with different D_φ and constant $D = 0.1$ (Conf. `M00-M03`, open symbols). Distributions are shown for times $t > \min(\tau_\Delta, \tau_{\Delta_\varphi})$ valid for evaluation. For $D_\varphi / a_\varphi^2 \ll D/a^2$ (□) rotational diffusion has no influence on the RTD and follows Eq. (4.4) (dashed lines). If $D_\varphi / a_\varphi^2 \geq D/a^2$ (◇,○), a double shoulder is visible. The left is caused by rotational diffusion [Eq. (5.4), solid line] and the right by translational diffusion [Eq. (3.9), dashed line]. Small solid symbols refer to the distributions of residence times, which belong to trajectories, where the object center has at least once entered the core area shown in Fig. 5.1 (b). Inset: Dependence of the effective radius R_{eff} on $a^2 D_\varphi / a_\varphi^2 D$.

5.3 Interpeak time distribution

Analogously to the RTD, first the implications of purely rotational diffusion on the ITD are investigated. In order to do so, again a probe performing jumps on concentric circles

$(r_{\text{min}} < r < r_{\text{max}})$ around the fixed object center are considered. Since, now the "off" times of the signal are relevant, the detection lines l_r, l_r' entering the general expression in Eq. (5.3) are given by the arcs outside the rectangle, represented by the thin lines in Fig. 5.1 (c). Their lengths are given by

$$
\begin{aligned}
l_r &= 2r \arccos\left(\tfrac{L_{\text{s}}}{2r}\right) & r_{\text{min}} < r \le r_{\text{max}}, \\
l_r' &= 2r \arcsin\left(\tfrac{L_{\text{l}}}{2r}\right) & L_{\text{l}}/2 < r \le r_{\text{max}}.
\end{aligned} \tag{5.5}
$$

Taking into account, that two equivalent arcs exist for $r_{\text{min}} < r < L_{\text{l}}/2$ and this time four pairwise equivalent arcs for $L_{\text{l}}/2 < r \le r_{\text{max}}$, the averaging of Eq. (5.3) over all positions between r_{min} and r_{max} results in

$$
\psi_{\text{rot}}(t) = \mathcal{N}^{-1} \left[\int_{r_{\text{min}}}^{r_{\text{max}}} \mathrm{d}\, r\ r\ \psi_{\text{rot},l_r}(r,t) + \int_{L_{\text{l}}/2}^{r_{\text{max}}} \mathrm{d}\, r\ r\ \psi_{\text{rot},l_r'}(r,t) \right]. \tag{5.6}
$$

Corresponding to the findings for the RTD in chapter 5.2, the ITD should also be decomposable into a short time regime $t < \tau_{\text{tr}}$ governed by rotational diffusion and a long time regime $t > \tau_{\text{tr}}$ governed by translational diffusion, if the typical times for leaving the detection area by a certain type of motion behave as $\tau_\varphi \ll \tau_{\text{tr}}$. In this case the time regimes should follow Eq. (5.6) and Eq. (3.16) with an radius of $R = r_{\text{max}}$, respectively. For $\tau_\varphi \gg \tau_{\text{tr}}$ rotational diffusion should not affect the ITD, so that Eq. (3.14) and Eq. (3.16) with $R = R''$ can be considered for evaluation in the corresponding time regimes. The lower time limit for application of the continuum treatment is analogous to the RTD given by $t \ge \min(\tau_{\text{max}}, \tau_{\Delta_\varphi})$.

For correct description of the translational diffusion when $D_\varphi/a_\varphi^2 \approx D/a^2$ ($\tau_{\text{tr}} \approx \tau_\varphi$) an effective radius is introduced during the treatment of the RTD. It shrinks from R' [Eq. (4.7)] in case of $D_\varphi = 0$ to r_{min} for $D_\varphi/a_\varphi^2 \ll D/a^2$, accounting for the decreasing effective distance an object center can leave the core area, without leaving the detection area due to a rotational step, see discussion in chapter 5.2. A similar consideration is necessary for the ITD, only that the effective radius increases here. When $D_\varphi = 0$ the object center can typically approach the tip up to its detection area's radius R'' [Eq. (4.8)] before being noticed by the tip. With increasing rotation the tip will sense the object earlier and the objects size seemingly increases. In the limiting case $D_\varphi/a_\varphi^2 \ll D/a^2$ the object at last cannot get closer than r_{max} to the tip without turning the signal on.

Application to simulation data

Figure 5.4 illustrates the ITDs of three different $a^2 D_\varphi/a_\varphi^2 D$ ratios (Conf. M00 - M03). For $a^2 D_\varphi/a_\varphi^2 D = 0.05$ ($\tau_\varphi/\tau_{\text{tr}} = 10 \gg 1$, squares) rotational diffusion has, as expected, no influence on the ITD and it can be described by Eq. (3.16) (dashed line) in the long time regime and approximately by Eq. (3.14) (dotted line) in the short time. At $a^2 D_\varphi/a_\varphi^2 D = 18$ ($\tau_\varphi/\tau_{\text{tr}} = 0.03 \ll 1$, circles) an additional shoulder emerges in the short time regime ($t < \tau_{\text{tr}}$) of the distribution depicting the influence of the rotational diffusion. It can be described by Eq. (5.6) and the exponential decay at long times by Eq. (3.16) with an object size of $\tilde{A} = \pi r_{\text{max}}^2$. A non-linear Levenberg-Marquardt fit yields an rotational diffusion coefficient of $D_\varphi = 0.715 \pm 0.002$ and a linear regression of the exponential decay in the long time regime a translational diffusion coefficient of $D = 0.09 \pm 0.05$, which both are in good agreement with the input values of $D_{\varphi,\text{in}} = 0.711$ and $D_{\text{in}} = 0.1$ respectively. In the third example, which represents the intermediate regime of $a^2 D_\varphi/a_\varphi^2 D = 2 \approx 1$

(diamonds), the additional shoulder is not as obvious, because of the similar shape of the purely translational ITD in this time regime. Nevertheless, it can be used to extract a rotational diffusion coefficient of $D_\varphi = 0.075 \pm 0.002$ via non linear fitting, which matches the input value of $D_{\varphi,\text{in}} = 0.079$. The evaluation of the long time regime yields a translational diffusion coefficient of $D = 0.09 \pm 0.01$ again using $R_{\text{eff}} = r_{\text{max}}$, which matches the input value of $D_{\text{in}} = 0.10$. The inset of of Fig. 5.4 indeed shows, that the interval of $a^2 D_\varphi / a_\varphi^2 D$ ratios, where R_{eff} is between R'' and r_{max}, is even narrower than the critical interval of the RTD. Therefore, in practice it is safe to assume $R_{\text{eff}} = r_{\text{max}}$ upon evaluating the long time regime $t \gg \tau_c$, whenever the second shoulder in the short time regime of the ITD is clearly identifiable, and $R_{\text{eff}} = R''$ otherwise.
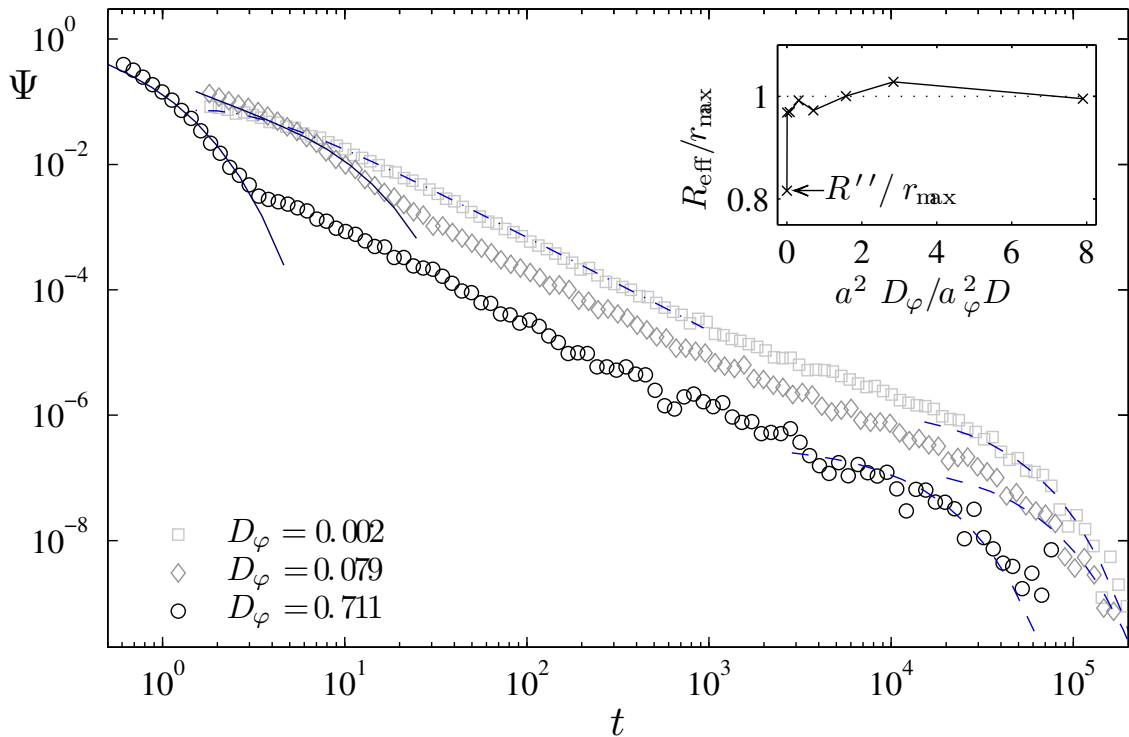
Figure 5.4: Interpeak time distributions for uncoupled rotational and translational diffusion with different D_φ and constant $D = 0.1$ (Conf. M00-M03, open symbols). Distributions are shown for times $t > \min(\tau_\Delta, \tau_{\Delta_\varphi})$ valid for evaluation. For $D_\varphi \ll D/a^2$ (□) rotational diffusion has no influence on the RTD and can be described by Eq. (3.13) in the short time regime (dash-dotted line) and Eq. (3.16) in the long time regime (dashed line). If $D_\varphi \geq D/a^2$ (◇,○), a shoulder caused by rotational diffusion [Eq. (5.6), solid line] appears in the short time regime. The long time regime is governed by translational diffusion [Eq. (3.16), dashed line]. (b) Dependence of the effective radius R_{eff} on D_φ / Da^2.

5.4 Assessment of the methods

In this chapter the effects of additional rotational diffusion on the ACF, RTD and ITD have been addressed. Though their curves are strongly influenced by rotational diffusion the determination of diffusion coefficients is not hampered significantly. On the contrary, it is rather extended to the possibility to simultaneously determine the translational and

rotational diffusion coefficient underlying a given time series. A comparison of the typical times for either type of motion discloses, that within the representations time regimes can be identified, that are each governed by only one kind of diffusion. As a result, these time regimes can be independently evaluated with the solution for pure rotational and pure translational diffusion, respectively. This implies that also exclusively rotational diffusion could be treated. From the experimental point of view the tip would have to be specifically positioned in a fixed distance between $r_{\min}$ and $r_{\max}$ from the rotating objects center to record a time series here, because otherwise the objects, lacking translational motion, will not reach the tip. In the theory the averaging over all possible r in Eq. (5.4) and Eq. (5.6) then becomes needless. In the treatment of the ACF only the rotational diffusion propagator has to be considered and corresponding detection lines would replace the detection areas.

Note, that the time series of circular objects will of course shown none of the effects described in this chapter. But also in case of quadratic molecules there will be only minor effects, if it all. For example, in the presented simulation setup the interval between $r_{\max}$ and $r_{\min}$ in case of a 5×5 square molecule approximately equals the translational step size and it is very unlikely to hit a distance relevant for rotation here. Therefore, as illustrated in Fig. 5.5, ACF, RTD and ITD show no sign of rotation, even in case of $D_\varphi = 0.711$ ($D = 0.1$, Conf. M04), where in the previous discussions for a 10×5 object a massive influence of the rotation was visible.
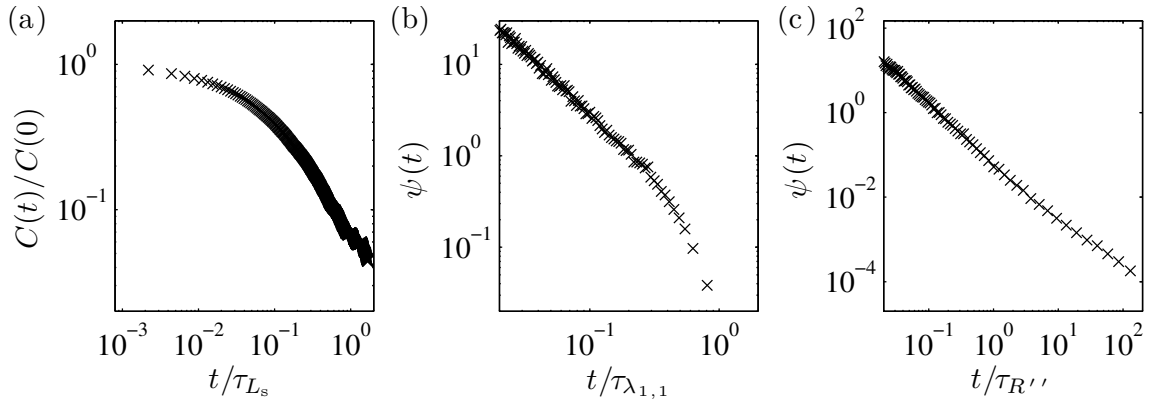
Figure 5.5: (a) ACF, (b) RTD and (c) ITD of a square object of size 5×5 with $D_\varphi = 0.711$ ($D = 0.1$) (Conf. M04). Despite the high $a^2 D_\varphi / a_\varphi^2 D$ ratio no signs that would indicate rotational diffusion, i.e., no kink in the ACF nor double shoulders in the RTD or ITD, are visible.

While in general all three methods are suited to determine the governing diffusion coefficient of a rectangular object in the respective time regime as displayed in Tab. 7.1, a ranking of eligibility can be made. The ACF is the weakest link, here, because it has only a small time interval valid for evaluation due to neglecting the cross correlations. This time regime then usually is governed by one type of motion and therefore only this one diffusion coefficient can be determined. In the worst case of of $a^2 D_\varphi / a_\varphi^2 D \approx 1$ one would have to resort to the extensive fitting with the full solution [Eq. (A.2) in the appendix]. Because of the characteristic kink the ACF can be recommended as a quick and reliable check, whether rotational diffusion is present, but it is not convenient for the simultaneous determination of both diffusion coefficients. The identification of rotational diffusion in the ITD becomes vague in case of $D_\varphi / a_\varphi^2 \gtrapprox D / a^2$, because the curves in the short time

regime with and without rotation are very similar, so that rotational motion might be overlooked. Another drawback of the ITD is, that the time regime $t \gg \tau_c$ is necessary for simultaneously determining the translational diffusion coefficient, which might be not resolved satisfactorily in case of small θ. Anyway, if the parameters are not in one of these adverse, but unlikely, ranges, the ITD can unlike the ACF be used to simultaneously determine the rotational and translational diffusion coefficients. Among the presented approaches the RTD, however, is favorable. It is not only based on a sufficiently small time interval to reliably resolve the translational diffusion governed and the rotational diffusion governed time regimes, but the regimes can also be distinguished best, in form of a distinct double shoulder.

	$\mathbf{D}_\varphi$	$\mathbf{D}$	$\mathbf{D}_\varphi$	$\mathbf{D}$	$\mathbf{D}_\varphi$	$\mathbf{D}$
input	0.002	0.10	0.079	0.10	0.711	0.10
ACF	—	0.10 ± 0.01	—	—	0.809 ± 0.002	—
RTD	—	0.12 ± 0.01	0.080 ± 0.001	0.06 ± 0.00	0.720 ± 0.001	0.07 ± 0.01
ITD	—	0.10 ± 0.01	0.075 ± 0.002	0.09 ± 0.01	0.715 ± 0.002	0.09 ± 0.05

Table 5.1: Simultaneously determined translational and rotational diffusion coefficients.

Chapter 6

Anisotropic diffusion

The treatment so far was based on the assumption of an isotropic diffusion coefficient. In the anisotropic case the diffusive motion is characterized by a diffusion tensor [77].

As far as the RTD for rectangular object is concerned, this tensor can be readily implemented, in case the principle axes of the diffusion tensor are parallel to the object's edges

$$\psi\left(t\right) = \frac{L_1 L_s}{\pi^2} \sum_{m,n=0}^{\infty} \frac{c_{\mu,\nu} \lambda'^2_{\mu,\nu}}{\mu\nu} \exp\left(-\lambda'^2_{\mu,\nu} t\right) . \tag{6.1}$$

The coefficients $c_{\mu,\nu}$ are equivalent to Eq. (4.3) with $\mu = (2m + 1)$ and $\nu = (2n + 1)$, but the eigenvalues $\lambda'^2_{\mu,\nu} = D_x \mu^2 \pi^2 / L_1^2 + D_y \nu^2 \pi^2 / L_s^2$ additionally depend on D_x and D_y here. Ikonomov *et al.* [39] surmised that this expression would suffice to identify a difference in D_x and D_y, representing the diffusion coefficients parallel to the short and long edge of the object respectively.

Equation (6.1) indeed contains two exponential functions with the typical times $\tau_x \equiv L_1^2 / \pi^2 D_x$ and $\tau_y \equiv L_s^2 / \pi^2 D_y$. Usually, the long time regime $\tau_x, \tau_y \ll t$ is used for fitting, where $\mu = \nu = 1$ are the leading terms of the sum. Its logarithmic representation is reduced to a single linear equation $\log(\psi(t)) \sim \log(L_1 L_s c_{1,1} \lambda'^2_{1,1} / \pi^2) - \lambda'^2_{1,1} t$ with slope $-\lambda'^2_{1,1}$. If de facto $D_y \neq D_x$, anisotropic diffusion could not be recognized in this time regime and treatment with Eq. (4.4) would result in a misleading effective diffusion coefficient.

If the object has a high aspect ratio or if D_x and D_y differ strongly, a time regime $\tau_x \ll t \ll \tau_y$ (or $\tau_y \ll t \ll \tau_x$) emerges, where the behavior of Eq. (6.1) would deviate considerably from that of Eq. (4.4). This could be used as an indicator for anisotropic diffusion. However, this time regime is not favorable for evaluation, because of the complex functional form of Eq. (6.1) and the fact that the short time regime of the RTD often is very noisy, c.f. chapter 7.

Generally speaking, resolving anisotropic diffusion by evaluating the signal of a point-like probe is very difficult and limited to setups, where τ_x and τ_y define a distinct additional time regime. Hence, better suited measurement techniques are desirable, which are sensitive to the direction of the diffusion. In the following modifications of the measurement setup will be discussed, which can be used to account for anisotropic diffusion properties.

6.1 Extended linear probe

Assuming the probe was not a single point, but rather an infinite extended line, directional information could be easily obtained. Because displacements parallel to the probe would not influence the signal, an analysis of the recorded signal would only give information on an object's diffusion perpendicular to the line, compare Fig. B.2 in the appendix. By changing the orientation of the linear tip every favored direction could be probed.

Since this measurement setup will also record a time series toggeling between "on" and "off", the principles of the RTD can be employed for evaluation. The problem of deriving the diffusion propagator used in the RTD is conveniently reduced to solving the one-dimensional diffusion equation between two absorbing boundaries, as done in appendix A.5. It gives

$$\psi\left(t\right) = \sum_{n=0}^{\infty} \frac{4D_{\perp}q_n^2}{(2n+1)\pi} \sin\left(q_n\Delta\right) \exp\left(-D_{\perp}q_n^2 t\right) , \qquad (6.2)$$

with $q_n = (2n+1)\pi/L$ and $D_{\perp}$ the effective diffusion coefficient in the direction perpendicular to the probe. The length of the detection line L, i.e. the width of the detection area, depends on the orientation $\bar{\gamma} \in [0, \pi/2]$ of the object in relation to the probe line

$$L\left(\bar{\gamma}\right) = L_{\mathrm{s}} \sin\left(\bar{\gamma}\right) + L_{\mathrm{l}} \cos\left(\bar{\gamma}\right) , \qquad (6.3)$$

compare the sketch in Fig. 6.1 (a). Note, that due to symmetry reasons a consideration of $0 \leq \bar{\gamma} \leq \pi/2$ is sufficient, here. Of course, this approach works fine with circular objects, too, by defining $L = 2R$ independent of the probe's orientation. The effective diffusion coefficient $D_{\perp}$ is then obtained by a linear regression of the RTD's exponential decay at $t \gg \tau_L \equiv L^2/\pi^2 D_{\perp}$ with

$$\psi\left(t\right) \sim \frac{4D_{\perp}\pi}{L^2} \sin\left(\frac{\pi\Delta}{L}\right) \exp\left(-D_{\perp}\frac{\pi^2}{L^2}t\right) . \qquad (6.4)$$

This is the leading term from Eq. (6.2) in the long time regime. Again, the minimal penetration depth of Δ has to be considered here, which defines a lower time limit τ_{Δ}, where the continuum approach holds true. It does not affect the fitting in the time regime $t \geq \tau_L$.

The RTD is derived for a single particle diffusing in the detection area. In practice, however, more than one object will diffuse on the surface. With increasing length of the probe, which enlarges the detection area, the risk of another object entering the latter rises. Hence, the idealized situation of an infinite extended tip is unfit for practical use and a probe with finite length and its corresponding detection area $\mathcal{D} \equiv \Lambda \times L$ will be considered from now on.

To find a reasonable size of the detection area $\mathcal{D}$, two aspects have to be taken into account. On the one hand, $\mathcal{D}$ should be as small as possible to not endanger the single particle consideration, as mentioned above. On the other hand, its aspect ratio should be as large as possible, so that objects preferably enter and leave through the long edges of $\mathcal{D}$. This way the the one-dimensional approach on evaluation, which is discussed above, still holds true. In the following the probabilities of both aspects with respect to the size of the detection area will be derived. Comparison results in a good estimation of the optimal probe length.
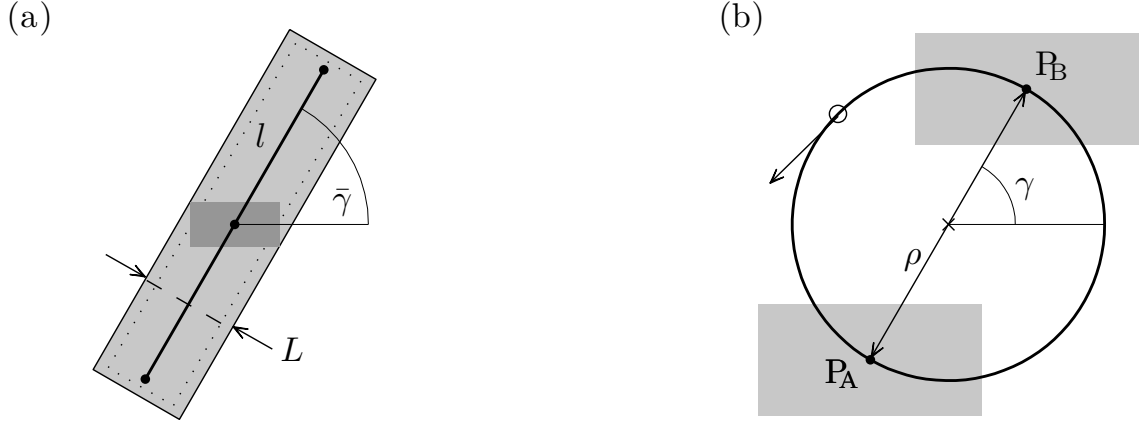
(a)

(b)

Figure 6.1: Basic geometries of the modified measurement setups: (a) A linearly extended tip of length $2l$ with the corresponding detection area (shaded area) of with L [Eq. (6.3)]. The minimal penetration depth Δ is indicated by the dotted line. (b) Two separate probing sites P_A and P_B in distance 2ρ. To avoid overlap of the detection areas (shaded areas), $\rho \gtrsim r_{max}$ should be chosen. Both setups are sensitive for diffusion along the γ-direction respective to the x-axes ($\gamma = \bar{\gamma} - \pi/2$).
The linear probe in (a) can be realized by a point-like probe oscillating between the turning points $\pm l$ from the idle position. The signal of an extended probe is reconstructed according to Fig. 6.3 (a). The two close, but separate, probing sites in (b) can be realized by a point-like probe rotating on a circle of radius ρ around the idle position half way between P_A and P_B. The signal at the probing sites can be extracted according to Fig. 6.3 (b) and (c).

To quantify the probability to find more than one object in $\mathcal{D}$, first the probability P_1 to find one marked object inside $\mathcal{D}$ has to be considered, which is defined by $P_1 \equiv \mathcal{D}/A = \mathcal{D}\theta/N\tilde{A}$. Here N is the number of objects of size $\tilde{A}$ on the surface A, which are connected via $A = N\tilde{A}/\theta$, compare Eq. (2.3). The probability $P_{>1}$ to find more than one object in $\mathcal{D}$ then follows from the binomial distribution, compare chapter 2.1,

$$P_{>1} = \left[1 - (1 - P_1)^N - NP_1 (1 - P_1)^{N-1}\right] . \tag{6.5}$$

For the one-dimensional approach, objects should preferably neither enter nor leave through the short edges of the detection area. In continuum the probability $P(L, \text{in}) = L/(L + \Lambda)$ to enter through one of the short edges of $\mathcal{D}$, denoted by "L,in", follows directly from its aspect ratio, since all entry positions are equally probable. However, even if an object has entered the detection area through a longer edge ($P(\Lambda, \text{in}) = 1 - P(L, \text{in})$), denoted by "$\Lambda$,in", there is a certain probability, that it will leave through one of the shorter ones, denoted by "L,out". The probability for an object center to reach one of the detection area's short edges, after starting in the point (x,y) inside the detection area [78], is given by

$$\tilde{P}(x, y) = \frac{4}{\pi} \sum_{k=0}^{\infty} \frac{-1^k}{2k + 1} \frac{\cosh\left[(k + 1/2)\pi x/L\right] \cosh\left[(k + 1/2)\pi y/L\right]}{\cosh\left[(k + 1/2)\pi \Lambda/L\right]} . \tag{6.6}$$

It has to be summed over all possible starting positions along the long edges, $P(L, \text{out}|\Lambda, \text{in}) = \frac{1}{2\Lambda} \sum_{k=0}^{\infty} \int_{-\Lambda/2}^{\Lambda/2} dx \frac{1}{2}[\tilde{P}(x, -L/2 + \Delta) + \tilde{P}(x, L/2 - \Delta)]$. As a result, the

probability that the object's path will cross one of the shorter edges of the detection area is given by

$$P_{\text{short}} = P(L, \text{in}) + P(\Lambda, \text{in}) \ P(L, \text{out}|\Lambda, \text{in}). \qquad (6.7)$$

The shorter edge L of the detection area is defined by Eq. (6.3) and only Λ is variable. Its optimal value can be appraised from the intersection point of both opposing probabilities $P_{>1}$ and P_{short}, compare Fig. B.4 in the appendix. The length l of the probe itself follows from $\Lambda = 2l + L_{\text{s}}$ for $\bar{\gamma} = \pi/2$ and $\Lambda = 2l + L_{\text{l}}$ for $\bar{\gamma} = 0$. For intermediate $\bar{\gamma}$, $\Lambda = 2l + L_{\text{s}}$ should be a fair estimate.

Application to simulation data

Fig. 6.2 (a) shows the RTDs of 10×5 sized objects diffusing with $D_x = 0.25$ in x-direction and varying $D_y = 0.25$, 0.1 and 0.01 along in y-direction, see configurations Conf. A00-A02. For each set, simulations with a linear tip of length $2l = 40$ at $\bar{\gamma} = 0$ and $\pi/2$ were carried out. To obtain the diffusion coefficients in the direction $\gamma = \bar{\gamma} + \pi/2$ perpendicular to the probe the exponential decay in the long time regime $t \gg \tau_L$ was evaluated with Eq. (6.4) and the respective $L(\bar{\gamma})$, which equal L_{l} and L_{s} following Eq. (6.3).
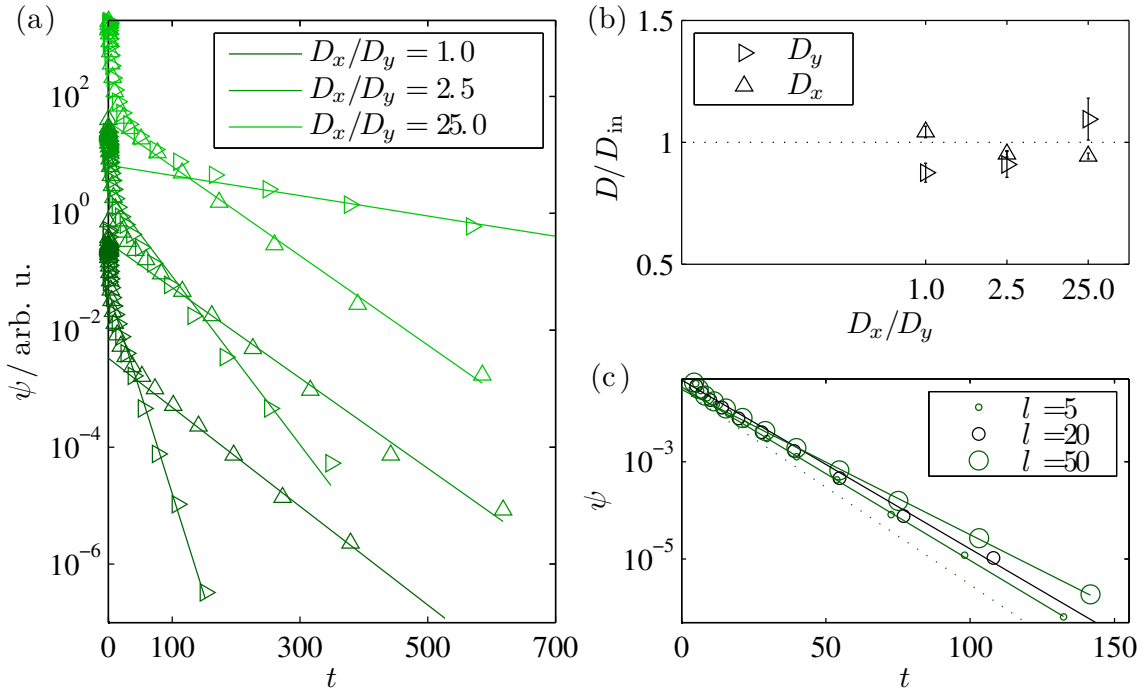
Figure 6.2: (a) RTDs of three different D_y/D_x ratios (Conf. A00-A02) recorded with an extended linear tip of length $l = 20$ at $\bar{\gamma} = 0$ ($\triangle$) and $\pi/2$ ($\triangleright$). The diffusion coefficients are obtained from a linear regression of the data in the long time regime with Eq. (6.4) (solid lines) using $L(\bar{\gamma})$ of Eq. (6.3). Data has been pairwise vertically shifted for better visibility here. (b) Fitted diffusion coefficients in relation to the respective input value. (c) Results for Conf. A00 and $\bar{\gamma} = 0$ for different probe lengths $l = 5, 20$ and 50. The distributions recorded with the shortest probe approach the solution for a two-dimensional detection area [Eq. (4.4), dotted line], because objects increasingly enter and leave through the short edges of the detection area. Those recorded with the longest probe contain many long peaks, which are caused by multiple objects in the detection area at the same time.

Though the tip length is not yet optimal, $l_{\rm opt} = 41$ cf. Fig. B.4 in the appendix, the resulting diffusion coefficients presented in Fig. 6.2 (b) and Tab. 6.1 are in good agreement with the input values for both directions. However, choosing a tip length farther from the optimal value, e.g. $2l = 10$ or 100, strongly increases the error of the results, see Fig. 6.2 (c). For the shorter probe the one-dimensional approximation starts to fail and the slope of the exponential decay approaches the one expected for a rectangular detection area. The slope in case of the longer probe is too flat in comparison to the expectation. The additional long time events included in the RTD here are caused by multiple objects entering the detection area.

	Conf. A00		Conf. A01		Conf. A02	
	D_x	D_y	D_x	D_y	D_x	D_y
$D_{\rm in}$	0.25	0.25	0.25	0.10	0.25	0.010
$\gamma \parallel x$	0.26 ± 0.01	—	0.24 ± 0.00	—	0.24 ± 0.00	—
$\gamma \parallel y$	—	0.22 ± 0.01	—	0.09 ± 0.01	—	0.011 ± 0.001

Table 6.1: Diffusion coefficients from evaluating the signal of a linear tip with $l = 20$.

Linearly oscillating probe

In practice the realization of an extended linear probe, which is still point-like in the cross-section on an atomic scale would be difficult and was so far not mentioned in the literature. However, this type of probe could be effectively realized by letting a single point probe oscillate with a frequency $\omega_{\rm lin}$ on a line. The period has to be short compared to the typical time τ_L for an object to cross the detection area to ensure identification of all passing objects. If this time is unknown prior to the measurement it can be estimated via a short control measurement according to chapter 3 or 4 with the probe locally fixed. The resulting rectangular signal then has to be coarse-grained on a grid corresponding to the time intervals $\Delta t \equiv \pi/\omega_{\rm lin}$ between the turning points in order to obtain the signal an extended probe would give.

As an example, Fig. 6.3 (a) illustrates the signal of a probe oscillating with $\Delta t \approx 0.3 \ll \tau_L = 400$ between the turning points at $\pm l = \pm 20$ relative to the idle position. Objects diffusing according to the parameters in Conf. A00 cause fluctuations in the signal recorded by the oscillating tip displayed by the solid black line. The solid gray line represent the virtual signal of an extended probe with length $2l$ after coarse graining the original signal with Δt. The signal of an actual extended probe in the same spot, shown by the dashed line, proofs the accuracy of this method.

A weakness of the linear extended probe is, besides the determination of the optimal probe length, that a new measurement is necessary for each spatial direction γ that is to be probed. Therefore, in the following chapter another point-probe trajectory will be introduced, that allows a simultaneous evaluation of the diffusion coefficient in arbitrary directions.
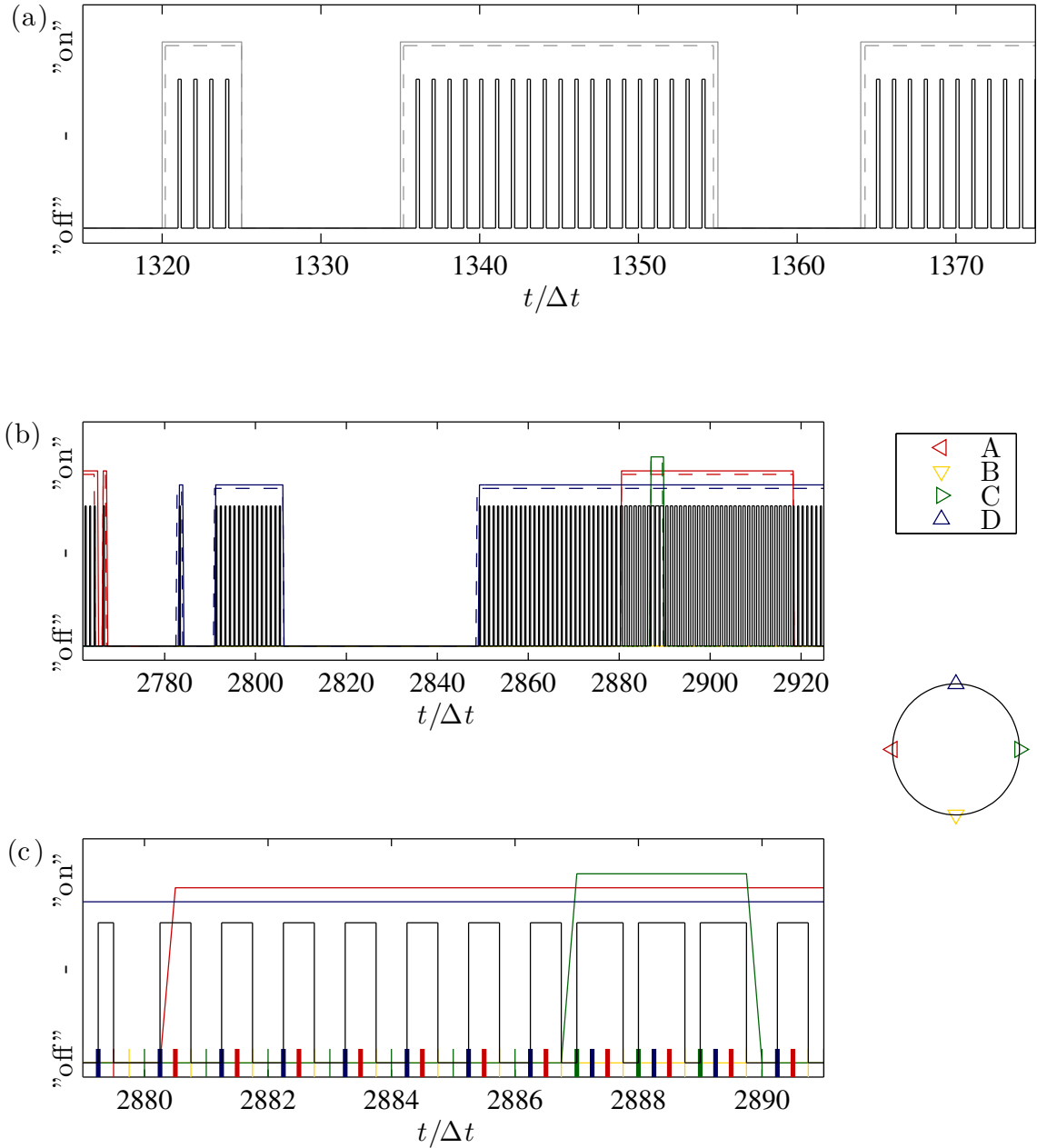
Figure 6.3: If the period of the moving probe is small compared to the typical time an object needs to cross the detection area, objects encountering the probe will repeatedly cause short peaks (solid black lines). (a) Exemplary signal of a probe oscillating with ω_{lin} on a line between the turning points $\pm l$ around the idle position. Discretizing the signal on a $\Delta t = \pi/\omega_{\text{lin}}$ grid, yields the virtual signal of an extended tip (solid gray line), which agrees very well with the signal of an actual extended tip (dashed gray line). (b) Extraction of the virtual signal (solid lines) in points A, B, C and D from the continuous signal of a probe rotating with ω_{circ} on a circle, see sketch. In each point $P(\rho, \gamma)$ the signal is updated only at $t = (\gamma + 2\pi n)/\omega_{\text{circ}}$ ($n \in \mathbb{N}$). In between the virtual probe is "blind" and keeps the previous status. The virtual signals agree very well with control signals (dashed lines) recorded by fixed probes in positions A-D. (c) Detailed cutout of (b). Ticks indicate the hit test in the respective points - bold ticks for "on" and thin ticks for "off".

6.2 Correlation between two separate probing points

Another possibility to gain directional sensitivity is the evaluation of the cross-correlation between the signals recorded at two separate points on the surface. Both measurement points $P_A(x_A, y_A)$ and $P_B(x_B, y_B)$ will define corresponding detection areas, compare Fig. 6.1(b). The cross-correlation function (CCF) is derived following the standard procedure described in appendix A.1, albeit using non-congruent detection areas and the free diffusion propagator for an anisotropic diffusion tensor from appendix A.4 in Eq. (A.5). It yields

$$
\begin{aligned}
C_{\text{cross}} \quad & (x_A, y_A, x_B, y_B, t) \qquad\qquad\qquad\qquad\qquad\qquad\qquad\qquad\qquad (6.8) \\
= \quad & c \int_{x_A - \frac{L_1}{2}}^{x_A + \frac{L_1}{2}} \mathrm{d}x_a \int_{y_A - \frac{L_s}{2}}^{y_A + \frac{L_s}{2}} \mathrm{d}y_a \int_{x_B - \frac{L_1}{2}}^{x_B + \frac{L_1}{2}} \mathrm{d}x_b \int_{y_B - \frac{L_s}{2}}^{y_B + \frac{L_s}{2}} \mathrm{d}y_b \frac{e^{-\frac{(x_b - x_a)^2}{4 D_x t}}}{\sqrt{4\pi D_x t}} \frac{e^{-\frac{(y_b - y_a)^2}{4 D_y t}}}{\sqrt{4\pi D_y t}} \\
= \quad & c \, C\left(x_B - x_A, D_x, L_1, t\right) \, C\left(y_B - y_A, D_y, L_s, t\right) ,
\end{aligned}
$$

with

$$
\begin{aligned}
C\left(\Delta, D, L, t\right) \;=\; & \sqrt{\frac{Dt}{\pi}} \left(e^{-\frac{(L+\Delta)^2}{4Dt}} - 2e^{-\frac{\Delta^2}{4Dt}} + e^{-\frac{(L-\Delta)^2}{4Dt}} \right) \qquad\qquad\qquad (6.9) \\
& - \frac{(L+\Delta)}{2} \operatorname{erf}\left(\frac{L+\Delta}{2\sqrt{Dt}}\right) + \Delta \operatorname{erf}\left(\frac{\Delta}{2\sqrt{Dt}}\right) + \frac{(L-\Delta)}{2} \operatorname{erf}\left(\frac{L-\Delta}{2\sqrt{Dt}}\right) .
\end{aligned}
$$

The origin of the employed coordinate system is, without loss of generality, set to the middle of the connection line between P_A and P_B, compare Fig. 6.1 (b). As a result, the points' location is defined by their distance 2ρ and the angle γ between the detection line and the x-axis, giving $\Delta x = x_B - x_A = 2\rho \cos\gamma$ and $\Delta y = y_B - y_A = 2\rho \sin\gamma$. Accordingly, $C_{\text{cross}} = C_{\text{cross}}(x_A, y_A, x_B, y_B, t)$ is written as $C_{\text{cross}} = C_{\text{cross}}(\rho, \gamma, t)$ in the following.

Application to simulation data

The solid lines in Fig. 6.4 show an overview of simulated CCFs of 10×10 objects diffusing with three different D_x/D_y ratios (Conf. A00-A02) as well as three different probe distances $\rho = 3, 7$ and 10 recorded at $\gamma = 0$ and $\pi/2$. The time axes are scaled with τ_{L_s} to get a feeling for the peak positions.

The overview illustrates how the correlation functions are affected by the distance between the measurement points. If $\rho < r_{\max} = (L_1^2 + L_s^2)^{1/2}$ the detection areas do not separate and $C_{\text{cross}}(t \to 0)$ approaches $\sim cA_\cap$, i.e., the expectation value for an object center to be inside the overlap area $A_\cap$. If $\rho > r_{\max} = (L_1^2 + L_s^2)^{1/2}$ the detection areas do not touch and $C_{\text{cross}}(t \to 0) \sim 0$. Here, the CCF is characterized by a single peak, whose position and height are related to the diffusion coefficients along the principal axis of the diffusion tensor. Hence, for evaluation purposes the radius should be chosen large enough for the detection areas to fully separate. For smaller ρ the differences of the correlations in both directions are marginal, see Fig. 6.4 (g)-(i), and the distinctive peak of the cross-correlation [Eq. (6.8)] is hidden in the flank arising from $C(0) \sim cA_\cap$. However, increasing the distance much beyond $r_{\max}$ is not recommended. With increasing ρ an object needs more time to translate from one measurement point to the other making it less likely that a signal in P_B was caused by the same object previously recorded in P_A. In the CCF this not only results in a delay of the correlation peak to larger times, but also in a decrease

of the absolute peak height. This eventually complicates the separation of the peak from the offset $C_{\text{offset}} = (cL_{\text{s}}L_{\text{l}})^2$, which is the constant probability that both probing sites are covered by different objects, compare the approximate treatment of the cross-correlation terms in appendix A.1.
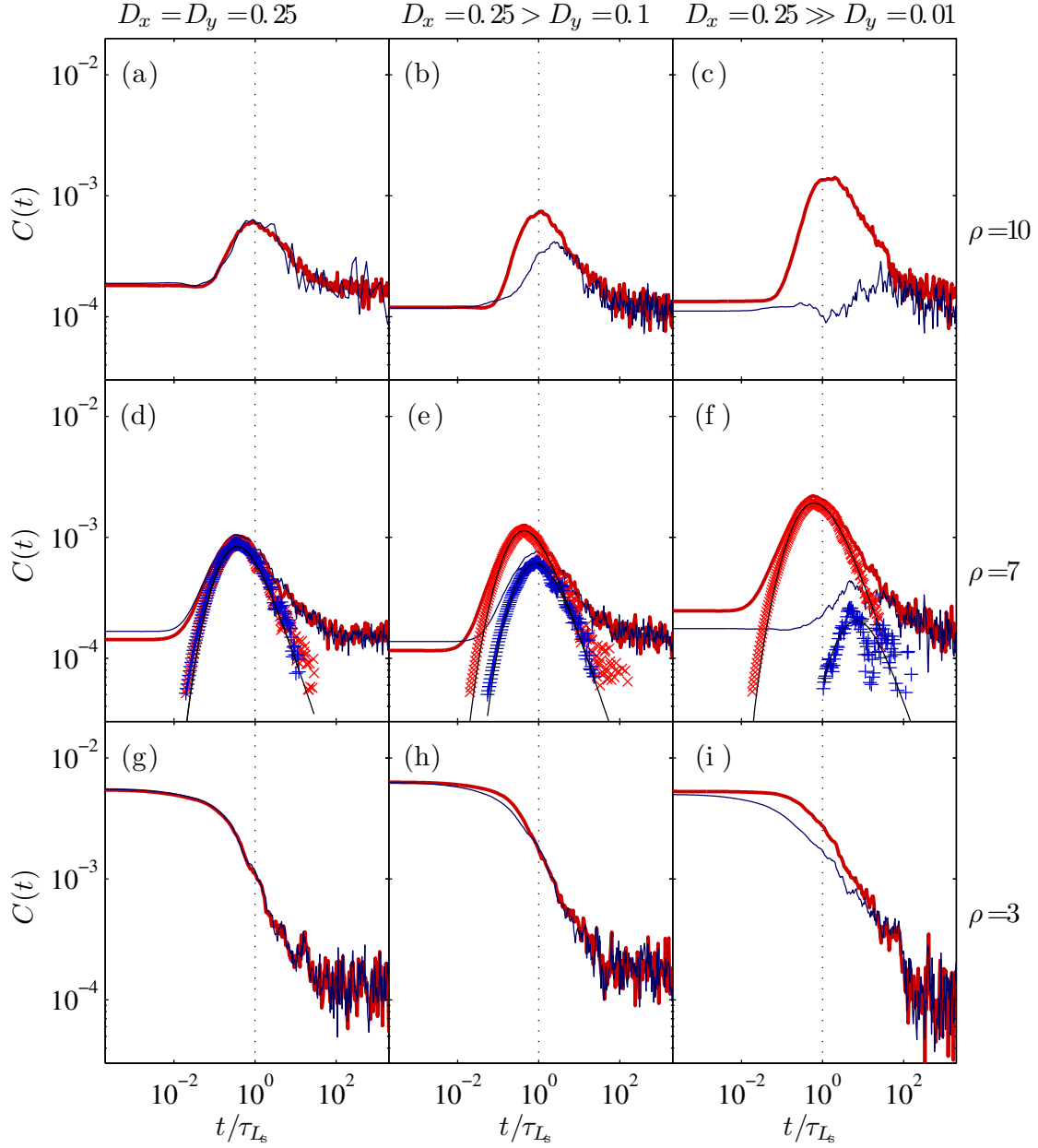
Figure 6.4: Overview of the CCFs [bold (red) lines: $\gamma \parallel x$, thin (blue) lines: $\gamma \parallel y$] of $D_x = D_y$ (left column, Conf. A00), $D_x = 2.5D_y$ (middle column, Conf. A01) and $D_x = 25.0D_y$ (right column, Conf. A02). As well as probe distances of $\rho = 3 < r_{\text{max}}$ (bottom row), $\rho = 7 \gtrapprox r_{\text{max}}$ (middle row) and $\rho = 10 \gg r_{\text{max}}$ (top row). For $\rho \gg r_{\text{max}}$ peaks decrease in height an shift towards the strongly noise affected time regime, thus hindering evaluation. For $\rho < r_{\text{max}}$ the CCFs of different directions differ only marginally and the distinctive peaks are not visible. A distance of $\rho = 7$ (graphs in the center) allows fitting of the CCF, ideally after subtracting C_{offset} (symbols) to obtain a more distinct curve (black lines).

In practice, the peak's shift into the time regime $t \gg \tau_{L_s}$ already is problematic, because more then one particle might contribute to the cross correlation here, which is not accounted for in the theory. Furthermore, the longer the investigated time interval in the CCF, the more events have to be recorded to sufficiently reduce the noise. As an example, the CCFs for $D_x = D_y$ at $\rho = 10$, which yield congruent curves for $\gamma = 0$ and $\pi/2$, are based on a measurement of 10^4 events for $\gamma = 0$ and 10^3 events for $\gamma = \pi/2$, see Fig. 6.4 (a). Though the noise is reduced considerably here, 10^4 events are not enough to sufficiently resolve both peaks of the CCF in Fig. 6.4 (c). Since a larger ρ would yield no further information, the recommended probe distance is $\rho \gtrsim r_{\max}$.

Unless the CCFs for different γ are equal and $D_x = D_y$ can be assumed, a simultaneous fitting of D_x and D_y based on Eq. (6.8) is necessary. It is recommended to subtract the offset C_{offset}=CCF(0) from the CCF to obtain a more distinct curve for fitting, see symbols in Fig. 6.4 (d)-(f). A corresponding evaluation of Conf. A00-A02 at a distance of $\rho = 7$ via non-linear least square fits to Eq. (6.8) yields the diffusion coefficients summarized in Tab. 6.2. They reproduce the input values to a quite good agreement, except the $\gamma = \pi/2 (\parallel y)$ measurement for $D_x = 25.0 D_y$ (Conf. A02), which is too noisy for a better evaluation. To improve results, a coupled fitting of the measurements along the main axis is recommended. With these results all corresponding CCFs, exept Conf. A02 at $\gamma = \pi/2$, in Fig. 6.4 (d)-(f) can be well described as indicated by the solid black lines.

	Conf. A00		Conf. A01		Conf. A02	
	D_x	D_y	D_x	D_y	D_x	D_y
D_{in}	0.25	0.25	0.25	0.10	0.25	0.010
$\gamma \parallel x$	0.28 ± 0.01	0.28 ± 0.01	0.30 ± 0.01	0.06 ± 0.01	0.28 ± 0.01	0.012 ± 0.001
$\gamma \parallel y$	0.28 ± 0.01	0.28 ± 0.01	0.28 ± 0.01	0.11 ± 0.01	0.11 ± 0.01	0.013 ± 0.001

Table 6.2: Anisotropic diffusion coefficients from evaluating the CCFs at $\rho = 7$ in Fig. 6.4.

So far, a system was assumed, where the principal axis of the diffusion tensor are parallel to the x- and y-axes as well as the objects edges. If this is not the case, Eq. (6.8) would have to be evaluated respectively, i.e., by expressing diffusion propagator [Eq. (A.27)] and limits of the detection area in the coordinate system defined by the diffusion tensor. In order to identify the main axis of the diffusion tensor, one can use the fact that the differences in the CCFs are supposed to be the strongest between those γ, which coincide with these axes. The CCFs obtained at different γ listed in Fig. 6.5 confirm this assumption and simultaneously present an approach to identify the axes, even without fitting. After probing several $\gamma \in [0, \pi]$ and marking the peak positions, the γ belonging to the left and right most peaks define the main axes of the system.
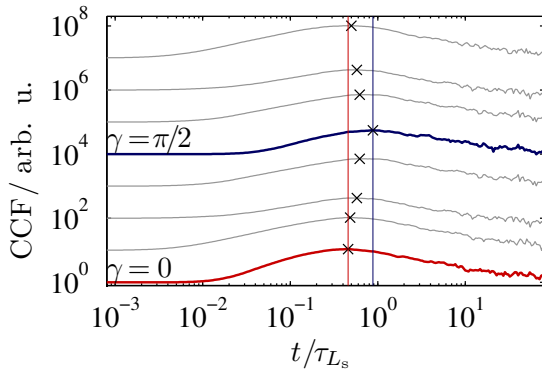

Figure 6.5: Shift of the peak in the CCF for $D_x = 2.5 D_y$ (Conf. A01) depending on the probed direction $\gamma \in [0, \pi[$, in steps of $\Delta\gamma = \pi/8$. Peak positions are marked by $\times$. The CCFs containing the right and leftmost peaks (bold lines) were recorded in direction of the principle axes.

Circularly rotating probe

At first glance it is not possible to implement the method presented in this chapter in practice, because of the short distance allowed between the two probes that have to record a unique signal each. State of the art STM techniques realize a minimal probe distance between 200 nm [79] and 1 mm [80], which is far beyond the requested distance of about 1 nm representing a typical molecule size, see Fig. 1.1. However, letting a single probe rotate with a frequency of ω_{circ} on a circular trajectory of radius ρ provides a convenient workaround. Each point on the circle will repeatedly be passed by the probe in a period of $\Delta t \equiv 2\pi/\omega_{\mathrm{circ}}$. Assuming, that the probe is "blind" except at times $t = (\gamma + 2\pi n)/\omega_{\mathrm{circ}}$ with $n \in \mathbb{N}$ a discrete virtual signal in a given point $\mathrm{P_A} = (\rho, \gamma)$ on the circle can be extracted from the continuous signal of the probe. The time resolution of the virtual signal is defined by Δt and the typical time for an object to traverse from one measurement point to the other by $(2\rho)^2/D$. Hence, $\Delta t \ll (2\rho)^2/D$ should be ensured to sufficiently identify objects diffusing from one measurement point to the other. Because of the circular geometry, the point $\mathrm{P_B} = (\rho, \pi + \gamma)$ is the obvious choice for the second measurement point probing the γ direction.

The convenience of this approach is, that signals corresponding to an arbitrary amount of points on the circle can be extracted simultaneously from a single measurement with the oscillating probe. This is a strong advantage compared to the extended linear probe, which requires an individual measurement for each probed direction. A practical example for the extraction of 4 individual signals at $\gamma = 0, \pi/2, \pi$ and $3\pi/2$ from the continuous signal of an oscillating probe is presented in Fig. 6.3 (b) and (c).

6.3   Experimental implementation

Though these methods were not experimentally tested yet, from a technical point of view there seem to be no hindrances for a scanning tunneling microscope. Linear tip trajectories are already widely used for video STM recordings [32]. They could be transformed into circular trajectories by adding an oscillating instead of a linear displacement in the perpendicular direction. Because the signal recorded by a moving probe will also have a finite time resolution rather than being continuous, this will be the limiting factor in an experimental implementation. To give, as an example, an estimation of the time resolution necessary to identify the diffusion coefficients of CuPc on Ag(100) at 200 K, a minimum of $n = 4$ data points per rotation has to be recorded. Assuming the main axes are known and perpendicular this gives

$$\Delta t_{\mathrm{rec}} = \frac{\Delta t}{n} \leq \frac{(2\rho)^2}{nD} \tag{6.10}$$

as minimal time resolution Δt_{rec}. With approximately $2\rho = 15\,\text{Å}$ and $D = 8 \times 10^{-11}\,\mathrm{cm^2/s}$, compare chapter 7, $\Delta t_{\mathrm{rec}} \lesssim 70\,\mathrm{\mu s}$ should be realized. The measurement setup used by Ikonomov $et\ al.$ [39] had a time resolution of $4\,\mathrm{\mu s}$ and other groups succeeded to realize recording frequencies up to 1.6 MHz [32], i.e., time resolutions below $1\,\mathrm{\mu s}$. This would even allow the probing of either further directions or higher temperatures in this example.

Atomic force microscopes have a rather limited time resolution of about $100\,\mathrm{\mu s}$ [81] to minimal $10\,\mathrm{\mu s}$ [36]. Nevertheless, they are an alternative to investigate anisotropic diffusion properties on isolating surfaces.

Chapter 7

Application to experimental data

The presented simulations are fair surrogate data during development of the evaluation methods, because they allow an arbitrary tuning of the parameters. However, the purpose of developing evaluation methods is to apply them to experimental data. The actual measurement method to record a time series does not matter for the presented evaluation methods. Only the premises of a point like and locally fixed probe and that "on" and "off" intervals can be clearly distinguished in the signal must be fulfilled. Considering the implementation of a measurement the challenge for experimentalists is to create a situation, where on the one hand molecules diffuse freely on the surface and do not form clusters. Hence a low coverage is necessary. On the other hand enough molecules have to pass the tip to record the demanded amount of peaks in a reasonable time, cf. chapter 3.4.

In the following the movement of two different shaped molecules on an isotropic Ag(100) surface is investigated. Copperphthalocyanine is a nearly quadratic molecule, see Fig. 1.1 (c), while the perylene derivate PTCDA has a rectangle like shape, see Fig. 1.1 (f). Experimental findings indicate that CuPc [52] and PTCDA [56], as free molecules, lie flat on the surface. The two systems are therefore ideal candidates to apply the presented evaluation methods.

The data, by courtesy of Sokolowski *et al.* [57], used in this chapter was recorded with a locally fixed STM tip. During "off" intervals only the noise afflicted setpoint current will be recorded. Molecules passing the tip will reduce the tunneling gap and thus increase the tunneling current. These intervals of high current are associated with the "on" times. Sokolowski *et al.* succeeded to establish a measurement environment, suitable to record a sufficient amount of peaks, for CuPc on Ag(100) and PTCDA on Ag(100) at a coverage of $\theta_0 = 10\%$ to 15%. They quote, that at this coverage both molecules form islands, which coexist with a two-dimensional gas phase of freely diffusing molecules [39]. This kind of equilibrium has also been observed in other systems [35] and is stable over a comparably long period of time [34]. To record a fluctuating signal the STM tip is placed in the gas phase between two larger islands. Note that the tip should not be placed too close to either of the islands, because in their adjacencies a molecule's motion can be influenced by inhomogeneities in the diffusion profile [82, 83] and edge diffusion [14], amongst others. Though an interaction between the tip and the molecules can not be ruled out, it can be reduced to an negligible minimum by systematically adjusting the tip-surface distance and bias voltage. Further details of the experiment are given in reference [39].

7.1 Processing raw measurement data

Peaks in an experimentally recorded signal have non-uniform shapes, see for example Fig. 7.1 (a). In case of an STM this roughness may be caused by the passing molecules electronic structure or the hopping motion itself. Additionally the signal will most certainly be noise afflicted. However, as a matter of fact, these detailed shapes are irrelevant for the evaluation via RTD and ITD, as long as "on" and "off" states are clearly distinguishable. It was also shown in chapter 3.1, that an ACF calculated with an "on-off" signal is sufficient to determine the diffusion coefficient. As a result, it is convenient to transform the given experimental time series into a rectangular "on-off" signal. Afterward, all presented evaluation methods can be readily applied.

In the following, a detailed explanation of the necessary preprocessing of STM data to separate the noise from the relevant signal will be given. Parts of the processing might be adaptable to other measurement methods as well, but this has to be judged in the individual case.
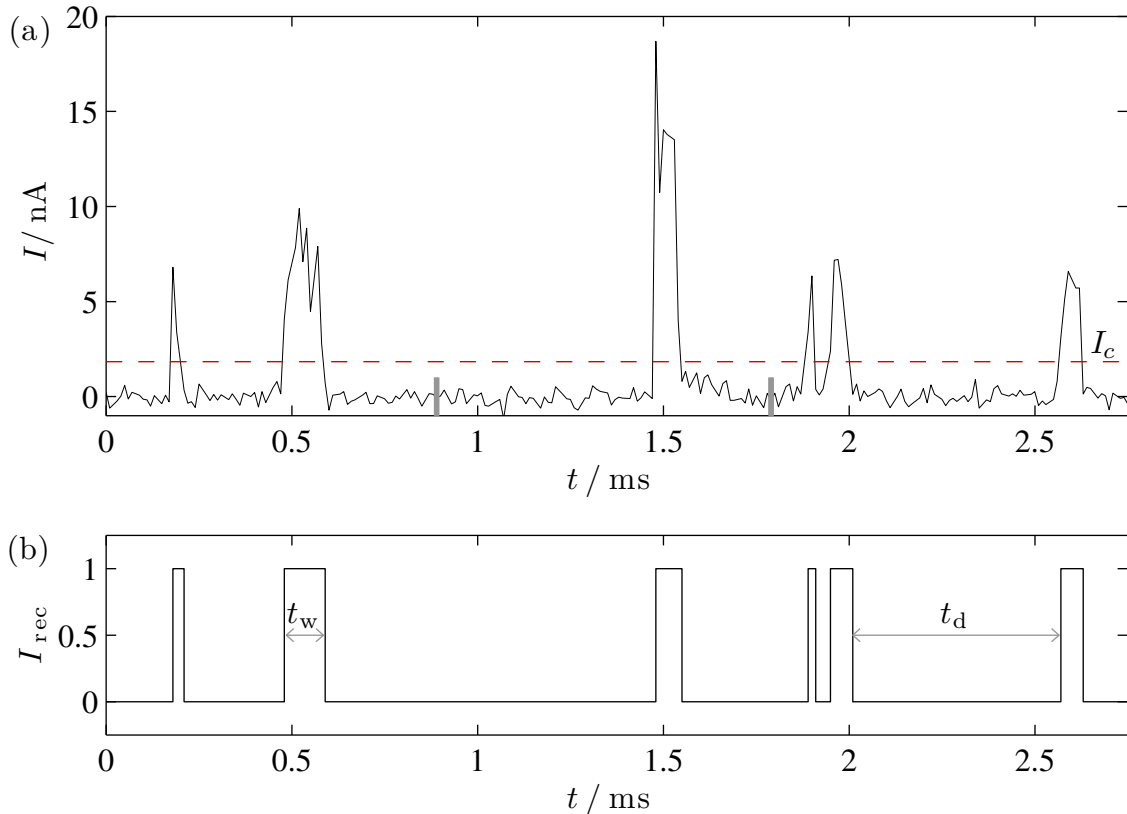
Figure 7.1: (a) Exemplary peaks in a time-current signal, recorded by an STM tip locally fixed above an Ag(100) surface at $T = 166\,\mathrm{K}$. Long interpeak intervals are partially shortened for a better overview (junctions marked by bold ticks). Diffusing CuPc molecules cause peaks that are significantly higher than the noise. The dashed line indicates the threshold I_c, which separates the noise from the relevant signal. It coincides with the lower limit of those current values, that deviate from a Gaussian distribution, c.f. Fig. 7.2 and text. Only those time intervals with currents higher than the threshold are considered as "on" phases in an otherwise "off" signal. (b) The resulting rectangular signal, where only information on the order and duration of "on" (t_w) and "off" (t_d) phases is preserved.

In a histogram of the tunneling currents I at $T = 166\,\mathrm{K}$ in Fig. 7.2 the maximum has been shifted to zero. Previously it can be associated with the tunneling current between the tip and the bare Ag surface, which usually is about $I_0 = 0.3\,\mathrm{pA}$ in the setup of reference [39]. Current values below this maximum can be attributed solely to noise and can be fitted with a half-sided Gaussian. Extending this Gaussian to positive current values yields the solid line in Fig. 7.2. For small positive values it fits the data very well, implying that these values can also be attributed to noise. At higher current values the diffusing molecules cause deviations from the Gaussian. To separate the diffusion-induced fluctuations from the noise, a threshold value I_c is defined, where the Gaussian distribution of the number of occurrences of a noise event drops below one, see dashed line in Fig. 7.2. It amounts to $I_c = 0.18\,\mathrm{nA} > I_0$ in this example. The threshold is then used to separate "on" and "off" states in the signal [dashed line in Fig. 7.1 (a)] and thus transforming it into a rectangular signal [Fig. 7.1 (b)]. An analogous preprocessing at $T = 192\,\mathrm{K}$, yielding a threshold of $I_c = 0.20\,\mathrm{nA}$, is given in the Figures 2 and 3 of reference [†].
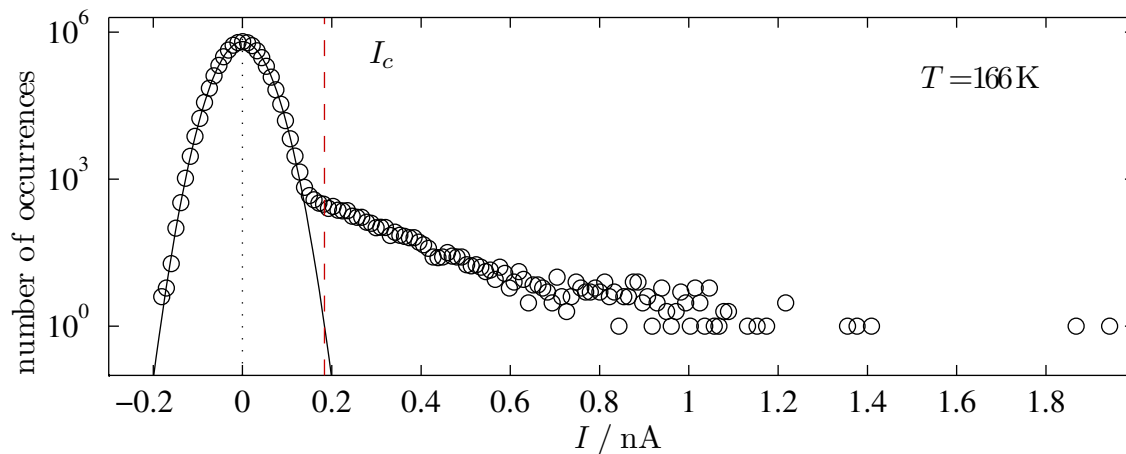
Figure 7.2: Histogram of current values measured at $T = 166\,\mathrm{K}$ after shifting the maximum to zero. The solid line represents a Gaussian fit of the values $I < 0$, which can be attributed to the noise, extended to larger values. The dashed line is positioned where the number of occurrences of noise values drops below one and defines the threshold, which is used to separate the diffusion-induced signal from the noise.

Experimentally recorded signals will usually have a discrete time axis with constant steps Δt [39]. Accordingly, peak widths and interpeak intervals will be multiples of Δt, which can result in a vanishing bin size in the sampling according to reference [73]. A classical histogram with logarithmic scaled bin sizes is therefore better suited for the data on hand and is used in the following.

7.2 Copperphthalocyanine on Ag(100)

The time series of Copperphthalocyanine (CuPc) diffusing on Ag(100), measured at seven different temperatures between $140\,\mathrm{K}$ and $222\,\mathrm{K}$, are available [57]. Hence, the corresponding diffusion coefficients and subsequently the activation energy in this material system can be determined. In the following, out of the seven measurements two, namely $149\,\mathrm{K}$ and $183\,\mathrm{K}$, will be exemplarily treated in detail to determine the diffusion coefficients.

Combined with the diffusion coefficients from other temperatures the Arrhenius equation can be used to determine the activation energy of the material system. Detailed evaluation of $T = 166\,\mathrm{K}$ and $192\,\mathrm{K}$ can be found in reference [†].

For application of the presented methods it is indispensable to know the dimensions of the detection area, i.e. of the molecule. Considering the relaxed vacuum structure from density functional calculations, one will find that CuPc is rather flat, see Fig. 1.1 (c). It has a quadratic footprint with an edge length, including the van der Waals radius of the outer hydrogen atoms of $L_\mathrm{s} = L_\mathrm{l} \approx 14.7\,\text{Å}$, which agrees well with literature values [43]. Observations of free CuPc molecules and other phthalocyanines suggest that their structure is not significantly distorted upon adsorption [39, 43, 52].

The rescaled ACFs $C(t)/C(0)$ of the respective rectangular signals are given by the symbols in Fig. 7.3 (a). Only times $t \leq \tau_{L_\mathrm{s}}/4$ were considered for fitting of the ACF to ensure that the cross-correlation terms can be neglected. This condition is checked self-consistently throughout the fitting process. Non-linear least square fits with the ACF for rectangular objects [Eq. (4.1)] are marked by the solid lines and yield diffusion coefficients of $D = (2.5 \pm 0.5) \times 10^{-11}\,\mathrm{cm}^2/\mathrm{s}$ at $149\,\mathrm{K}$ and $D = (7.8 \pm 0.5) \times 10^{-11}\,\mathrm{cm}^2/\mathrm{s}$ at $183\,\mathrm{K}$. These two diffusion coefficients combined with those resulting at the other temperatures in an Arrhenius plot are shown in Fig. 7.3 (b), where a least square fit with $D = D_0 \exp(-E_\mathrm{a}/k_\mathrm{B}T)$ yields an activation energy of $E_\mathrm{a} = 33 \pm 20\,\mathrm{meV}$ and a pre-exponential factor of $D_0 = (5.7 \pm 1.7) \times 10^{-10}\,\mathrm{cm}^2/\mathrm{s}$. Though the footprint of CuPc could also be compared to a circle, an evaluation via ACF in the circular geometry is not carried out, because the evaluation of simulation data in chapter 4.4 already demonstrated, that the results can be misleading.
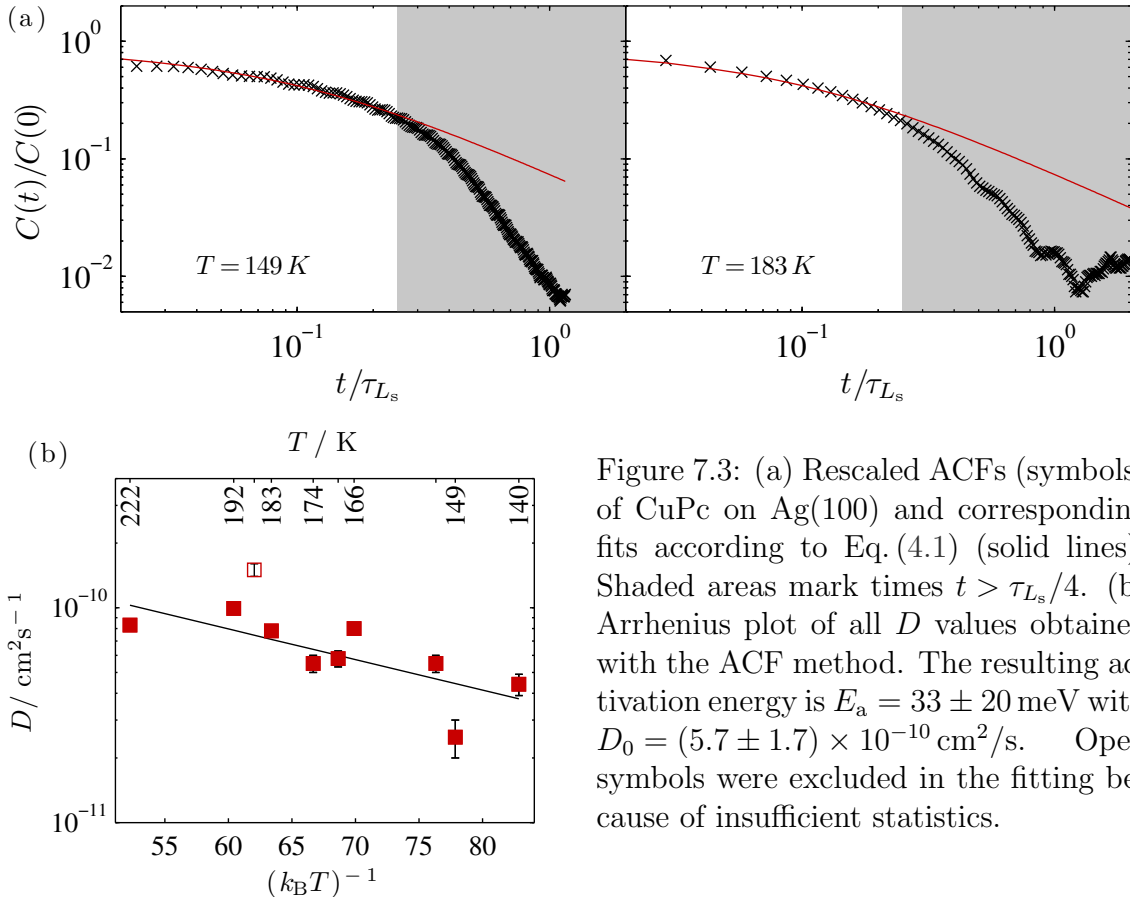
Figure 7.3: (a) Rescaled ACFs (symbols) of CuPc on Ag(100) and corresponding fits according to Eq. (4.1) (solid lines). Shaded areas mark times $t > \tau_{L_\mathrm{s}}/4$. (b) Arrhenius plot of all D values obtained with the ACF method. The resulting activation energy is $E_\mathrm{a} = 33 \pm 20\,\mathrm{meV}$ with $D_0 = (5.7 \pm 1.7) \times 10^{-10}\,\mathrm{cm}^2/\mathrm{s}$. Open symbols were excluded in the fitting because of insufficient statistics.

The residence times are associated with the widths of the rectangular peaks, see t_{w} in Fig. 7.1 (a). Their distribution at temperatures 149 K and 183 K is shown by the symbols in Fig. 7.4. The exponential decays at times $t \geq \tau_{\lambda_{1,1}}$ are fitted with the long time limit of the rectangular RTD solution [Eq. (4.5)]. Here it is also self-consistently checked that the condition $t \geq \tau_{\lambda_{1,1}}$ holds true. As a side note, like discussed in chapter 4 for an quadratic shape it is irrelevant, if the rectangular solution is used or the circular one with an appropriate circle of radius $\tilde{R}' \approx 6.8\,\text{Å}$, following Eq. (4.7). The resulting diffusion coefficients are $D = (5.3 \pm 1.8) \times 10^{-11}\,\text{cm}^2/\text{s}$ for 149 K and $D = (4.6 \pm 0.8) \times 10^{-11}\,\text{cm}^2/\text{s}$ for 183 K. Using this diffusion coefficient an average minimal penetration depth of $\Delta \approx 2.2\,\text{Å}$ is obtained, which is of order of the lattice constant $2.9\,\text{Å}$ [39] of the Ag(100) substrate. As previously discussed this sets a lower limit τ_{Δ} to the applicability of the presented theory, but since $\tau_{\lambda_{1,1}} > \tau_{\Delta}$ it does not affect the fitting. Using these values, the full solution for the RTD [Eq. (4.4)] satisfactorily describes the distribution for times $t \leq \tau_{L_{\mathrm{s}}}/4$. Fig. 7.4 (b) shows an Arrhenius plot of all determined diffusion coefficients. Fitting yields an activation energy of $E_{\mathrm{a}} = 33 \pm 21\,\text{meV}$ and a pre-exponential factor of $D_0 = (5.7 \pm 1.8) \times 10^{-10}\,\text{cm}^2/\text{s}$, which agrees with the results from the ACF analysis.
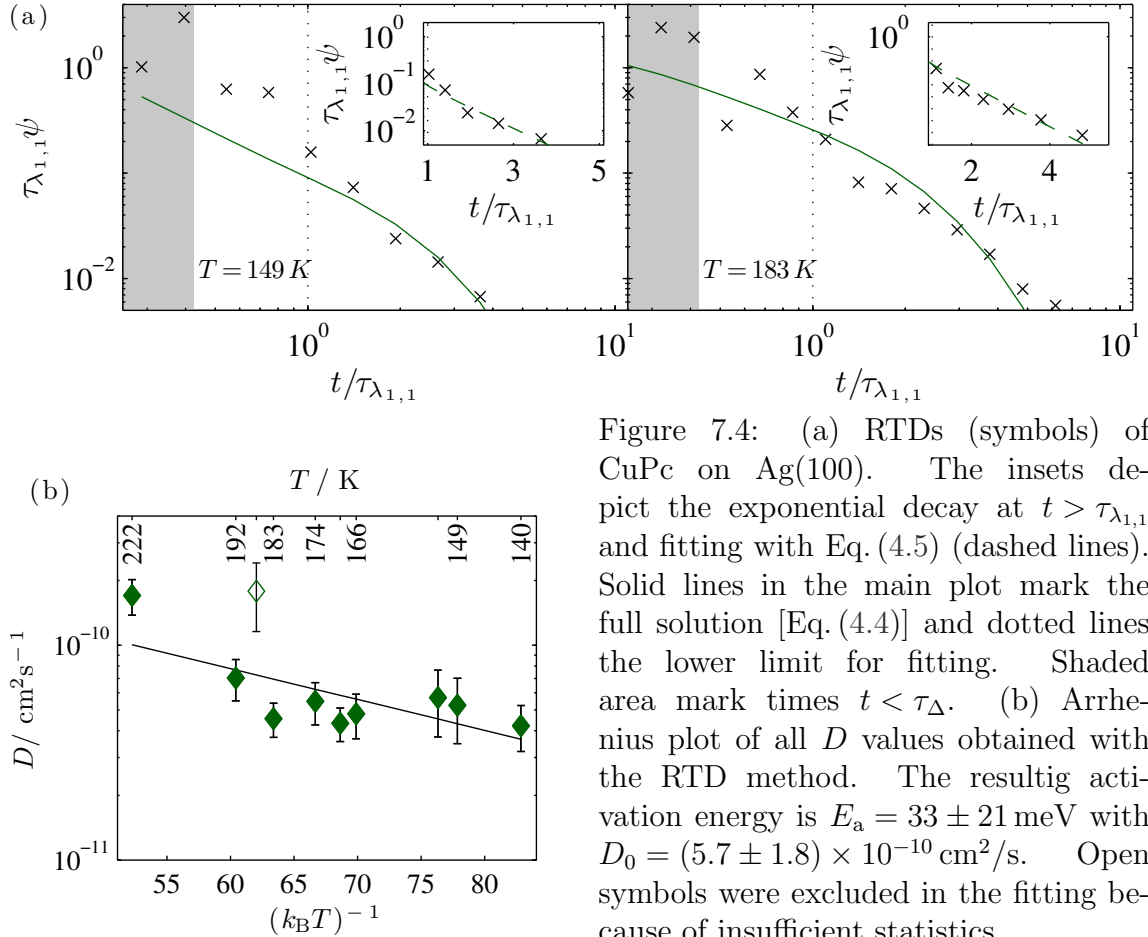
Figure 7.4: (a) RTDs (symbols) of CuPc on Ag(100). The insets depict the exponential decay at $t > \tau_{\lambda_{1,1}}$ and fitting with Eq. (4.5) (dashed lines). Solid lines in the main plot mark the full solution [Eq. (4.4)] and dotted lines the lower limit for fitting. Shaded area mark times $t < \tau_{\Delta}$. (b) Arrhenius plot of all D values obtained with the RTD method. The resultig activation energy is $E_{\mathrm{a}} = 33 \pm 21\,\text{meV}$ with $D_0 = (5.7 \pm 1.8) \times 10^{-10}\,\text{cm}^2/\text{s}$. Open symbols were excluded in the fitting because of insufficient statistics.

Distributing the intervals between two rectangular peaks, e.g. t_{d} in Fig. 7.1, yields the ITD, displayed by symbols in Fig. 7.5 (a) for $T = 149\,\text{K}$ and $183\,\text{K}$. As discussed in chapter 4, there are two possibilities to tackle the evaluation of an ITD. Fortunately, the statistics in the available data sets is good enough, to execute and compare a fitting in the single-particle regime and in the exchange process regime. For evaluating the short

time regime, which is dominated by the same particle returning to the detection area, a circle with $\tilde{R}' \approx 8.3\,\text{Å}$ according to Eq. (4.8) is set as the detection area. The maximum of the distribution and its behavior right to the maximum is fitted as described in chapter 3.3 using $\tau_{\max} = \Delta^2/(6D)$ and Eq. (3.17). The determined diffusion coefficients are $D = (11.4 \pm 3.2) \times 10^{-11}\,\text{cm}^2/\text{s}$ for $T = 149\,\text{K}$ and $D = (10.8 \pm 1.9) \times 10^{-11}\,\text{cm}^2/\text{s}$ for $183\,\text{K}$. The distributions according to Eq. (3.13) with the resulting parameters are marked by the solid lines in Fig. 7.5 (a). The activation energy resulting from all diffusion coefficients determined with the ITD method is $E_{\text{a}} = 32 \pm 20\,\text{meV}$ with $D_0 = (8.3 \pm 2.3) \times 10^{-10}\,\text{cm}^2/\text{s}$. The minimal penetration depth, on average $\Delta = 5.7\,\text{Å}$, is larger in case of the ITD method than the RTD method, but is still comparable to the Ag(100) lattice constant. A possible explanation in terms of penetration depth is that the molecule has to enter the detection area only slightly for turning the signal "on" (RTD). In contrast a quite large distance to the tip is necessary to be disregarded and thus turning the signal "off" (ITD). However, because of the rather strong noise in the short time regime of the ITD, these findings should not be overinterpreted.
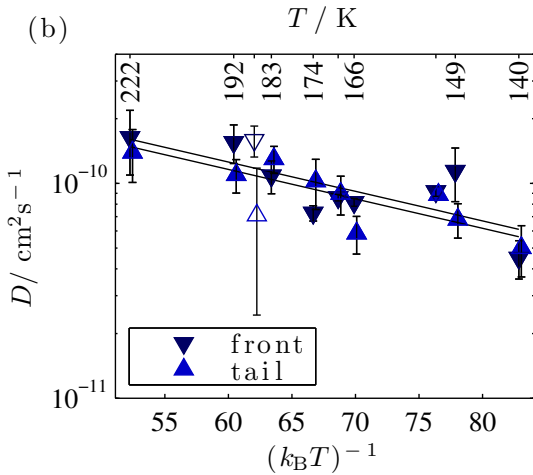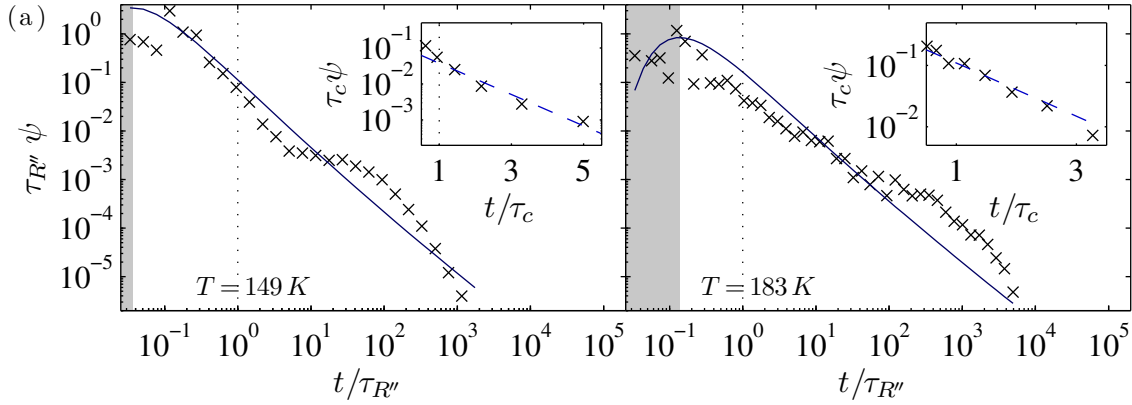
Figure 7.5: (a) ITDs (symbols) of CuPc on Ag(100). Solid lines in the main plots show fitting of the short time regime $t < \tau_{R'}$ with Eq. (3.13). Dashed lines in the insets display fitting of the exponential decay with Eq. (3.16) in the exchange process time regime $t > \tau_c$. Shaded areas mark times $t < \tau_{\max}$. (b) Arrhenius plot of all D values obtained with the ITD method. The resulting activation energy is $E_{\text{a}} = 32 \pm 20\,\text{meV}$ with $D_0 = (8.3 \pm 2.3) \times 10^{-10}\,\text{cm}^2/\text{s}$ for evaluating $t < \tau_{R'}$ and $E_{\text{a}} = 32 \pm 17\,\text{meV}$ with $D_0 = (7.7 \pm 1.5) \times 10^{-10}\,\text{cm}^2/\text{s}$ for $t > \tau_c$. Open symbols were excluded in the fitting because of poor statistics.

To investigate the long time limit, which is dominated by exchange processes of different molecules, first the effective coverage θ in the gas phase has to be determined. It is equivalent to the sum of peak widths compared to the overall measurement time

$\theta \equiv \sum_i t_{w,i}/(t_{w,i} + t_{d,i})$. In the presented data series the effective coverage varies roughly between $\theta = 0.01\%$ and 0.1%. The number density then follows from $c = \theta/\tilde{A}$ [Eq. (2.3)]. In accordance with the findings during the evaluation of simulation data the proportionality factor in Eq. (3.16) is chosen as $\kappa = 1$. Using these parameters the slope of the exponential decay according to Eq. (3.16) yields $D = (6.8 \pm 1.2) \times 10^{-11} \, \mathrm{cm^2/s}$ for $T = 149 \, \mathrm{K}$ and $D = (13.0 \pm 1.9) \times 10^{-11} \, \mathrm{cm^2/s}$ for $183 \, \mathrm{K}$, which is in good agreement with the evaluation of the short time regime and the results of the other methods. Here Δ can not be determined, because the detection area is considered as point-like in this time regime. An Arrhenius plot of all diffusion coefficients obtained via this ITD method is shown in Fig. 7.5 (c). It yields an activation energy of $E_a = 32 \pm 17 \, \mathrm{meV}$ and a pre-exponential factor of $D_0 = (7.7 \pm 1.5) \times 10^{-10} \, \mathrm{cm^2/s}$, which matches the previous results.

The comparison of all three evaluation methods in Fig. 7.6 and Tab. 7.1 shows that an activation energy $\overline{E_a} = 33 \, \mathrm{meV}$ can independently and reliably be obtained with each method. The high relative uncertainty $\overline{\Delta E_a}$ $(\overline{\Delta E_a}/\overline{E_a} \approx 61\%)$ is not surprising for an evaluation of only seven temperatures. The pre-exponential factor D_0 of the different methods varies only by $\pm 20\%$ referring to the average $\overline{D_0} = 7.8 \times 10^{-10} \, \mathrm{cm^2/s}$ indicating, that also the absolute D values are trustworthy. With a total between 300 and 1000 recorded events, see Fig. B.5 in the appendix, the data sets do not contain the minimum of 10000 events as recommended in chapter 3.4. However, at first glance on the autocorrelation function and distributions, see Fig. 7.3, Fig. 7.4 and Fig. 7.5, it becomes obvious that they behave as expected. This implies that even partially weak statistics allow an assessment, albeit the short time regimes of the RTD and ITD are quite noisy. One exception is the signal recorded at $T = 187$ K, where only 46 peaks can be identified, which is too little for a meaningful interpretation and hence this temperature is only treated under reservations and not considered in the determination of the activation energy.
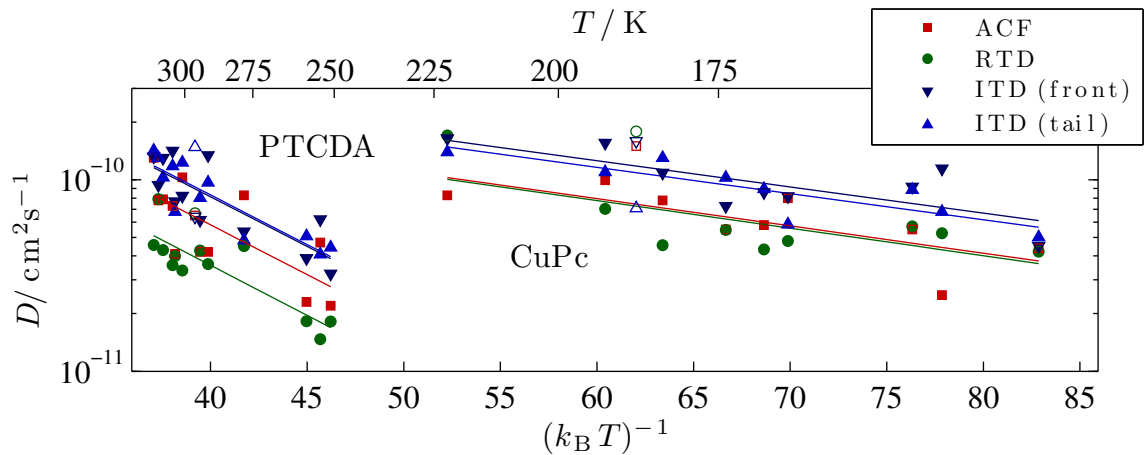

Figure 7.6: An overview of all D values determined for CuPc and PTCDA diffusing on Ag(100) at different temperatures. The activation energy, proportional to the slope of the linear regression, is reliably obtained, independent of the applied evaluation method. The preexponential factor D_0 varies a little, but is still a good basis for calculating absolute diffusion coefficients.

7.3 PTCDA on Ag(100)

For the rectangle like shaped PTCDA molecule diffusing on an Ag(100) surface time series for overall 13 different temperatures between $T = 251\,\mathrm{K}$ and $313\,\mathrm{K}$ are available [57]. Again two data sets, at $T = 254\,\mathrm{K}$ and $304\,\mathrm{K}$, are chosen to be evaluated in detail, while the others serve to determine the activation energy with an Arrhenius plot. By means of density functional theory the longer edge of the relaxed vacuum structure of a PTCDA molecule is found to be $14.6\,\text{Å}$ and the shorter one $8.9\,\text{Å}$, including the van der Waals radii of the hydrogen and oxygen atoms respectively. This size agrees with values, that can be found in the literature [39, 84]. Pertinent sources also suggest that the structure of a free PTCDA molecule is not distorted and stays flat upon adsorption on a surface [39, 56].

The symbols in Fig. 7.7 (a) mark the rescaled autocorrelation functions $C(t)/C(0)$ of the signals at $T = 254\,\mathrm{K}$ and $304\,\mathrm{K}$. A least square fit with the rectangular ACF [Eq. (4.1)], again considering only $t \le \tau_{L_\mathrm{s}}/4$, yields the solid lines and diffusion coefficients of $D = (4.7 \pm 0.5) \times 10^{-11}\,\mathrm{cm^2/s}$ at $254\,\mathrm{K}$ and $D = (4.1 \pm 0.5) \times 10^{-11}\,\mathrm{cm^2/s}$ at $304\,\mathrm{K}$. The activation energy resulting from a linear fit of all diffusion coefficients found for PTCDA in an Arrhenius representation [Fig. 7.7 (b)] is $E_\mathrm{a} = 120 \pm 50\,\mathrm{meV}$ with a preexponential factor of $D_0 = (7.0 \pm 2.8) \times 10^{-9}\,\mathrm{cm^2/s}$.
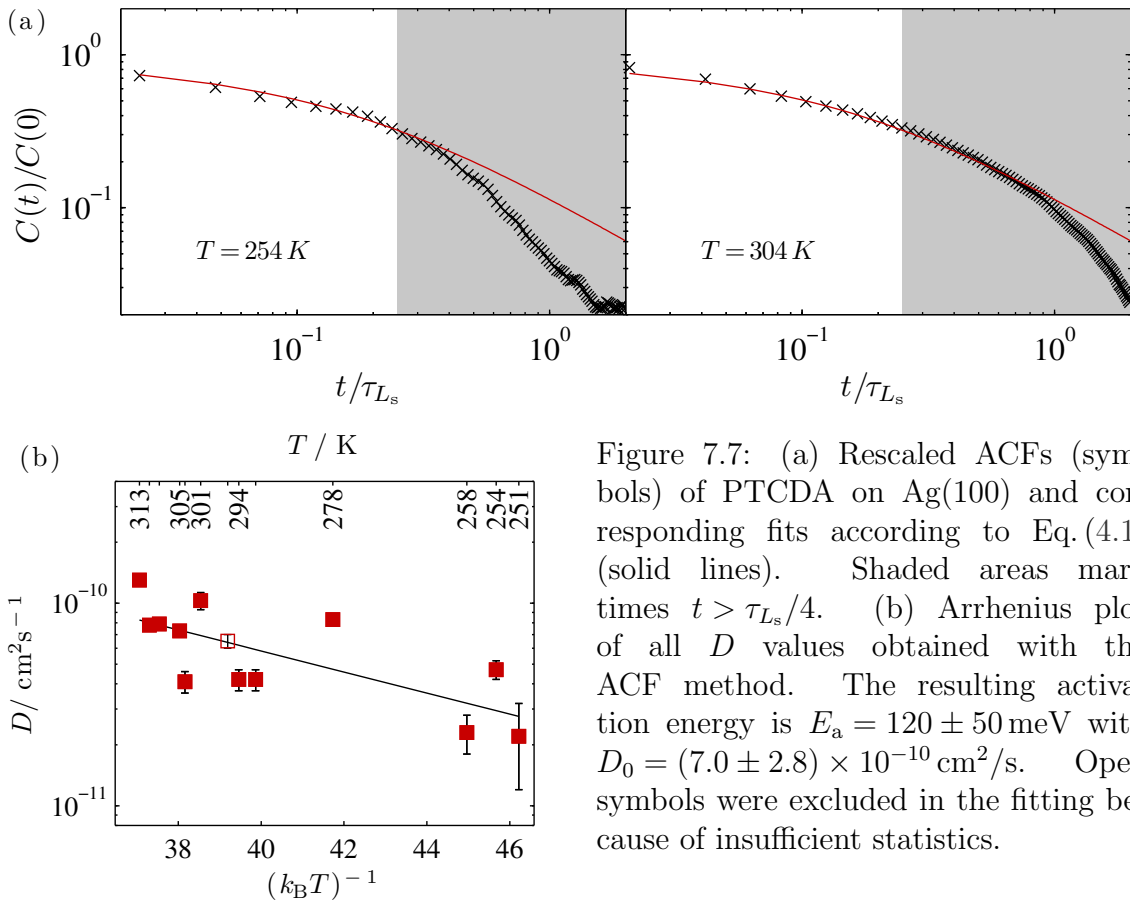
Figure 7.7: (a) Rescaled ACFs (symbols) of PTCDA on Ag(100) and corresponding fits according to Eq. (4.1) (solid lines). Shaded areas mark times $t > \tau_{L_\mathrm{s}}/4$. (b) Arrhenius plot of all D values obtained with the ACF method. The resulting activation energy is $E_\mathrm{a} = 120 \pm 50\,\mathrm{meV}$ with $D_0 = (7.0 \pm 2.8) \times 10^{-10}\,\mathrm{cm^2/s}$. Open symbols were excluded in the fitting because of insufficient statistics.

A distribution of the peak widths contained in the PTCDA signal at $254\,\mathrm{K}$ and $304\,\mathrm{K}$ is displayed by the symbols in Fig. 7.8 (a). The slopes of the exponential tails at $t \ge \tau_{\lambda_{1,1}}$ give diffusion coefficients of $D = (5.3 \pm 1.8) \times 10^{-11}\,\mathrm{cm^2/s}$ at $254\,\mathrm{K}$ and $D = (7.0 \pm 1.5) \times 10^{-11}\,\mathrm{cm^2/s}$ at $304\,\mathrm{K}$ according to the rectangular RTD solution Eq. (4.5).

The lower limit $t \geq \tau_{\lambda_{1,1}}$ for this time regime is checked self-consistently throughout the process. Due to the similarities between circular and rectangular approach a circle with radius $\tilde{R}' = 5.8\,\text{Å}$ can be assigned to the detection area of the PTCDA molecule, following chapter 4.4 with Eq. (4.7). This approach will yield identical values for the diffusion coefficients and minimal penetration depth. The latter is found to be $\overline{\Delta} = 1.9\,\text{Å}$ on average, which is in agreement with the lattice constant $2.9\,\text{Å}$ of the Ag(100) surface and sets a lower time limit τ_Δ that does not interfer with the fitting process. Using these parameters Eq. (4.4) satisfactorily accounts for the whole distribution. Evaluation of an Arrhenius plot [Fig. 7.8 (b)] of all diffusion coefficients yields an activation energy of $E_\text{a} = 120 \pm 44\,\text{meV}$ and a preexponential factor of $D_0 = (4.5 \pm 1.1) \times 10^{-9}\,\text{cm}^2/\text{s}$ in agreement with the result of the ACF method.
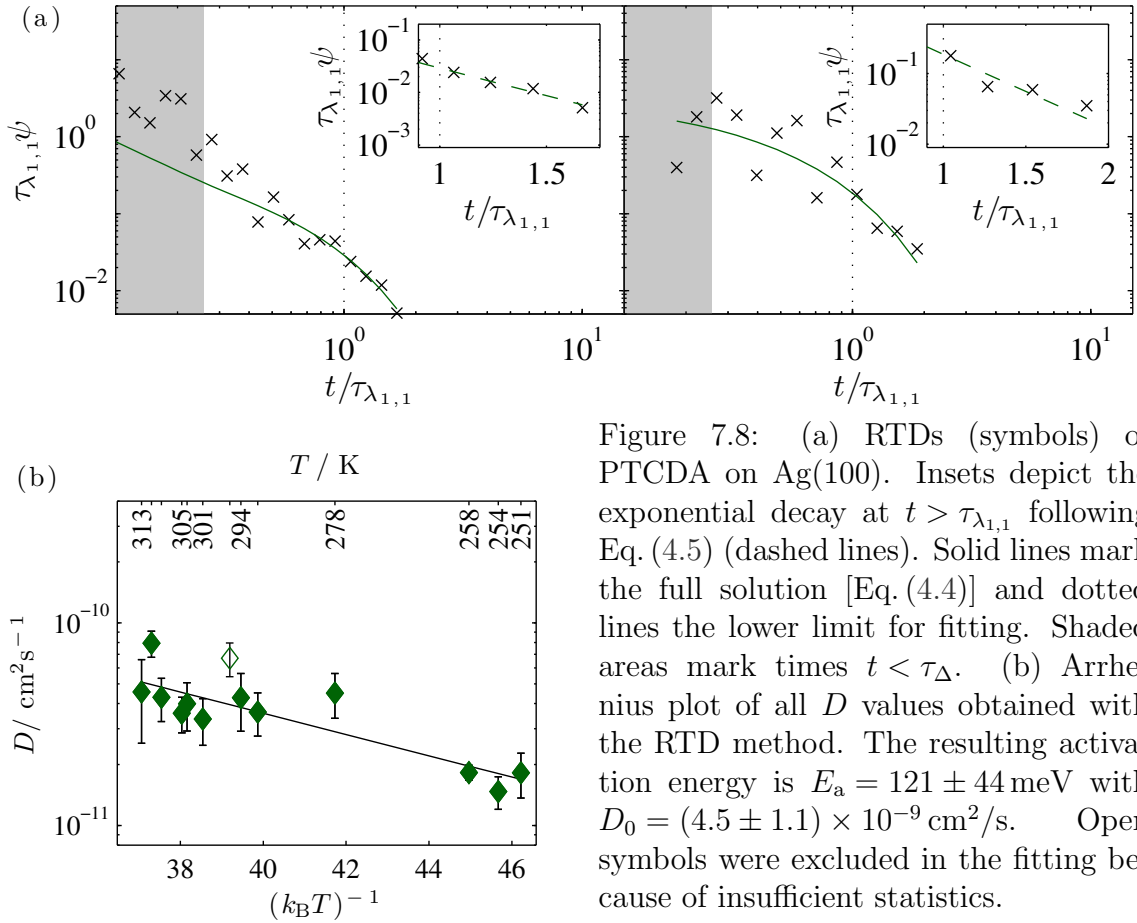
Figure 7.8: (a) RTDs (symbols) of PTCDA on Ag(100). Insets depict the exponential decay at $t > \tau_{\lambda_{1,1}}$ following Eq. (4.5) (dashed lines). Solid lines mark the full solution [Eq. (4.4)] and dotted lines the lower limit for fitting. Shaded areas mark times $t < \tau_\Delta$. (b) Arrhenius plot of all D values obtained with the RTD method. The resulting activation energy is $E_\text{a} = 121 \pm 44\,\text{meV}$ with $D_0 = (4.5 \pm 1.1) \times 10^{-9}\,\text{cm}^2/\text{s}$. Open symbols were excluded in the fitting because of insufficient statistics.

The interpeak time distribution of PTCDA diffusing on Ag(100) at $T = 254\,\text{K}$ and $304\,\text{K}$ is shown by the symbols in Fig. 7.9(a). The effective coverage of the surface in the vicinity of the recording tip determined from the time series ranges between $\theta = 0.04\%$ and 4%. Transformed into the number density it can be used to determine the diffusion coefficient from the slope of the exponential decay in the exchange process regime for $t \gg \tau_c$ given in Eq. (3.16). With $\kappa = 1$, the results are $D = (6.3 \pm 1.9) \times 10^{-11}\,\text{cm}^2/\text{s}$ at $T = 254\,\text{K}$ and $D = (7.7 \pm 1.2) \times 10^{-11}\,\text{cm}^2/\text{s}$ at $T = 304\,\text{K}$. The activation energy is $E_\text{a} = 120 \pm 41\,\text{meV}$ in case of the ITD evaluation with an preexponential factor of $D_0 = (9.9 \pm 2.1) \times 10^{-9}\,\text{cm}^2/\text{s}$. These values agree well with the previous findings.

Lacking an exact solution for the short time regime of the ITD with a rectangular detection area, the circular solution Eq. (3.14) with an effective radius of $\tilde{R}' = 6.4\,\text{Å}$ according to Eq. (4.8) is used for an assessment in the time regime $t \ll \tau_{L_s}$. The latter condition is dynamically adjusted during the process. With this approach diffusion coefficients of $D = (4.1 \pm 0.8) \times 10^{-11}\,\text{cm}^2/\text{s}$ at $254\,\text{K}$ and $D = (6.8 \pm 0.9) \times 10^{-11}\,\text{cm}^2/\text{s}$ at $304\,\text{K}$, as well as an average mininmal penetration depth of $\overline{\Delta} = 5.3\,\text{Å}$ are obtained. Note that the short time regime is again quite noisy. The overall results including an activation energy of $E_a = 120 \pm 48\,\text{meV}$ and the preexponential factor of $D_0 = (9.7 \pm 2.9) \times 10^{-9}\,\text{cm}^2/\text{s}$ are in good agreement with the previous findings.
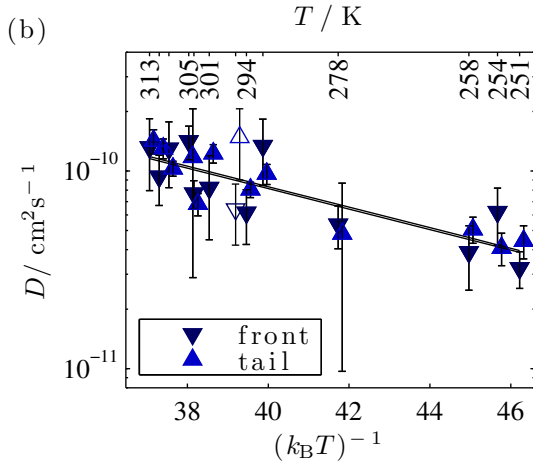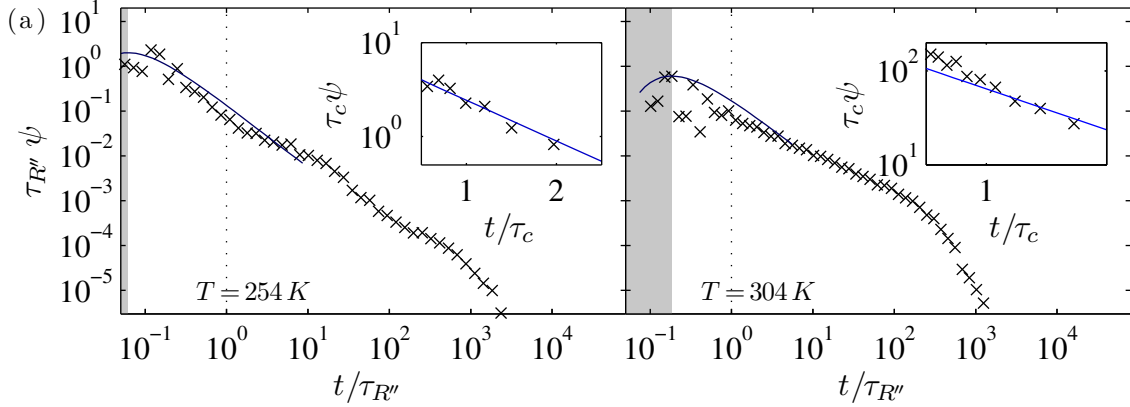
Figure 7.9: (a) ITDs (symbols) of PTCDA on Ag(100). Solid lines in the main plots show fitting of the short time regime $t < \tau_{R''}$ with Eq. (3.13). Dashed lines in the insets display fitting of the exponential decay with Eq. (3.16) in the exchange process time regime $t > \tau_c$. Shaded areas mark times $t < \tau_{\max}$. (b) Arrhenius plot of all D values obtained with the ITD method. The resulting activation energy is $E_a = 120 \pm 48\,\text{meV}$ with $D_0 = (9.7 \pm 2.9) \times 10^{-9}\,\text{cm}^2/\text{s}$ for evaluating $t < \tau_{R''}$ and $E_a = 120 \pm 41\,\text{meV}$ with $D_0 = (9.9 \pm 2.1) \times 10^{-9}\,\text{cm}^2/\text{s}$ for $t > \tau_c$. Open symbols were excluded in the fitting because of poor statistics.

Again it was demonstrated, that all three methods can be used independently to determine the activation energy of about $\overline{E_a} = 120\,\text{meV}$, see Fig. 7.6 and Tab. 7.1. The relative error of $\overline{\Delta E_a}/\overline{E_a} = 38\%$ is smaller than for CuPc, because 13 instead of 7 temperatures are available. The variation in the preexponential factor of over $\pm 30\%$ referring to the average $\overline{D_0} = 7.8 \times 10^{-9}\,\text{cm}^2/\text{s}$ is larger than for the evaluation of CuPc. The RTD values differ the strongest, which is caused by the small $\tilde{R}/a$ ratio as explained in the discussion (Chapter 7.4).

The RTDs of PTCDA are the most noise afflicted distribution in this context. This is surprising because in case of PTCDA more events have been recorded per time series than

for CuPc. All time series have recorded about 10^3 and more peaks. Several offer even more than the recommended minimum of 10^4 events, see Fig. B.5 in the appendix. An exception is the measurement at T=296 K, where only 135 events were reported and which is therefore treated under reservations and not included when determining the activation energy. Consideration of the mean residence times , see Fig. B.6 in the appendix, offers a possible explanation to this apparent contradiction. In a certain temperature range, the typical residence times are shorter for the smaller PTCDA molecule than for CuPc and therefore a higher experimental time resolution is necessary to resolve the short peaks sufficiently. However, the time resolution is limited and thus the error when resolving the shortest peaks of diffusing PTCDA in the respective temperature range is higher than for CuPc. Furthermore, the experimental equipment is operated close to the maximal possible recording frequency [85]. The higher noise in case of the PTCDA therefore seems to be caused by experimental limitations.

The reader might also notice the comparably large differences in the diffusion coefficients between adjacent temperatures, e.g. $T = 301$ K to 305 K. As a matter of fact, these measurements have not been performed subsequently, but over a long period of time interrupted by other measurements, see Tab. B.1 in the appendix. The results matching each other straightaway is therefore rather a sign of the experimental method's robustness and reproducibility.

	CuPc			
	$D(149\,\mathrm{K})/10^{-11}\mathrm{cm}^2/\mathrm{s}$	$D(183\,\mathrm{K})/10^{-11}\mathrm{cm}^2/\mathrm{s}$	$D_0/10^{-9}\mathrm{cm}^2/\mathrm{s}$	$E_\mathrm{a}/\mathrm{meV}$
ACF	2.5 ± 0.5	7.8 ± 0.5	5.7 ± 1.7	33 ± 20
RTD	5.3 ± 1.8	4.6 ± 0.8	5.7 ± 1.8	33 ± 21
ITD (front)	11.4 ± 3.2	10.8 ± 1.9	8.3 ± 2.3	32 ± 20
ITD (tail)	6.8 ± 1.2	13.0 ± 1.9	7.7 ± 1.5	32 ± 17
	PTCDA			
	$D(254\,\mathrm{K})/10^{-11}\mathrm{cm}^2/\mathrm{s}$	$D(304\,\mathrm{K})/10^{-11}\mathrm{cm}^2/\mathrm{s}$	$D_0/10^{-10}\mathrm{cm}^2/\mathrm{s}$	$E_\mathrm{a}/\mathrm{meV}$
ACF	4.7 ± 0.5	4.1 ± 0.5	7.0 ± 2.8	120 ± 50
RTD	5.3 ± 1.8	7.0 ± 1.5	4.5 ± 1.1	121 ± 44
ITD (front)	4.1 ± 0.8	6.8 ± 0.9	9.7 ± 2.9	120 ± 48
ITD (tail)	6.3 ± 1.9	7.7 ± 1.2	9.9 ± 2.1	120 ± 41

Table 7.1: Overview of translational diffusion coefficients, pre-exponential factors and the respective activation energies determined from STM signal fluctuation caused by CuPc and PTCDA diffusing on Ag(100).

7.4 Discussion of the results

Throughout applying the methods to simulation data in chapters 3 and 4 premises have been stated to assure a meaningful evaluation. These will be revised in the following with respect to the experimental data. A minimum number of recorded events was suggested in chapter 3.4, because it was anticipated that other sources of disturbance, would affect the distribution of residence times and interpeak intervals, as well as the autocorrelation function in an experiment. Though this recommendation still holds true, the data on hand shows that even much less events are sufficient for an evaluation, if the experiment is conducted with care.

It was also discussed, that a molecule size of $\tilde{R}/a \geq 3$ sets a lower limit to the applicability of the continuum theory underlying the expressions Eqs. (3.9), (3.13) and (4.4). CuPc with $R' = \tilde{R}'/a \approx 8.0/2.9 \approx 2.8$ ($R''\tilde{R}''/a \approx 8.2/2.9 \approx 2.8$) and PTCDA with $R' = \tilde{R}'/a \approx 5.8/2.9 = 2.0$ ($R'' = \tilde{R}''/a \approx 6.4/2.9 \approx 2.2$) on Ag(100) both, albeit within a justifiable distance, fall below this boundary. Therefore, is has to be clear in one's mind, that the absolute values of D tend to be underestimated in case of the RTD method, compare Fig. 3.8 (c). For $R' = 2$ (PTCDA) they are presumably off by 35% and, indeed, D_0 values obtained from PTCDA diffusing on Ag(100) with the RTD method differ by 40% from the average value, whereas they blend in with the other values for diffusing CuPc. Evaluation of the short time regime in the ITD is also, though not as strongly, affected by this difficulty and leads to slightly overestimated values, see Fig. 3.8 (c). As a result, D_0 values obtained with this ITD method tend to be the largest, compare Fig. 7.6 and Tab. 7.1.

Another aspect entering the treatment of experimental data is the time resolution of the signal. While handling simulation data, the time resolution was, if at all, limited by the machine accuracy. Real hardware, however, is limited in its capacity and records the signal in discrete time steps. All three methods presented here require a certain recording frequency. For using the RTD method only the exponential decay at $t \geq \tau_R$ or $t \geq \tau_{\lambda_{1,1}}$ is necessary for evaluation. Hence, peaks with corresponding widths have to be resolved in detail. The ITD method at first glance seems to be even less demanding, because it allows an analysis of the long time limit for times $t > \tau_c$ with $\tau_c > \tau_R$ at typical coverages. However, to determine the interpeak intervals the peaks separating them have to be identified as well and therefore the ITD and RTD method are comparable in their required time resolution. Most problematic in this context is the ACF method, which calls small time shifts of $t \ll \tau_R$ or $t \ll \tau_{L_s}$ in the correlation to exclude the influence of cross-correlations. The available time series has a time resolution of 4 μs generally fulfilling all of these demands for the given materials. But, as already addressed in chapter 7.3, it might lead to uncertainties for very short peaks and thus noisy short time regimes in RTD and ITD. Compared to related methods, however, the STM is best suited for this type of measurement and should usually comply with the requirements, because of its high recording frequency of 100 kHz [86] and beyond. Evaluation of AFM signals, for instance, can be more challenging, because the recording frequency commonly is ten times smaller [87].

If one of the molecules diffuses anisotropically on the Ag(100) surface cannot be answered conclusively by these recordings of a fixed point like tip, as has been pointed out in chapter 6. Rotational diffusion, however, should be identifiable, albeit only for the rectangular shaped PTCDA. CuPc is nearly quadratic and rotational diffusion would therefore cause no deviation from the ACF and distributions known for pure translational movement, compare chapter 5.4. The short time regime of the ITD of PTCDA at $T = 313$ K indeed deviates from the curve predicted for purely translational diffusion, see Fig. 7.10 (c), which could be interpreted as additional shoulder indicating rotational diffusion. Also the ACF, Fig. 7.10 (a), is not as smooth as expected in this case. Opposing these hints on rotational diffusion of the PTCDA molecule, there is strong evidence against it. The alteration in the ACF has a rather polygonal shape and does not resemble the kink caused by rotational diffusion described in chapter 5.1. Furthermore, rotational diffusion of the PTCDA molecule on a surface, besides rotating $\pm\pi/2$ from time to time in order to form a closed layer [42], was not mentioned in the literature, so far. The fact disagreeing most with the assumption of rotational diffusion is the curve of the RTD,

which behaves just as expected for translational diffusion, even though is it supposed to be the most sensitive for identification of these two types of motion, compare chapter 5.4. Since the peculiarities only appear for the methods including the molecule's motion outside of the detection area, the explanation is reduced to some obstacle on its path that hindered free translational diffusion, like nucleation on surface defects and with other diffusing molecules [88] or capture by a neighboring island [14]. Since it was the last in a series of measurements, see Tab. B.1 in the appendix, and no signs of rotational diffusion could be found for the other temperatures, it is likely that the STM tip either drifted into a non-favorable area of the surface during the continuous heating or the surface itself deformed due to stress.
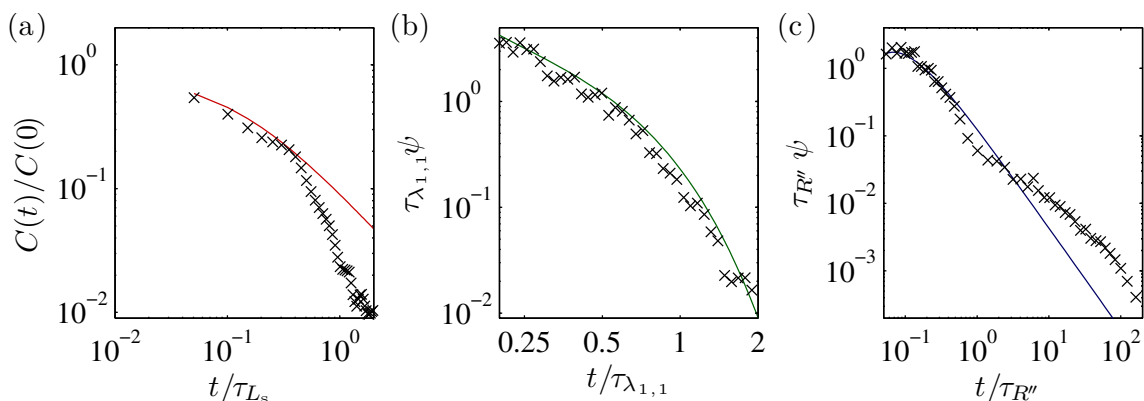
Figure 7.10: (a) ACF, (b) RTD and (c) ITD of PTCDA diffusing on Ag(100) at $313\,\mathrm{K}$ (symbols). ACF and ITD deviate slightly from the curves expected for translational diffusion only [Eq. (4.1) and Eq. (3.13)], the RTD on the contrary meets the predictions [Eq. (4.4)] (solid lines). Parameters correspond to the evaluation in chapter 7.3.

The evaluation of PTCDA and CuPc diffusing on Ag(100) with the RTD method was previously reported in reference [39] and the treatment of CuPc by means of the ACF, ITD and RTD methods was presented in reference [†]. The partially deviating results will be addressed in the following. The higher activation energy for CuPc on Ag(100) in reference [39], was already explained in reference [†], naming a strong weighting of the exposed data point for $T = 222\,\mathrm{K}$ as the reason for the difference. This weighting by the error in D during determination of the activation energy also explains the discrepancy in E_a of PTCDA on Ag(100). In this work the the errors were not considered in the linear regression for the activation energy, because they all are of comparable size for a given method.

The small deviations in D_0 are caused by different definitions of the molecule size. In reference [†] a circular detection area was assigned to the CuPc molecule with its gyration radius. This is legitimate for a nearly circular molecule like CuPc, but with the recent knowledge on how rectangular molecules should be treated, compare chapter 4.4 and reference [‡], R' from Eq. (4.7) has to be chosen as the appropriate radius. In reference [39] the rectangular solution was used, but slightly different edge lengths were assigned to the rectangular footprint of the molecules. Without own measurements it is hard to say which one is correct here, because of the different values available in literature, e.g. for the van der Waals radius of hydrogen between $1.1\,\text{Å}$ and $1.2\,\text{Å}$ [89], and the fact that the molecule might adjust itself a little to the surface. Anyway, the error due to this minimal differences in the detection area's dimension should be negligible.

7.5   Comparison of the methods

Of the presented methods each has its strengths and weaknesses. These will be filed in the following to find the optimal evaluation method for a given measurement. The list contains topics specific for STM measurements, which possibly do not apply to other measurement methods. Those can yet entail their own problems.

All three methods have in common that they require a rectangular "on"-"off" signal, which is extracted from a continuous signal by setting a threshold current. Afterward, peak widths and interpeak intervals can be identified simultaneously. Note that any method of determining a threshold is associated with some uncertainty. For the ITD, this is no problem in practice, because the the interpeak intervals are large compared to the peak widths. For the RTD, the vagueness of the threshold is a more severe problem. Because molecules diffuse slowly into the detection area, the peaks in the original tunneling current signal have rather flat flanks. As a result, the peak widths change more sensitively with the threshold than the interpeak intervals, compare Fig. B.7 in the appendix.

An advantage of the RTD is that the diffusion coefficient can be determined solely by analyzing the exponential tail for large residence times. One should note, however, that it may be challenging to obtain a good statistics in this time regime, if the molecules are highly mobile or small. In this case, the peaks are narrow and it could be difficult to resolve them accurately. Another problem is that the RTD can give misleading absolute values of the diffusion coefficient, when the radius assigned to the detection area is smaller than three times the jump size of the molecule on the substrate. The determination of the activation energy is not affected by this problem. In the RTD method, the interaction with the STM tip can influence the residence times and in this case one would not determine the free diffusion of the molecules on the substrate. By systematically changing the bias voltage, a possible influence can, however, be reduced to a minimum [39]. A strength of the RTD, which should not be underestimated, is that it is related to a single-particle problem and no approximations enter the treatment.

The ITD method has the advantage, that tip-molecule interaction can be expected to have, if at all, a marginal influence on the interpeak times. However, it is prone to be disturbed on its path outside the detection area, e.g. by surface defects. For small interpeak intervals, the ITD is essentially also related to to a single-particle problem, with the same restrictions for the molecules size as the RTD. Furthermore, an exact solution in this time regime is only available for circular shaped molecules. For large interpeak intervals, the diffusion coefficient can be determined based on an estimate for exchange processes, where one molecule after leaving the detection area is followed by a different molecule entering it.

The autocorrelation function of a rectangular signal can be readily calculated by a fast Fourier transformation. If only a table of toggling times between "on" and "off" should be available, it can be calculated as described in appendix B.1, with only minor setbacks in calculation time. Furthermore, it is unlike the RTD and ITD method immune to the problem of exceeding a certain molecule size compared to the jump length to be applicable. A disadvantage is that only the short time regime is governed by single-particle diffusion, while an accurate theoretical description of the crossover to the long-time regime, governed by the collective particle diffusion, requires a careful consideration of the mutual exclusion of the molecules (and possibly other interaction effects). Another drawback is that the determination of the ACF includes time intervals, where molecules are under the tip, and possible interactions with the tip can thus have an influence on the diffusion properties.

The crucial strengths and weaknesses of the methods are summarized in Tab. 7.2 to quickly find an evaluation method suited for a given data set.

Characteristics	ACF	RTD	ITD
Signal processing	⊕ Convenient by FFT	⊖ Peak widths affected by I_c	⊕ Negligible influence of I_c on interpeak intervals
Tip influence	⊖ Possible	⊖ Possible	⊕ Less likely
Assumptions in theory	⊖ Non-interacting particles	⊕ None	⊕ Short time regime: None ⊖ Long time regime: Non-interacting particles
Minimal size	⊕ None	⊖ $R \geq 3$	⊖ $R \geq 3$
Simultaneous determination of D_φ	⊖ Not possible	⊕ Possible	⊕ Possible

Table 7.2: Strengths and weaknesses of the three methods for determining D

Chapter 8

Closing remarks, summary and outlook

In this work various methods are developed to characterize diffusive motion of molecules on surfaces by analyzing fluctuations in the signal of a locally fixed point-like probe. The methods enable the determination of absolute translational as well as rotational diffusion coefficients of molecules taking into account their shape. In case of anisotropic diffusion the diffusion tensor and its principal axes can be identified. The recording of time series stands out amongst other measurement techniques: It has a high time resolution, since the tip does not have to move in order to scan a certain area. It is universally applicable and hardly limited in the investigated materials. And it is minimally invasive, because it neither damages the sample nor does it significantly influence the adsorbate's motion.

The evaluation methods are based on the autocorrelation function (ACF) of the recorded signal, the distribution of peak widths (residence time distribution - RTD) and the distribution of interpeak intervals (interpeak time distribution - ITD). Each of them contains at least one characteristic time regime, which allows determination of the diffusion coefficient. In the short time regimes of the ACF and ITD a non-linear fitting procedure is applied. The long time regimes of the RTD and ITD are evaluated with a linear regression, due to their exponential decay. Each of these three methods has its own strengths and weaknesses and the appropriate evaluation method depends on the situation. For instance the RTD is simple in evaluation, but requires a very good time resolution to sufficiently resolve short peaks. Therefore, the long time regime of the ITD might be a better choice in case of high mobilities. This way, the methods, which all operate on the same recorded signal, complement each other.

Summary

In chapter 2 and 4 of this work, respective formulas are given for the ACF, RTD and ITD, which was newly developed in this work, to extract translational diffusion coefficients of circular adsorbates. To include rectangular adsorbates in the considerations corresponding adjustments to the theory are made. Though the functional behavior in general does not differ from the solutions regarding circular adsorbates, it is found that the adsorbate's shape has to be correctly specified in order to obtain non-misleading diffusion coefficients. Here, kinetic Monte Carlo simulation data, as described in chapter 2, were used to test the methods and suggest prerequisites for experimental measurements like a minimum number of recorded peaks.

The evaluation methods are successfully applied to experimental data recorded with a locally fixed STM tip [57] in chapter 7 of this work. With each evaluation method individually it is possible to determine consistent translational diffusion coefficients of copperphthalocyanine and PTCDA diffusing on Ag(100) over a wide temperature range.

Rectangular adsorbates cause further variations in the signal, if they perform rotational moves in addition to the translational displacements. To include rotational degrees of freedom in the theoretical treatment, the case of uncoupled translational and rotational diffusion is considered in chapter 5. If the rate of translational and rotational movements is comparable or rotation is dominant, the RTD and ITD separate into two time regimes, where one is governed by rotation and the other by translation. Based on a novel theoretical description of the rotational behavior in the rotation dominated time regime absolute values for rotational diffusion coefficients can be determined. Simultaneously, the translation governed time regime can be used for determination of translational diffusion coefficient with the previously described methods.

In chapter 6 further means are developed to quantify anisotropic diffusion on the surface. Along with the development of these methods new experimental setups for corresponding measurements are suggested. Since directional information of the motion is required, a point like probe is no longer sufficient. To resolve this problem the RTD of a linearly extended probe and the cross correlation of signals recorded at two separated measurement points are introduced. For these two setups theoretical descriptions were derived, which allow the determination of the diffusion tensor and its principal axis as was tested on kinetic Monte Carlo simulation data of a corresponding measurement setup. From a practical point of view, the cross-correlation technique turns out as more flexible. It is, however, difficult to implement, because the probing sites have to be very close. For use in an experiment, hence, a continuously recording point-like probe rotating on a circular path is suggested. Simulations with tips moving accordingly and subsequent coarse graining of the recorded signal verified that arbitrary individual measurement points on the circle can be emulated this way. Since such experiments were not executed yet, the experimental practicability is discussed.

Outlook

The various methods developed in this work are not limited to adsorbates diffusing on a surface on the atomic scale. In principle, the only requirements for their applicability are that the recording probe has to be small compared to the investigated object and that is has to distinguish between "on" and "off" states. Therefore, with an appropriate sensor also other large diffusing objects should be amenable to the general treatment, as, for instance, graphene flakes [90] or compactly diffusing adatom clusters [14]. Also, the evaluation methods should be applicable to molecules diffusing inside a two-dimensional membrane [91]. The principles of ACF and RTD are, with modifications, transferable to three-dimensions. Noteworthy in this context is the single-molecule fluorescence spectroscopy [92, 93, 94, 95], which is also based on fluctuations in the recorded signal. Because of the larger focal volume, the rotation can probably not be resolved here, but the principles for investigating anisotropic motion, may be adjustable to quantify anisotropic diffusion in liquid environments.

For application of the presented evaluation methods the detailed shape of the measured signal may be irrelevant. However, the peak shape certainly contains further information on probe-sample interactions. Sumetskii *et al.* [38, 75] pursued an approach to determine

the autocorrelation function of an STM tip locally fixed above a surface, which contained detailed information on the adatoms as well as the tunneling geometry. This idea could be picked up for analogous considerations with molecules. These have elaborate electronic structures and motion patterns, that might be elucidated this way. Furthermore the STM tip could be functionalized with either different surface materials or with single molecules to probe their interaction with the diffusing adsorbates.

So far, some of the evaluation methods were applied exclusively to simulation data. This calls for experimentalists to record corresponding time series, e.g. for circular-shaped or rotating rectangular molecules. The novel approach of letting tips move on circular trajectory, while continuously recording the signal, as suggested to simulate close individual measurement points, is a challenging task. For applicability of the corresponding evaluation method, it is crucial to verify, if the necessary coarse graining is possible for noise affected signals. The convenient characterization of several diffusion properties by evaluation of a single time series recorded with available measurement hardware should encourage the effort.

Appendix A

Details on derivations

The first part of the appendix contains selected derivations of formulas, that would have hindered the flow of reading in the main text.

A.1   Autocorrelation function

Given a locally fixed probe site on a two-dimensional surface of size A and N objects with lateral extent $\tilde{A}$ diffusing on this surface, the autocorrelation function is generally defined by the following relation

$$C(t) = \langle S(0) S(t) \rangle . \tag{A.1}$$

The overall signal S is given as the sum of the contributions $s_\mu(t) \equiv s_\mu[\mathbf{r}_\mu(t)]$ of each object to the signal $S(t) = \sum_{\mu=1}^{N} s_\mu(t)$. This allows the decomposition

$$C(t) = \left\langle \sum_{\mu=1}^{N} s_\mu(0) \sum_{\mu=1}^{N} s_\mu(t) \right\rangle = \sum_{\mu=1}^{N} \langle s_\mu(0) s_\mu(t) \rangle + \sum_{\mu=1}^{N} \sum_{\substack{\nu=1 \\ \nu \neq \mu}}^{N-1} \langle s_\mu(0) s_\nu(t) \rangle . \tag{A.2}$$

Assuming independent objects the latter expectaion values seperates into $\sum_{\mu \neq \nu} \langle s_\mu \rangle \langle s_\nu \rangle$. Furthermore, the objects are supposed to be indistinguishable, so the sums break down to

$$C(t) = N \langle s(0) s(t) \rangle + N(N-1) \langle s \rangle^2 . \tag{A.3}$$

In the evaluation of measurement data only times smaller than τ_R will be considered, where τ_R is the typical time for the object to cross the probe site completely. This way it can be assured, that the same object is considered in the vicinity of the probe site during this time. Under these circumstances the term containing the cross-correlation between two different objects becomes small compared to the dominant self correlator and Eq. (A.3) reads

$$C(t) = N \langle s(0) s(t) \rangle . \tag{A.4}$$

For the cross-correlation term a rough treatment can be given by considering the expectation value $\tilde{A}/A$ of a single object's rectangular signal. In this case the cross-correlation term amounts to add $(c\tilde{A})^2$, where $c = N/A$ is the number density of objects on the surface, to Eq. (3.3).

The remaining self-correlator $\langle s(0) s(t) \rangle$ in Eq. (A.4) can be calculated from the probability for an object at position $\mathbf{r}_1$ at time t to contribute to the signal, if it was previously

giving a signal in position $\mathbf{r}_0$ at time $t = 0$:

$$\langle s(0)\, s(t) \rangle = A^{-1} \int \mathrm{d}\mathbf{r}_0 \int \mathrm{d}\mathbf{r}_1 s(\mathbf{r}_1) p(\mathbf{r}_1, t | \mathbf{r}_0) s(\mathbf{r}_0). \tag{A.5}$$

The probability to relocate from $\mathbf{r}_1$ to $\mathbf{r}_0$ in time t is given by the two-dimensional diffusion propagator [18]

$$p(\mathbf{r}_1, t | \mathbf{r}_0) = \frac{1}{4\pi Dt} \exp\left(-\frac{(\mathbf{r}_1 - \mathbf{r}_0)^2}{4Dt} \right). \tag{A.6}$$

Combination of Eqs. (A.4)-(A.6), yields the autocorrelation function in Eq. (3.3).

A.2 Modified autocorrelation function including rotational diffusion

When including rotational diffusion changing the object's orientation φ in the consideration of the autocorrelation function, as described in chapter 5.1, the general expression [Eq. (3.3)] is expanded to

$$C(t) = c \int_0^{2\pi} \mathrm{d}\varphi_1 \tag{A.7}$$

$$\int_{-\frac{L_1}{2}}^{\frac{L_1}{2}} \mathrm{d}x_0 \int_{-\frac{L_s}{2}}^{\frac{L_s}{2}} \mathrm{d}y_0 \int_{-\frac{L_1}{2}}^{\frac{L_1}{2}} \mathrm{d}X_1 \int_{-\frac{L_s}{2}}^{\frac{L_s}{2}} \mathrm{d}Y_1 \ p\left(x_1(X_1, Y_1), y_1(X_1, Y_1), \varphi_1, t | x_0, y_0, \varphi_0\right).$$

Since the translation and rotation are supposed to be uncoupled in this model, the diffusion propagator

$$p(x_1, y_1, \varphi_1, t | x_0, y_0, \varphi_0) = \frac{\exp\left(-\frac{(x_1 - x_0)^2 + (y_1 - y_0)^2}{4Dt} \right)}{4\pi Dt} \frac{\exp\left(-\frac{\varphi^2}{4D_\varphi t} \right)}{\sqrt{4\pi D_\varphi t}} \tag{A.8}$$

is simply the product of the free solutions of the two-dimensional translational diffusion equation $\partial p / \partial t = D\Delta p$ and the diffusion equation for one-dimensional azimuthal rotational diffusion $\partial p / \partial t = D \partial^2 p / \partial \varphi^2$. The consideration of the angular displacement between initial and target orientation calls for an additional integration in φ. The angular difference is, without loss of generality, given in reference to the starting orientation resulting in a prefactor of 2π. Also, each of the target orientations is equally probable, but only one will be taken, which calls for a normalization by $1/2\pi$ canceling out the other prefactor. The coordinate transformation

$$\mathbf{r_1} = \begin{pmatrix} x_1 \\ y_1 \end{pmatrix} = \begin{pmatrix} \frac{X_1}{|X_1|} \sqrt{X_1^2 + Y_1^2} \cos\left[\arctan\left(\frac{Y}{X} \right) + \varphi \right] \\ \frac{X_1}{|X_1|} \sqrt{X_1^2 + Y_1^2} \sin\left[\arctan\left(\frac{Y}{X} \right) + \varphi \right] \end{pmatrix}. \tag{A.9}$$

is necessary to switch between initial and target detection area coordinates.

Eq. (A.7) can not be solved analytically and it can not be simplified, because of the nontrivial φ dependencies. Hence, the full five-fold integral has to be evaluated numerically. This is furhtermore impeded by the oscillatory terms in the integrand, which calls for a careful choice of the supporting points.

A.3 Diffusion propagator for circular absorbing boundaries

The propagator for a circular stripe with absorbing boundaries at r_a and r_c ($r_a < r < r_c$) and initial probability distribution

$$p_0(\mathbf{r}) = p_0(r) = \frac{1}{2\pi r}\delta(r - r_b), \ r_a < r_b < r_c, \tag{A.10}$$

is derived in the following as previously reported in reference [†]. The limit $r_a \to 0$ will yield the RTD propagator and $r_c \to \infty$ the ITD propagator.

In order to do so the symmetry of the circular geometry asks for solving the radial diffusion equation using $p(\mathbf{r}, t) = p(r, t)$

$$\frac{\partial p(r,t)}{\partial t} = D\left(\frac{\partial^2}{\partial r^2} + \frac{1}{r}\frac{\partial}{\partial r}\right)p(r,t)\ . \tag{A.11}$$

With the product ansatz $p(r, t) = f(r)g(t)/2\pi$ equation (A.11) separates into a spatial and a time dependent part. The time dependency yields $g(t) = \exp(-\lambda^2 D t)$, where $\lambda^2 > 0$ are the eigenvalues of the radial Laplace operator

$$\left(\frac{\partial^2}{\partial r^2} + \frac{1}{r}\frac{\partial}{\partial r}\right)f_n(r) = -\lambda_n^2 f_n(r)\ . \tag{A.12}$$

Equation (A.12) is the Bessel differential equation [96], which is solved by both the zeroth-order Bessel functions of first $J_0(.)$ and second kind $Y_0(.)$, so that the eigenfunctions can be given as their linear combination $f_n(r) = A_n J_0(\lambda_n r) + B_n Y_0(\lambda_n r)$. The absorbing boundary requires the spatial function to vanish for all times at the respective radii $f_n(r_a) = f_n(r_c) = 0$, resulting in

$$J_0(\lambda_n r_a) Y_0(\lambda_n r_c) - J_0(\lambda_n r_c) Y_0(\lambda_n r_a) = 0\ , \tag{A.13}$$

as the determination equation for the λ_n, with $n = 1, 2, \ldots$ ($0 < \lambda_1 < \lambda_2 < \ldots$). After defining

$$W(x, y) = J_0(x) Y_0(y) - J_0(y) Y_0(x) \tag{A.14}$$

the solution becomes

$$p(r, t) = \frac{1}{2\pi}\sum_{n=1}^{\infty} C_n W_0(\lambda_n r, \lambda_n r_a) \exp\left(-\lambda_n^2 D t\right)\ , \tag{A.15}$$

with the boundary condition $W_0(\lambda_n r_a, \lambda_n r_c) = 0$. Because the Laplacian is negative definite [97], the eigenvalues λ_n^2 are positive, which guarantees linear independent eigenfunctions [74]. This can be employed via

$$\int_{r_a}^{r_c} \mathrm{d}r\ r W_0(\lambda_m r, \lambda_m r_a) W_0(\lambda_n r, \lambda_n r_a) = \delta_{m,n}\int_{r_a}^{r_c}\mathrm{d}r\ r W_0^2(\lambda_n r, \lambda_n r_a) \tag{A.16}$$

to determine the expansion coefficients C_n from the initial condition in Eq. (A.10)

$$C_n = \frac{\int_{r_a}^{r_c}\mathrm{d}r\ r W_0(\lambda_n r, \lambda_n r_a) p_0(r)}{\int_{r_a}^{r_c}\mathrm{d}r\ r W_0^2(\lambda_n r, \lambda_n r_a)} = \frac{W_0(\lambda_n r_b, \lambda_n r_a)}{\int_{r_a}^{r_c}\mathrm{d}r\ r W_0^2(\lambda_n r, \lambda_n r_a)}\ . \tag{A.17}$$

The result for $p(r,t)$ for the general situation therefore is

$$p(r,t) = \sum_{n=1}^{\infty} \frac{W_0(\lambda_n r_b, \lambda_n r_a) W_0(\lambda_n r, \lambda_n r_a)}{2\pi \int_{r_a}^{r_c} dr \, r W_0^2(\lambda_n r, \lambda_n r_a)} \exp\left(-\lambda_n^2 Dt\right) . \tag{A.18}$$

The specialized propagator in Eq. (3.8) used for the RTD in chapter 3.2 is obtained by letting $r_a \to 0$, which calls for some adjustments on the derivation. First, only one boundary condition $f(r_c) = 0$ has to be taken into account. Second, the Bessel functions of second kind cease to apply, because their logrithmic singularity [74] at the origin eliminates them from the space of functions, where the radial Laplacian is Hermitian. The eigenfunctions thus are given by $f_n(r) = A_n J_0(\lambda_n r)$, where the λ_n are determined by $J_0(\lambda_n r_c) = 0$. Eq. (A.15) becomes

$$p(r,t) = \frac{1}{2\pi} \sum_{n=1}^{\infty} A_n J_0(\lambda_n r) \exp\left(-\lambda_n^2 Dt\right) , \tag{A.19}$$

and the A_n are again determined by the initial condition, corresponding to an expansion of $p_0(r)$ [Eq. (A.10)] into a Fourier-Bessel series

$$A_n = \frac{\int_0^c dr \, r J_0(\lambda_n r) p_0(r)}{\int_0^{r_c} dr \, r J_0^2(\lambda_n r)} = \frac{2 J_0(\lambda_n r_b)}{r_c^2 J_1^2(\lambda_n r_c)} . \tag{A.20}$$

This yields

$$p(r,t) = \frac{1}{\pi r_c^2} \sum_{n=1}^{\infty} \frac{J_0(\lambda_n r) J_0(\lambda_n r_b)}{J_1^2(\lambda_n r_c)} \exp\left(-\lambda_n^2 Dt\right) . \tag{A.21}$$

Eq. (3.8) follows by setting $r_c = R$, $r_b = R - \Delta_R$ and $\lambda_n = \chi_n/R$, where χ_n is the n-th root of the Bessel function of first kind $J_0(.)$.

The limit $r_c \to \infty$ yields the propagator in Eq. (3.12) used for the ITD in chapter 3.3. Again the derivation is slightly different in this case. The spectrum of eigenvalues determined by Eq. (A.13) becomes continuous. Analogous to the change of a Fourier series to a Fourier integral, the Weber transform [98]

$$Q(\lambda) = \frac{1}{r_a^2} \int_{r_a}^{\infty} dr \, r W_0(\lambda r, \lambda r_a) q(r) , \tag{A.22}$$

of a function $q(r)$ along with its back-transformation

$$q(r) = r_a^2 \int_0^{\infty} d\lambda \, \lambda \frac{W_0(\lambda r, \lambda r_a)}{J_0^2(\lambda r_a) + Y_0^2(\lambda r_a)} Q(\lambda) \tag{A.23}$$

can be considered. Accordingly, Eq. (A.15) becomes

$$p(r,t) = \frac{1}{2\pi} \int_0^{\infty} d\lambda C(\lambda) W_0(\lambda r, \lambda r_a) \exp\left(-\lambda^2 Dt\right) , \tag{A.24}$$

where

$$C(\lambda) = \int_{r_a}^{\infty} dr \, r \frac{\lambda W_0(\lambda r, \lambda r_a) p_0(r)}{J_0^2(\lambda r_a) + Y_0^2(\lambda r_a)} = \frac{\lambda W_0(\lambda r_b, \lambda r_a)}{J_0^2(\lambda r_a) + Y_0^2(\lambda r_a)} . \tag{A.25}$$

This yields

$$p(r,t) = \int_0^{\infty} \frac{d\lambda}{2\pi} \lambda \frac{\lambda W_0(\lambda r, \lambda r_a) W_0(\lambda r_b, \lambda r_a)}{J_0^2(\lambda r_a) + Y_0^2(\lambda r_a)} \exp\left(-\lambda^2 Dt\right) . \tag{A.26}$$

Eq. (3.12) follows by setting $r_a = R$, $r_b = R + \Delta_R$ and $\lambda = \chi/R$

A.4 Free translational diffusion propagator with diffusion tensor

The free diffusion propagator for anisotropic diffusion in d dimensions then reads [77]

$$p\left(\mathbf{r}, t | \mathbf{r}', t'\right) = \frac{(2\pi)^{-d/2}}{\sqrt{\left(2\left(t-t'\right)\right)^d \det \underline{\underline{D}}}} \exp\left(-\frac{1}{2}\frac{1}{2\left(t-t'\right)}\left(\mathbf{r}-\mathbf{r}'\right)^{\mathrm{T}} \underline{\underline{D}}^{-1}\left(\mathbf{r}-\mathbf{r}'\right)\right), \quad \text{(A.27)}$$

where $\underline{\underline{D}}$ is the diffusion tensor. In its principal axis system it has the form,

$$\underline{\underline{D}} = \begin{pmatrix} D_x & 0 \\ 0 & D_y \end{pmatrix}, \quad \text{(A.28)}$$

where D_x and D_y are the eigenvalues along the respective direction of this axis system. In a coordinate system aligned to the the principal axis system the propagator becomes

$$p\left(\mathbf{r}, t | \mathbf{r}', 0\right) = \frac{1}{4\pi\sqrt{D_x D_y}t} \exp\left(-\frac{D_y\left(r_1-r_1'\right)^2 + D_x\left(r_2-r_2'\right)^2}{4D_x D_y t}\right), \quad \text{(A.29)}$$

which transitions into Eq. (A.6) for $D_x = D_y$.

A.5 One-dimensional residence time distribution

In case of one-dimensional diffusion the detection area is reduced to a detection line. As a result, obtaining the residence time distribution calls for solving the one-dimensional diffusion equation $\partial p/\partial t = -D\partial^2 p/\partial x^2$ with two absorbing boundaries $p(x=0,t) = p(x=L,t) = 0$ at the beginning and end of the detection line.

$$p\left(x, t\right) = \sum_{n=0}^{\infty} c_n \sin\left(\frac{n\pi x}{L}\right) \exp\left[-D\left(\frac{n\pi}{L}\right)^2 t\right]. \quad \text{(A.30)}$$

The coefficients c_n are defined by the initial distribution, which is, split equally, positioned Δ in front of the absorbing boundaries $p(x,t=0) = 1/2[\delta(x-\Delta) + \delta(x-(L-\Delta))]$

$$c_n = \frac{2}{L}\int_0^L \mathrm{d}x\, p(x,0) \sin\left(\frac{n\pi x}{L}\right) = \frac{1}{L}\left[1-(-1)^n\right] \sin\left(\frac{n\pi\Delta}{L}\right). \quad \text{(A.31)}$$

Only coefficients with odd n ($c_n = 2/L\sin((2n+1)\pi\Delta/L)$) will contribute to the sum. With $\nu = 2n+1$ the diffusion propagator then reads

$$p\left(x, t\right) = \sum_{n=0}^{\infty} \frac{2}{L} \sin\left(\frac{\nu\pi\Delta}{L}\right) \sin\left(\frac{\nu\pi x}{L}\right) \exp\left[-D\left(\frac{\nu\pi}{L}\right)^2 t\right]. \quad \text{(A.32)}$$

Analogously to the two-dimensional considerations, the residence time distribution follows from

$$\psi\left(t\right) = -\partial_t \int_0^L \mathrm{d}x\, p\left(x, t\right) = \sum_{n=0}^{\infty} \frac{4Dq_n^2}{\nu\pi} \sin\left(q_n\Delta\right) \exp\left(-Dq_n^2 t\right) \quad \text{(A.33)}$$

introducing $q_n = \nu\pi/L$.

In case of rotational diffusion $(D \rightarrow D_\varphi)$ the variable x is equivalent to the angular displacement and $\Delta = \Delta_\varphi$ corresponds to the angular distance of the initial distribution to the absorbing boundary. The length of the detection line L equals the maximum angular interval ϕ inside the rectangular detection area depending on the distance r from the rotation center, compare Fig. 5.1(c). Alternatively, $\psi(t)$ also can be expressed in terms of arcs lengths l_r rather than angles by replacing $\phi = l_r/r$, as done in Eq. (5.4) of chapter 5.2.

A.6 Derivation of approximations

Throughout this work time regimes have been identified within the ACF, RTD and ITD in the respective setups. Within these time regimes the functional dependence is usually reduced to an exponential or power law behavior, which allows for a much easier handling. In this chapter some explanation is given, how these time regimes can be derived analytically from the respective full solution.

A.6.1 Autocorrelation function for circular objects

The autocorrelation function for $t \rightarrow 0$ gives the expectation value of the signal, or physically the probability, that the probe site is covered, which is $C(0) = c\tilde{A}$. This relation, however, can also be derived mathematically from the full ACF given in Eq. (3.7). If $t \ll \tau_R$ the argument of the included Bessel function becomes large, therefore the approximation for large arguments $I_0(z) \rightarrow e^z/\sqrt{2\pi z}$ for $|z| \rightarrow \infty$ [74] is legitimate. After some expansions Eq. (3.7) reads

$$
\begin{aligned}
C(t) &\sim \frac{4\pi c}{4Dt} \int_0^R \mathrm{d}r_1\, r_1 \int_0^R \mathrm{d}r_0\, r_0 \frac{\sqrt{4\pi Dt}}{\sqrt{4\pi Dt}}\, e^{-\frac{r_0^2+r_1^2}{4Dt}} \sqrt{\frac{4Dt}{4\pi r_0 r_1}}\, e^{-\frac{2r_0 r_1}{4Dt}} \\
&\sim 2\pi c \int_0^R \mathrm{d}r_1 \sqrt{r_1} \int_0^R \mathrm{d}r_0 \sqrt{r_0} \left[\frac{e^{-\frac{(r_0-r_1)^2}{4Dt}}}{\sqrt{4\pi Dt}} \right].
\end{aligned} \tag{A.34}
$$

The square parenthesis contain a Gaussian distribution, which becomes the Dirac Delta function $\delta(r_0 - r_1)$ for $t \rightarrow 0$. The integral is therefore reduced to $2\pi c \int_0^R \mathrm{d}r_0\, r_0 = c\pi R^2$.

After the substitution $\rho_i = r_i/\sqrt{4Dt}$ with $i = 0,1$ the ACF for circular objects reads

$$
C(t) \propto \int_0^{\rho_{\max}} \mathrm{d}\rho_0 \int_0^{\rho_{\max}} \mathrm{d}\rho_1 \rho_1 \rho_0 \exp\left(-\left(\rho_1^2 + \rho_0^2\right)\right) I_0\left(2\rho_1 \rho_0\right). \tag{A.35}
$$

$\rho_{\max} \equiv R/\sqrt{4Dt} = \sqrt{\tau_R/4t}$ is the upper integral boundary after substitution. For times $t \gg \tau_R$ all $\rho_i \ll 1$. Under these conditions the exponential function ($e^x \sim 1$ for $x \rightarrow 0$) as well as the modified Bessel function ($I_0(z) \sim 1$ for $|z| \rightarrow 0$ [74]) become 1 and the integrals are reduced to $\int_0^{\rho_{\max}} \mathrm{d}\rho_0\, \rho_0 \int_0^{\rho_{\max}} \mathrm{d}\rho_1 \rho_1$ To estimate the general behavior of the function, note that the biggest contribution to the integral for a given ρ_0 is for $\rho_1 = 1$, so that $C(t) \sim \int_0^{\rho_{\max}} \mathrm{d}\rho\, \rho = \rho_{\max}^2/2 = R^2/4Dt$ indicates the power law $\propto t^{-1}$.

A.6.2 Autocorrelation function for rectangular objects

In the limit $t \rightarrow 0$ the ratios $\tau_{L_s}/t < \tau_{L_l}/t$ contained in the full ACF for rectangular objects [Eq. (4.1)] become very large, so the error functions tend to one and $\exp(-\tau_{L_{s,l}}/4t) \rightarrow 0$.

Simplification yields

$$C(t) \sim \frac{c}{\pi} \left[\sqrt{4Dt} + \sqrt{\pi} L_{\mathrm{l}} \right] \left[\sqrt{4Dt} + \sqrt{\pi} L_{\mathrm{s}} \right] \tag{A.36}$$

in this case and $C(0) = cL_{\mathrm{l}}L_{\mathrm{s}}$, which is the expectation value to find the probe site covered.

The power law $\propto t^{-1/2}$ in the intermediate time regime $\tau_{L_{\mathrm{s}}} \ll t \ll \tau_{L_{\mathrm{l}}}$ arises, because the behavior here is regulated by a very small $\tau_{L_{\mathrm{s}}}/t$ and a very large $\tau_{L_{\mathrm{l}}}/t$ ratio. The parentheses in Eq. (4.1) containing the L_{l} dependence are treated like before and for those depending on L_{s} the limiting cases for small arguments z, yielding $\mathrm{erf}(z) \sim 2z/\sqrt{\pi}$ and $\exp(z) \sim 1$, are employed. In this case Eq. (4.1) reads

$$\begin{aligned} C(t) &\sim \frac{c}{\pi} \left[-\sqrt{4Dt} + L_{\mathrm{l}}\sqrt{\pi} \right] \left[2L_{\mathrm{s}} \sqrt{\frac{\tau_{L_{\mathrm{s}}}}{4t}} \right] \\ &= \frac{cL_{\mathrm{s}}^2}{\pi} \left[-2 + \sqrt{\frac{\pi \tau_{L_{\mathrm{l}}}}{t}} \right] . \end{aligned} \tag{A.37}$$

The formula indicates the power law $\propto t^{-1/2}$, keeping in mind $t \ll \tau_{L_{\mathrm{l}}}$.

The power law $\propto t^{-1}$ for $\tau_{L_{\mathrm{l}}} \ll \tau_{L_{\mathrm{s}}} \ll t$, i.e. small $\tau_{L_{\mathrm{s,l}}}/t$, becomes visible directly after using the series expansion for small arguments on all exponential and error functions in Eq. (4.1):

$$C(t) \sim \frac{c}{\pi} \left[2L_{\mathrm{l}} \sqrt{\frac{\tau_{L_{\mathrm{l}}}}{4t}} \right] \left[2L_{\mathrm{s}} \sqrt{\frac{\tau_{L_{\mathrm{s}}}}{4t}} \right] \propto t^{-1} . \tag{A.38}$$

A.6.3 Residence time distribution for circular objects

At long times $t \gg \tau_R/\chi_1^2$ the exponential factor in the RTD for a circular geometry [Eq. (3.9)] decreases rapidly and only the term for $n = 1$ contributes significantly to the sum. Higher summands can be neglected, so that the functional behavior will follow Eq. (3.11).

For small times $t \ll \tau_R/\chi_1^2$, on the contrary, many terms will contribute to the sum, enabling to transform it into an integral. After substitution of $\xi \equiv \chi(n)$ Eq. (3.9) then reads

$$\psi(t) \approx \int \frac{\mathrm{d}\xi}{\chi'(n)} \, \xi \, \frac{J_0\left[\xi \left(1 - \Delta_R/R\right)\right]}{J_1\left(\xi\right)} \, \exp\left(-\xi^2 \frac{t}{\tau_R}\right) . \tag{A.39}$$

There is no explicit expression for the zeros of the Bessel-function of first order $\chi(n)$, which would be necessary to universally calculate the factor $\chi'(n) = \frac{\mathrm{d}\chi(n)}{\mathrm{d}n}$ arising from the substitution. However, for large arguments the zeros can be estimated from the asymptotic form $J_0(\chi) \sim (2/\pi\chi)^{1/2} \cos(\chi - \pi/4)$ [74] yielding $\chi(n) = (n + 3/4)\pi$ and a constant $\chi'(n) = \chi'$, which will be used in this approximation. To account for the time dependency a further substitution of $u^2 \equiv \xi^2 t/\tau_R$ is convenient

$$\psi(t) \approx \frac{2}{t} \int \frac{\mathrm{d}u}{\chi'} \, u \, \frac{J_0\left[u\sqrt{\frac{\tau_R}{t}} \left(1 - \frac{\Delta_R}{R}\right)\right]}{J_1\left(u\sqrt{\frac{\tau_R}{t}}\right)} \, \exp\left(-u^2\right) . \tag{A.40}$$

The exponential function is dominant in the integrand and only small u values will contribute to the integral. This allows to use a Taylor series with $u \approx 0$ on the Bessel-functions resulting in

$$\psi(t) \approx \frac{2}{t} \int \frac{\mathrm{d}u}{\chi'} \, u \, \left[\frac{2}{u} \sqrt{\frac{t}{\tau_R}} - \frac{u}{2} \sqrt{\frac{\tau_R}{t}} \left(1 - \frac{\Delta_R}{R}\right) \right] \exp\left(-u^2\right) . \tag{A.41}$$

The first summand is negligible, because the time regime $t \ll \tau_R / \chi_1^2$ is considered. The prefactor of the remaining expression

$$\psi(t) \approx \frac{1}{t} \sqrt{\frac{\tau_R}{t}} \int \frac{du}{\chi'} \left(\frac{\Delta_R}{R} - 1 \right) u^2 \exp\left(-u^2\right) \tag{A.42}$$

defines the power law $\propto t^{-3/2}$

A.6.4   Residence time distribution for rectangular objects

At small times $\tau_\Delta \ll t \ll \tau_{\lambda_{1,1}}$ a power law proportional to $t^{-3/2}$ arises in the RTD for rectangular objects. For such small residence times many summands in Eq. (4.4) add to the result, therefore it is legitimate to again transform the sum into an integral. Furthermore, the substitutions $u^2 = D\pi^2\mu^2 t/L_l^2$ and $v^2 = D\pi^2\nu^2 t/L_s$ are helpful in the further derivation. After some rearrangements Eq. (4.4) reads

$$\psi(t) \approx \frac{32}{(L_s + L_l)\pi^2 t} \tag{A.43}$$

$$\int_{\frac{\pi\sqrt{Dt}}{L_s}}^{\infty} \int_{\frac{\pi\sqrt{Dt}}{L_l}}^{\infty} dv\, du \left[\frac{\sin\left(\frac{u\Delta}{\sqrt{Dt}}\right)}{\frac{v}{\sqrt{Dt}}} + \frac{\sin\left(\frac{v\Delta}{\sqrt{Dt}}\right)}{\frac{u}{\sqrt{Dt}}} \right] \frac{u^2 + v^2}{u\,v} e^{-u^2 - v^2}. \tag{A.44}$$

The exponential function is the dominant expression here and only $u^2 + v^2 \leq 1$ contribute significantly to the result. Provided that $\max(u)=\max(v)=1$ a small-angle approximation yields $\sin(\Delta/\sqrt{Dt}) = \Delta/\sqrt{Dt}$ and therefore

$$\psi(t) \approx \frac{32\Delta}{(L_s + L_l)\pi^2 t} \tag{A.45}$$

$$\int_{\frac{\pi\sqrt{Dt}}{L_s}}^{\infty} \int_{\frac{\pi\sqrt{Dt}}{L_l}}^{\infty} dv\, du\, 2\, e^{-u^2 - v^2} + \frac{u^2}{v^2}\, e^{-u^2 - v^2} + \frac{v^2}{u^2}\, e^{-u^2 - v^2}. \tag{A.46}$$

This double integral consists of three types of integrals, which can be solved each by carefully considering the integration boundaries and functional behavior of the integrands:

$$\text{(I)} \int_{\frac{\pi\sqrt{Dt}}{L_{s,l}} = \frac{\pi t}{\tau_{L_{s,l}}}}^{\infty} dx\, x^2\, e^{-x^2}, \quad \text{(II)} \int_{\pi t/\tau_{L_{s,l}}}^{\infty} dx\, x^{-2}\, e^{-x^2}, \quad \text{(III)} \int_{\pi t/\tau_{L_{s,l}}}^{\infty} dx\, e^{-x^2} \tag{A.47}$$

The lower boundary in (I) tends to zero, because in the considered time regime $t \ll \tau_{L_{s,l}}$. Furthermore, the integrand decreases rapidly for small x, therefore it is legitimate to extend the integration limits to the well defined $\int_0^\infty dx\, x^2 \exp(x^2) = \sqrt{\pi}/4$. In (II) both terms decrease rapidly for $x > 1$ and for $x \leq 1$, u^{-2} increases strongly, while $\exp(-x^2)$ approaches one. As an approximation it is therefore valid to consider only $\int_{\pi t/\tau_{L_{s,l}}}^{\infty} dx\, x^{-2} = \left(\tau_{L_{s,l}}/\pi^2 t\right)^{1/2}$. Analogous to the previous arguments, in (III) the lower boundary tends to zero and the integral can be estimated via $\int_0^\infty \exp(-x^2) = \sqrt{\pi}/2$. Using this solutions, the original double integral can be solved consecutively, resulting in

$$\psi(t) \approx \frac{8\Delta}{(L_s + L_l)\pi^2 t} \left(2\pi + \sqrt{\frac{\tau_{L_s} + \tau_{L_l}}{\pi t}} \right), \tag{A.48}$$

which contains the predicted power law $\propto t^{-3/2}$.

At long times $\tau_{\lambda_{1,1}} \ll t$, the exponential function in Eq. (4.4) is crucial for the functional behavior. Only the summand with $\mu = \nu = 1$ contributes significantly to the sum, and the higher terms can be neglected. The remaining expression [Eq. (4.5)] describes the exponential decay in this time regime.

A.6.5 Interpeak time distribution for circular objects

In the ITD for a single circular object [Eq. (3.13)] two time regimes separated by τ_R can be identified. To deal with the short time regime $t \ll \tau_R$, the substitution of $u^2 \equiv \chi^2 \frac{t}{\tau_R}$ is useful

$$
\psi(t) = \frac{2}{\pi t} \int_0^\infty \mathrm{d}u \; u \; \exp\left(-u^2\right) \tag{A.49}
$$
$$
\frac{-J_0\left[u\sqrt{\frac{\tau_R}{t}}\left(1 + \frac{\Delta_R}{R}\right)\right] Y_0\left(u\sqrt{\frac{\tau_R}{t}}\right) + J_0\left(u\sqrt{\frac{\tau_R}{t}}\right) Y_0\left[u\sqrt{\frac{\tau_R}{t}}\left(1 + \frac{\Delta_R}{R}\right)\right]}{J_0^2\left(u\sqrt{\frac{\tau_R}{t}}\right) + Y_0^2\left(u\sqrt{\frac{\tau_R}{t}}\right)} .
$$

The exponential function limits significant values of the integral to small u. The arguments $u(t/\tau_R)^{-1/2}$ of the Bessel-functions of first $[J_0(.)]$ and second $[Y(.)]$ kind therefore become very large in this time regime and the asymptotic expansions for large arguments [74] $J_0(z) \sim (2/\pi z)^{1/2} \cos(z - \pi/4)$ and $Y_0(z) \sim (2/\pi z)^{1/2} \sin(z - \pi/4)$ can be employed. After several conversions using the addition theorems, the expression is reduced to

$$
\psi(t) \sim \frac{2}{\pi t \sqrt{1 - \Delta_R/R}} \int_0^\infty \mathrm{d}u \; u \exp\left(-u^2\right) \sin\left(u\sqrt{\frac{\tau_R}{t}} \frac{\Delta_R}{R}\right) . \tag{A.50}
$$

When solving the integral it directly devolves into the approximation in Eq. (3.14) used for fitting the short time regimes of ITDs.

In the long time regime $t \gg \tau_R$ the arguments in the Bessel-functions of Eq. (A.49) become very small, allowing to use the limiting forms for small arguments [74] $J_0(z) \sim 1$ and $Y_0 \sim 2\ln(z)/\pi$. After further transformations and approximations with respect to the time regime the expression is reduced to

$$
\psi(t) \approx \left(\frac{2}{\pi}\right)^2 \frac{\ln\left(1 + \Delta_R/R\right)}{t} \int_0^\infty \mathrm{d}u \; u \left[\left(\frac{2}{\pi}\right)^2 \ln^2\left(\sqrt{\frac{t}{\tau_R}}\right)\right]^{-1} \exp\left(-u^2\right) . \tag{A.51}
$$

Solving the integral yields Eq. (3.15) as the approximation for $t \gg \tau_R$.

Appendix B

Supplementary information

In this part of the appendix supplementary information on different aspects of the work is collected.

B.1 Calculating correlation functions from "on"-"off" time tables

If measurement signals are given as a table of "on" and "off" times, the calculation of the correlation function via fast fourier transformation would require a reconstruction of a corresponding discrete time series with steps dt:

```
t = 0:dt:max(table entries)
for each t
  if at least one table entry is in [t-dt,t]
    find the last table entry smaller t
    if it is of 'on'-type
      S(t):=1
    else
      S(t):=0
    end if
  else
    S(t):=S(t-dt)
  end if
end
```

Given this reconstructed signal Eq. (3.6) can be applied. However, the size of dt has to be chosen with care. If it is too large, peaks can be overlooked. If dt is chosen very small, runtime as well as memory load increase considerably.

A more convenient alternative is to define the peaks as $\Theta(t - t_{\text{on}}) - \Theta(t - t_{\text{off}})$ with t_{on} the beginning of the peak and t_{off} the end as well as the Heaviside jump function $\Theta(.)$. The full signal α is then given by

$$S^{\alpha}(t) = \sum_n \left[\Theta\left(t - t_{\text{on}}^{\alpha,n}\right) - \Theta\left(t - t_{\text{off}}^{\alpha,n}\right) \right] . \tag{B.1}$$

The correlation function between the signals α and β reads

$$C(\tau) = \frac{1}{T} \int_0^T dt \; S^\alpha(t) S^\beta(t+\tau) \tag{B.2}$$

$$= \frac{1}{T} \sum_{m,n} \int_0^T dt \; [\Theta(t - t_{\text{on}}^{\alpha,n}) - \Theta(t - t_{\text{off}}^{\alpha,n})][\Theta(t - (t_{\text{on}}^{\beta,m} + \tau)) - \Theta(t - (t_{\text{off}}^{\beta,m} + \tau))]$$

There are well defined conditions, whether and how two peaks from the signals α and β will contribute to the correlation. First the peak from β must not end before the corresponding peak from α has started and it must not start, if the other one already ended, see Fig. B.1 (a)-(b). If these conditions are met, the start of the correlating time interval is given by the larger of both t_{on} and the end by the smaller t_{off}, see Fig. B.1 (c)-(f). Calculation of the correlation function is therefore reduced to a comparison of start and end times

$$C(\tau) = \tag{B.3}$$

$$\frac{1}{T} \sum_{m,n} \begin{cases} \min\left(t_{\text{off}}^{\alpha,m}, t_{\text{off}}^{\beta,n} + \tau\right) - \max\left(t_{\text{on}}^{\alpha,m}, t_{\text{on}}^{\beta,n} + \tau\right) & \text{if} & t_{\text{off}}^{\beta,n} + \tau > t_{\text{on}}^{\alpha,m} \wedge \\ & & t_{\text{on}}^{\beta,n} + \tau < t_{\text{off}}^{\alpha,m}, \\ & 0 & \text{else}. \end{cases}$$

Clearly, for the autocorrelation α and β are the same signal.
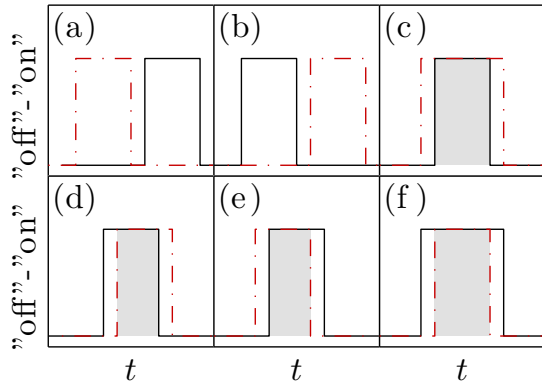
Figure B.1: Simplified overview of the six possible arrangements between peaks from signal α (solid line) and β (dash-dotted line). Only (c)-(f) will contribute to the correlation. The time interval relevant for correlation (shaded area) is restricted by the larger of the starting times and the smaller of the ending times.

B.2 Directional sensitivity of linear extended tip
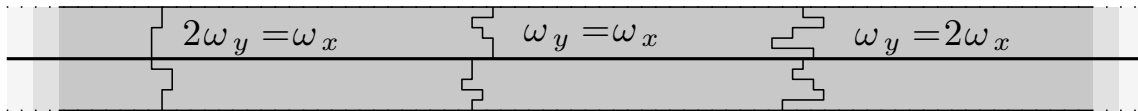
Figure B.2: Qualitative illustration of three diffusion paths ($2\omega_y = \omega_x$, $\omega_y = \omega_x$ and $\omega_y = 2\omega_x$) through the detection area (gray) of an infinite extended linear probe (bold line), which is aligned to the x-axis. Displacements parallel to the probe cannot change the signal.

B.3 Number of events in exponential time regime

Figure B.3: Percentage of events in time regime previous to the exponential decay depending on the object radius R. For the RTD $\Psi(t)$ from Eq. (3.9) has to be integrated over the time interval $[\Delta^2/D, \tau_R/\chi_1^2]$ (dash-dotted line) and for the ITD $\Psi(t)$ from Eq. (3.13) over the interval $[\tau_{max}, \tau_c]$ (dashed line).
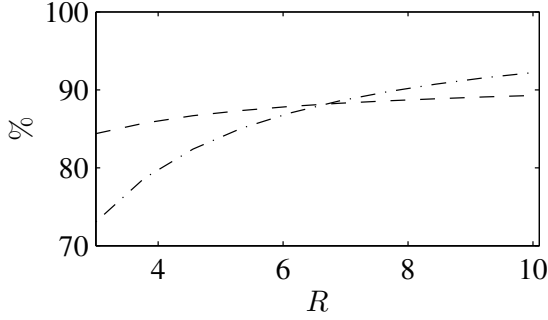
B.4 Determination of optimal tip length
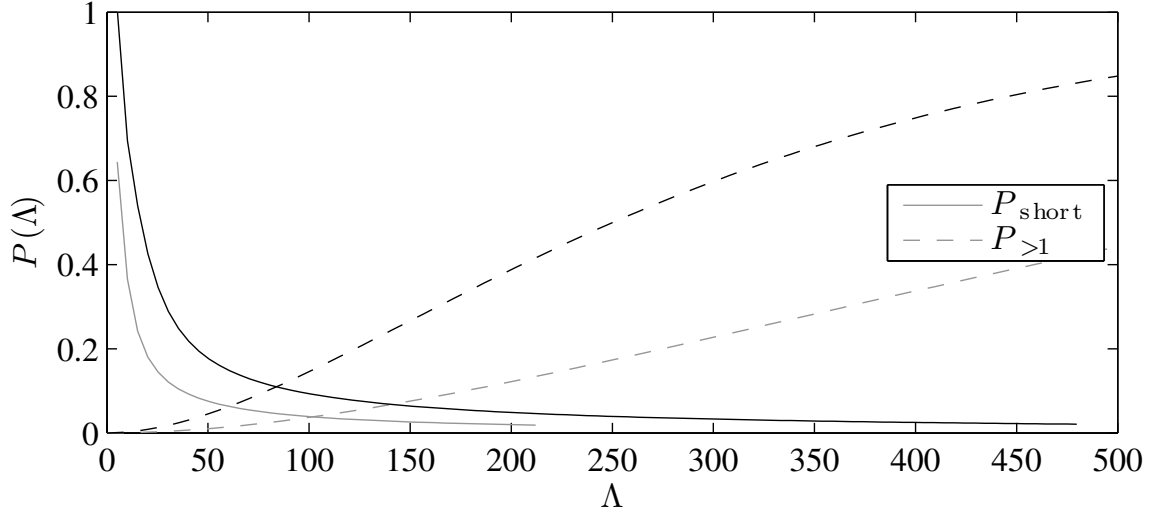
Figure B.4: Increasing probability to find more than one object in the detection area of a extended linear probe [Eq. (6.5), dashed lines] and decreasing probability to enter or leave the detection area through one of the short edges [Eq. (6.7), solid lines]. The intersection point indicates the most reasonable length for the detection area in Conf. A00-A02. Here $\Lambda = 100$ for $\bar{\gamma} = 0$ (gray lines) and $\Lambda = 80$ for $\bar{\gamma} = \pi/2$ (black lines) yield a linear probe length between, $l = 45$ and $l = 37.5$, respectively. Therefore, $l_{opt} = 41$ is defined as the best probe length.

Annotations: In case of a discrete grid $P_{L,in} \to (L-1)/(L+\Lambda-2)$ to avoid a double weighting of the vertices. For $\bar{\gamma} = \pi/2$ even at the optimal length there is a probability of 11% for the processes, which threaten the one-dimensional approach. In general, performance of this method will hence increases at lower coverages, where $P_{>1}$ decreases.

B.5 Event count in experimental data
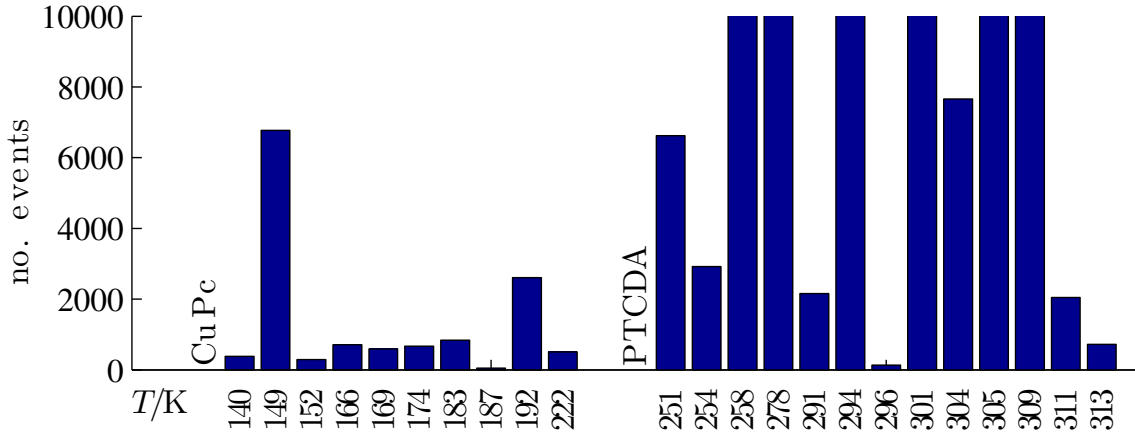
Figure B.5: Number of events contained in the available signals for CuPc and PTCDA at different temperatures. Peaks were extracted according to chapter 7.1. Most time series contain less than the recommended 10^4 events (compare chapter 3.4), but still show usable distributions of peak widths and distances. Only measurements at 187 K and 296 K have to be treated with reservations, because with 46 and 136 peaks they offer too little statistics for a meaningful evaluation.

B.6 Mean residence time for CuPc and PTCDA
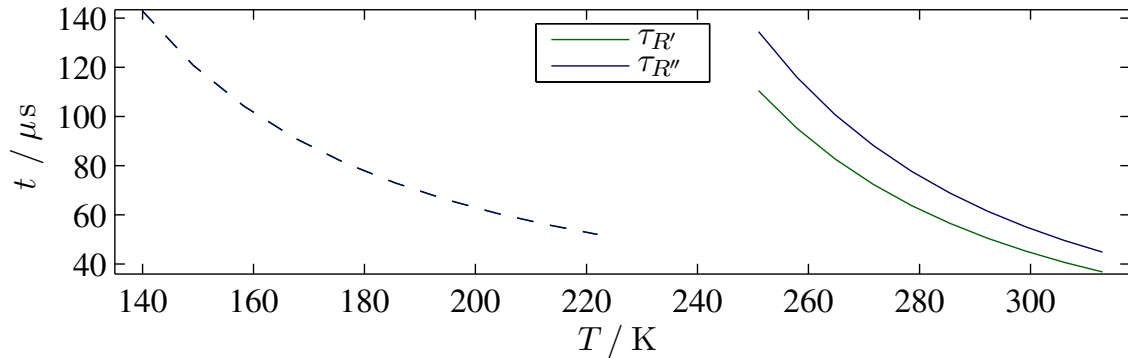
Figure B.6: The typical residence times $\tau_{R'}$ and $\tau_{R''}$ [with $D = \bar{D}_0 \exp(-E_\mathrm{a}/k_\mathrm{B}T)$] for PTCDA (solid lines) and CuPc (congruent dashed lines). In its respective temperature regime it is partially shorter for the PTCDA molecule than for CuPc.

B.7 Influence of threshold
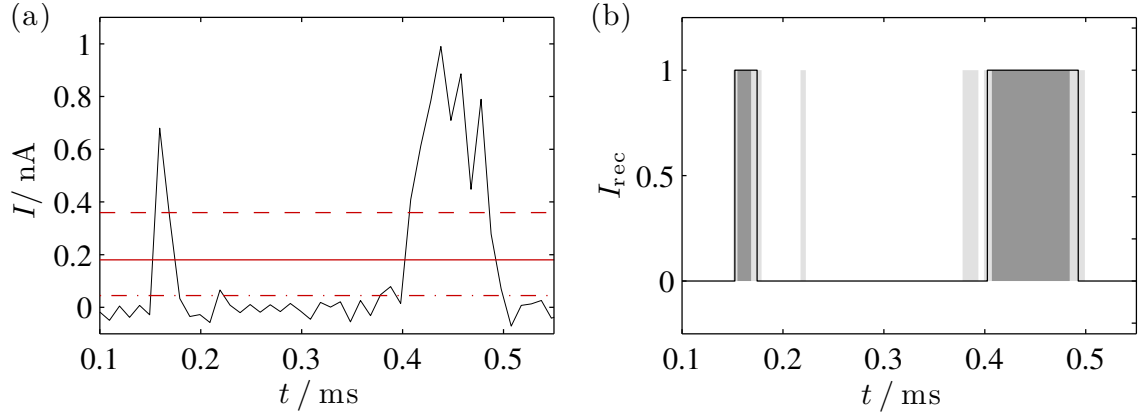
Figure B.7: (a) Excerpt of the signal in Fig. 7.1 with three different threshold values $I_c = 0.18$ nA (solid line), $2I_c$ (dashed line) and $0.25I_c$ (dash-dotted line). (b) The respective rectangular signal (solid line). With $0.25I_c$ peaks are widened and additional peaks are detected (light gray), with $2I_c$ the peak's widths is considerably reduced (dark gray). While peak widths are very sensitive to the threshold, for the interpeak intervals the difference is negligible.

B.8 Succession of experimental measurements

CuPc		PTCDA	
$T/$K	Date - Order	$T/$K	Date - Order
140	2009/04/15 B	251	2008/10/31 C
149	2009/04/15 G	254	2008/10/30 B
152	2009/04/15 A	258	2008/11/03 A
166	2009/04/15 C	278	2008/11/03 B
169	2009/04/15 D	291	2008/10/30 A
174	2009/04/15 E	294	2008/10/23 A
183	2009/08/26 A	296	2008/10/15 A
187	2009/04/16 A	301	2008/11/07 A
192	2009/08/26 B	304	2008/10/23 B
222	2009/04/15 F	305	2008/11/07 B
		309	2008/10/23 C
		311	2008/11/07 C
		313	2008/10/23 D

Table B.1: Dates and (alphabetical) order of the experimental measurements.

Appendix C

Simulated configurations

In this part of the appendix all simulation parameter sets used throughout this work are listed. A system of size $(1000 \times 1000)a$ with periodic boundary conditions was used and the Mersenne Twister ran 10^5 steps as warm up. If not stated elsewise, 10^5 peaks have been recorded.

C.1   Configurations with circular shaped molecules

C01

Geometry		Rates & stepsize	
R/a	5	w_{tr}	1
		a	1
θ_0	0.01	w_{rot}	—
		Δ_φ	—

C02

Geometry		Rates & stepsize	
R/a	10	w_{tr}	1
		a	1
θ_0	0.01	w_{rot}	—
		Δ_φ	—

C03

Geometry		Rates & stepsize	
R/a	1	w_{tr}	1
		a	1
θ_0	0.01	w_{rot}	—
		Δ_φ	—

C04

Geometry		Rates & stepsize	
R/a	2	w_{tr}	1
		a	1
θ_0	0.01	w_{rot}	—
		Δ_φ	—

C05

Geometry		Rates & stepsize	
R/a	3	w_{tr}	1
		a	1
θ_0	0.01	w_{rot}	—
		Δ_φ	—

C06

Geometry		Rates & stepsize	
R/a	4	w_{tr}	1
		a	1
θ_0	0.01	w_{rot}	—
		Δ_φ	—

C.2   Configurations with rectangular shaped molecules

C.2.1   Isotropic translational diffusion only

R01

Geometry		Rates & stepsize	
L_s/a	10	w_{tr}	1
L_l/a	10	a	1
θ_0	0.01	w_{rot}	—
		Δ_φ	—

R02

Geometry		Rates & stepsize	
L_s/a	10	w_{tr}	1
L_l/a	20	a	1
θ_0	0.01	w_{rot}	—
		Δ_φ	—

R03

Geometry		Rates & stepsize	
L_s/a	10	w_{tr}	1
L_l/a	30	a	1
θ_0	0.01	w_{rot}	—
		Δ_φ	—

R04

Geometry		Rates & stepsize	
L_s/a	10	w_{tr}	1
L_l/a	40	a	1
θ_0	0.01	w_{rot}	—
		Δ_φ	—

R05

Geometry		Rates & stepsize	
L_s/a	10	w_{tr}	1
L_l/a	50	a	1
θ_0	0.01	w_{rot}	—
		Δ_φ	—

C.2.2   Mixed isotropic translational and rotational diffusion

M00

Geometry		Rates & stepsize	
L_s/a	5	w_{tr}	0.25
L_l/a	10	a	1
θ_0	0.01	w_{rot}	0.01
		Δ_φ	$2\pi/10$

M02

Geometry		Rates & stepsize	
L_s/a	5	w_{tr}	0.25
L_l/a	10	a	1
θ_0	0.01	w_{rot}	0.40
		Δ_φ	$2\pi/10$

M03

Geometry		Rates & stepsize	
L_s/a	5	w_{tr}	0.25
L_l/a	10	a	1
θ_0	0.01	w_{rot}	3.60
		Δ_φ	$2\pi/10$

M04

Geometry		Rates & stepsize	
L_s/a	5	w_{tr}	0.25
L_l/a	5	a	1
θ_0	0.01	w_{rot}	3.60
		Δ_φ	$2\pi/10$

C.2.3 Anisotropic translational diffusion

A00

Geometry		Rates & stepsize	
L_s/a	5	$w_{\text{tr},x}$	0.50
L_l/a	10	a_x	1
θ_0	0.01	$w_{\text{tr},y}$	0.50
l		a_y	1

A01

Geometry		Rates & stepsize	
L_s/a	5	$w_{\text{tr},x}$	0.50
L_l/a	10	a_x	1
θ_0	0.01	$w_{\text{tr},y}$	0.20
l		a_y	1

A02

Geometry		Rates & stepsize	
L_s/a	5	$w_{\text{tr},x}$	0.50
L_l/a	10	a_x	1
θ_0	0.01	$w_{\text{tr},y}$	0.02
l		a_y	1

Bibliography

[†] S. Hahne, J. Ikonomov, M. Sokolowski, P. Maass. *Determining Molecule Diffusion Coefficients on Surfaces from a Locally Fixed Probe: Analysis of Signal Fluctuations.* Phys. Rev. B **87** 085409 (2013)

[‡] S. Hahne, P. Maass. *Diffusion Coefficients from Signal Fluctuations: Influence of Molecular Shape and Rotational Diffusion.* J. Phys. Chem. A **118** 2237 (2014)

[1] C. H. Kim, G. Qi, K. Dahlberg, W. Li. *Strontium-Doped Perovskites Rival Platinum Catalysts for Treating NOx in Simulated Diesel Exhaust.* Science **327**, 1624 (2010).

[2] G. C. Bond, D. T. Thompson. *Catalysis by Gold.* Catal. Rev. **41**, 319 (1999).

[3] N. Toshima, T. Yonezawa. *Bimetallic Nanoparticles-Novel Materials for Chemical and Physical Applications.* New J. Chem. **22**, 1179 (1998).

[4] G. E. Moore. *Cramming More Components onto Integrated Circuits.* Electronics **38**, 114 (1965).

[5] C. D. Dimitrakopoulos, P. R. L. Malenfant. *Organic Thin Film Transistors for Large Area Electronics.* Adv. Mater. **14**, 99 (2002).

[6] C. Bombis, F. Ample, L. Lafferentz, H. Yu, S. Hecht, C. Joachim, L. Grill. *Single Molecular Wires Connecting Metallic and Insulating Surface Areas.* Angew. Chem. Int. Edit. **48**, 9966 (2009).

[7] C. Joachim, M. A. Ratner. *Molecular Electronics: Some Views on Transport Junctions and Beyond.* Proc. Natl. Acad. Sci. **102**, 8801 (2005).

[8] C. Joachim, J. K. Gimzewski, A. Aviram. *Electronics Using Hybrid-Molecular and Mono-Molecular Devices.* Nature **408**, 541 (2000).

[9] P. Rahe, M. Kittelmann, J.L. Neff, M. Nimmrich, M. Reichling, P. Maass, A. Kühnle. *Tuning Molecular Self-Assembly on Bulk Insulator Surfaces by Anchoring of the Organic Building Blocks.* Adv. Mater. **25**, 3948 (2013).

[10] G. Hlawacek, C. Teichert. *Nucleation and Growth of Thin Films of Rod-Like Conjugated Molecules.* J. Phys. Condens. Mat. **25**, 143202 (2013).

[11] S. Kowarik, A. Gerlach, F. Schreiber. *Organic Molecular Beam Deposition: Fundamentals, Growth Dynamics, and in situ Studies.* J. Phys.: Condens. Mat. **20**, 184005 (2008).

[12] A. Kühnle. *Self-Assembly of Organic Molecules at Metal Surfaces.* Curr. Opin. Colloid Interface Sci. **14**, 157 (2009).

[13] P. Clancy. *Application of Molecular Simulation Techniques to the Study of Factors Affecting the Thin-Film Morphology of Small-Molecule Organic Semiconductors.* Chem. Mater. **23**, 522 (2011).

[14] K. Oura, M. Katayama, V. G. Lifshits, A. A. Saranin, A. V. Zotov. *Surface Science.* Springer (2003).

[15] M. Einax, W. Dieterich, P. Maass. *Binding Energies between Unlike Atoms Determined from Island Densities.* J. Appl. Phys. **105**, 054312 (2009).

[16] R. Brown. *XXVII. A Brief Account of Microscopical Observations Made in the Months of June, July and August 1827, on the Particles Contained in the Pollen of Plants; and on the General Existence of Active Molecules in Organic and Inorganic Bodies.* Philos. Mag. **4**, 161 (1828).

[17] R. Brown. *XXIV. Additional Remarks on Active Molecules.* Philos. Mag. **6**, 161 (1829).

[18] A. Fick. *Ueber Diffusion.* Ann. Phys. **170**, 59 (1855).

[19] J. V. Barth. *Transport of Adsorbates at Metal Surfaces: From Thermal Migration to Hot Precursors.* Surf. Sci. Rep. **40**, 75 (2000).

[20] E. W. Mülller. *Weitere Beobachtungen mit dem Feldelektronenmikroskop.* Zeits. f. Physik **108**, 668 (1938).

[21] R. Gomer. *Field Emission and Field Ionization.* Harvard University Press (1961).

[22] R Gomer. *Current Fluctuations from Small Regions of Adsorbate Covered Field Emitters - Method for Determining Diffusion-Coefficients on Single-Crystal Planes.* Surf. Sci. **38**, 373 (1973).

[23] E. W. Müller, T. T. Tsong. *Field Ion Microscopy.* American Elsevier Publishing Company (1969).

[24] R. Viswanathan, D. R. Burgess, P. C. Stair, E. Weitz. *Laser Flash Desorption of CO from Clean Copper Surfaces.* J. Vac. Sci. Technol. **20**, 605 (1982).

[25] J. Crank. *The Mathematics of Diffusion.* Oxford University Press (1975).

[26] G. Binnig, H. Rohrer, C. Gerber, E. Weibel. *Tunneling Through a Controllable Vacuum Gap.* Appl. Phys. Lett. **40**, 178 (1982).

[27] G. Binnig, C. F. Quate, C. Gerber. *Atomic Force Microscope.* Phys. Rev Lett. **56**, 930 (1986).

[28] M. Heidernätsch, M. Bauer, G. Radons. *Characterizing N-dimensional Anisotropic Brownian Motion by the Distribution of Diffusivities.* J. Chem. Phys. **139**, 184105 (2013).

[29] H. Brune, G. S. Bales, J. Jacobsen, C. Boragno, K. Kern. *Measuring Surface Diffusion from Nucleation Island Densities.* Phys. Rev. B **60**, 5991 (1999).

[30] J. W. Evans, P. A. Thiel, M. C. Bartelt. *Morphological Evolution during Epitaxial Thin Film Growth: Formation of 2D Islands and 3D Mounds.* Surf. Sci. Rep. **61**, 1 (2006).

[31] M. Einax, S. Ziehm, W. Dieterich, P. Maass. *Scaling of Island Densities in Submonolayer Growth of Binary Alloys.* Phys. Rev. Lett. **99**, 016106 (2007).

[32] G. Schitter, M. J. Rost. *Scanning Probe Microscopy at Video-Rate.* Mater. Today **11**, 40 (2008).

[33] B. S. Swartzentruber. *Direct Measurement of Surface Diffusion Using Atom-Tracking Scanning Tunneling Microscopy.* Phys. Rev. Lett. **76**, 459 (1996).

[34] S. Berner, M. Brunner, L. Ramoino, H. Suzuki, H. J. Guntherodt, T. A. Jung. *Time Evolution Analysis of a 2D Solid-Gas Equilibrium: A Model System for Molecular Adsorption and Diffusion.* Chem. Phys. Lett. **348**, 175 (2001).

[35] S. Berner, M. de Wild, L. Ramoino, S. Ivan, A. Baratoff, H. J. Guntherodt, H. Suzuki, D. Schlettwein, T. A. Jung. *Adsorption and Two-Dimensional Phases of a Large Polar Molecule: Sub-Phthalocyanine on Ag(111).* Phys. Rev. B **68**, 115410 (2003).

[36] A. D. L. Humphris, B. Zhao, D. Catto, J. P. Howard-Knight, P. Kohli, J. K. Hobbs. *High Speed Nano-Metrology.* Rev. Sci. Instrum. **82**, 043710 (2011).

[37] M. Tringides, M. Gupalo, Q. Li, X. Wang. *Equilibrium Versus Non-Equilibrium Surface Diffusion Measurements.* **519**, 309 (1999).

[38] M. Sumetskii, A. A. Kornyshev. *Noise in STM Due to Atoms Moving in the Tunneling Space.* Phys. Rev. B **48**, 17493 (1993).

[39] J. Ikonomov, P. Bach, R. Merkel, M. Sokolowski. *Surface Diffusion Constants of Large Organic Molecules Determined from their Residence Times under a Scanning Tunneling Microscope Tip.* Phys. Rev. B **81**, 161412 (2010).

[40] J. Lagoute, K. Kanisawa, S. Fölsch. *Manipulation and Adsorption-Site Mapping of Single Pentacene Molecules on Cu(111).* Phys. Rev. B **70**, 245415 (2004).

[41] Q. Chen, A. J. McDowall, N. V. Richardson. *Ordered Structures of Tetracene and Pentacene on Cu(110) Surfaces.* Langmuir **19**, 10164 (2003).

[42] E. Le Moal, M. Müller, O. Bauer, M. Sokolowski. *Stable and Metastable Phases of PTCDA on Epitaxial NaCl Films on Ag(100).* Phys. Rev. B **82**, 045301 (2010).

[43] M. Fendrich, T. Wagner, M. Stöhr, R. Möller. *Hindered Rotation of a Copper Phthalocyanine Molecule on C_{60}: Experiments and Molecular Mechanics Calculations.* Phys. Rev. B **73**, 115433 (2006).

[44] M. Stöhr, Th. Wagner, M. Gabriel, B. Weyers, R. Möller. *Direct Observation of Hindered Eccentric Rotation of an Individual Molecule: Cu-Phthalocyanine on C_{60}.* Phys. Rev. B **65**, 033404 (2001).

[45] L. J. Lauhon, W. Ho. *Single Molecule Thermal Rotation and Diffusion: Acetylene on Cu(001).* J. Chem. Phys. **111**, 5633 (1999).

[46] T. Sonnleitner, I. Swart, N. Pavlicek, A. Pöllmann, J. Repp. *Molecular Symmetry Governs Surface Diffusion.* Phys. Rev. Lett. **107**, 186103 (2011).

[47] E. Ganz, S. K. Theiss, I.-S. Hwang, J. Golovchenko. *Direct Measurement of Diffusion by Hot Tunneling Microscopy - Activation Energy, Anisotropy, and Long Jumps.* Phys. Rev. Lett. **68**, 1567 (1992).

[48] R Otero, F Hummelink, F Sato, SB Legoas, P Thostrup, E Laegsgaard, I Stensgaard, DS Galvao, F Besenbacher. *Lock-and-Key Effect in the Surface Diffusion of Large Organic Molecules Probed by STM.* Nat. Mater. **3**, 779 (2004).

[49] M. Schirber. *Giant Diffusion on Magnetic Conveyor.* Phys. Rev. Focus **26**, 22 (2010).

[50] J. Seibel, O. Allemann, J. S. Siegel, K.-H. Ernst. *Chiral Conflict among Different Helicenes Suppresses Formation of One Enantiomorph in 2D Crystallization.* J. Am. Chem. Soc. **135**, 7434 (2013).

[51] L. Gross, K. H. Rieder, F. Moresco, S. M. Stojkovic, A. Gourdon, C. Joachim. *Trapping and Moving Metal Atoms with a Six-Leg Molecule.* Nat. Mater. **4**, 892 (2005).

[52] A. Mugarza, R. Robles, C. Krull, R. Korytár, N. Lorente, P. Gambardella. *Electronic and Magnetic Properties of Molecule-Metal Interfaces: Transition-Metal Phthalocyanines Adsorbed on Ag(100).* Phys. Rev. B **85**, 155437 (2012).

[53] L. Gross, F. Mohn, N. Moll, P. Liljeroth, G. Meyer. *The Chemical Structure of a Molecule Resolved by Atomic Force Microscopy.* Science **325**, 1110 (2009).

[54] L. Wan, K. Itaya. *In Situ Scanning Tunneling Microscopy of Benzene, Naphthalene, and Anthracene Adsorbed on Cu(111) in Solution.* Langmuir **13**, 7173 (1997).

[55] D. V. Potapenko, N. J. Choi, R. M. Osgood. *Adsorption Geometry of Anthracene and 4-Bromobiphenyl on TiO2(110) Surfaces.* J. Phys. Chem. C **114**, 19419 (2010).

[56] A. Paulheim, M. Muller, C. Marquardt, M. Sokolowski. *Fluorescence Spectroscopy of PTCDA Molecules on the KCl(100) Surface in the Limit of Low Coverages: Site Selection and Diffusion.* Phys. Chem. Chem. Phys. **15**, 4906 (2013).

[57] M. Sokolowski, Insitut für Physikalische und Theoretische Chemie, Universität Bonn, Wegelerstraße 12, 53115 Bonn, Germany.
The author thanks Prof. Sokolowski for providing the raw measurement data of Copperphthalocyanine diffusing on Ag(100) @ $T \in [140\,\mathrm{K}, 222\,\mathrm{K}]$ and PTCDA diffusing on Ag(100) @ $T \in [251\,\mathrm{K}, 313\,\mathrm{K}]$, which were previously published in [39].

[58] M. Hanwell, D. Curtis, D. Lonie, T. Vandermeersch, E. Zurek, G. Hutchison. *Avogadro: An Advanced Semantic Chemical Editor, Visualization, and Analysis Platform.* J. Cheminform. **4**, 17 (2012).

[59] E. Artacho, J. M. Cela, J. Gale, A. García, J. Junquera, R. M. Martin, P. Ordejón, D. Sánchez-Portal, J. M. Soler. *Siesta web page.* http://departments.icmab.es/leem/siesta/ (2014). Retrieved 2014-05-24.

[60] J. Izquierdo, A. Vega, L. C. Balbás, Daniel Sánchez-Portal, Javier Junquera, Emilio Artacho, Jose M. Soler, Pablo Ordejón. *Systematic Ab Initio Study of the Electronic and Magnetic Properties of Different Pure and Mixed Iron Systems.* Phys. Rev. B **61**, 13639 (2000).

[61] K. A. Fichthorn, W. H. Weinberg. *Theoretical Foundations of Dynamic Monte-Carlo Simulations.* J. Chem. Phys. **95**, 1090 (1991).

[62] A.P.J. Jansen. *An Introduction to Monte Carlo Simulations of Surface Reactions* (2003). arXiv:cond-mat/0303028 [cond-mat.stat-mech].

[63] The C++ Resources Network. *Reference - C++ Reference.* http://www.cplusplus.com/reference/ (2013). Retrieved 2014-03-03.

[64] M. Matsumoto, T. Nishimura. *Mersenne Twister: A 623-dimensionally Equidistributed Uniform Pseudo-random Number Generator.* ACM Trans. Model. Comput. Simul. **8**, 3 (1998).

[65] ISO/IEC 19505-1:2012. *Unified Modeling Language - Part 1: Infrastructure.* (2012).

[66] J. Tersoff, D. R. Hamann. *Theory and Application for the Scanning Tunneling Microscope.* Phys. Rev. Lett. **50**, 1998 (1983).

[67] C. B. Lang, N. Pucker. *Mathematische Methoden in der Physik.* Elsevier (2005).

[68] J. W. Cooley, J. W. Tukey. *An Algorithm for the Machine Calculation of Complex Fourier Series.* Math. Comput. **19**, 29 (1965).

[69] K. Levenberg. *A Method for the Solution of Certain Problems in Least Squares.* Quart. Appl. Math. **2**, 164 (1944).

[70] D. Marquardt. *An Algorithm for Least-Squares Estimation of Nonlinear Parameters.* SIAM J. Appl. Math. **11**, 431 (1963).

[71] S. Goldstein. *Some Two-Dimensional Diffusion Problems with Circular Symmetry.* Proc. Lond. Math. Soc. **34**, 51 (1932).

[72] S. Redner. *A Guide to First-Passage Processes.* Cambride University Press (2001).

[73] M. Einax, M. Dierl, P. Maass. *Verfahren zur Erstellung von Grauwertstatistiken in der digitalen Bildbearbeitung mit maximaler statistischer Genauigkeit (DE102011104732A1).* https://depatisnet.dpma.de (2011). Retrieved 2014-02-07.

[74] M. Abramowitz, I. A. Stegun. *Handbook of Mathematical Functions With Formulas, Graphs, and Mathematical Tables.* National Bureau of Standards (1964).

[75] M. Sumetskii, A. A. Kornyshev, U. Stimming. *Adatom Diffusion Characteristics from STM Noise: Theory.* Surf. Sci. **307**, 23 (1994).

[76] S. Chandrasekhar. *Stochastic Problems in Physics and Astronomy.* Rev. Mod. Phys. **15**, 1 (1943).

[77] H. Risken. *The Fokker-Planck Equation.* Springer (1989).

[78] F. Bornemann, D. Laurie, S. Wagon, J. Waldvogel. *Vom Lösen Numerischer Probleme.* Springer (2006).

[79] W. Cai, F. Pang, J. Wang, H. Liu, X. J. Liang, Q. K. Xue, D. M. Chen. *Ultrahigh Vacuum, Variable Temperature, Dual Scanning Tunneling Microscope System Operating under High Magnetic Field.* Rev. Sci. Instrum. **78**, 065108 (2007).

[80] A. Roychowdhury, M. A. Gubrud, R. Dana, J. R. Anderson, C. J. Lobb, F. C. Wellstood, M. Dreyer. *A 30 mK, 13.5 T Scanning Tunneling Microscope with Two Independent Tips.* Rev. Sci. Instrum. **85**, 043706 (2014).

[81] P. I. Chang, P. Huang, J. Maeng, S. B. Andersson. *Local Raster Scanning for High-Speed Imaging of Biopolymers in Atomic Force Microscopy.* Rev. Sci. Instrum. **82**, 063703 (2011).

[82] A. C. Mayer, R. Ruiz, H. Zhou, R. L. Headrick, A. Kazimirov, G. G. Malliaras. *Growth Dynamics of Pentacene Thin Films: Real-Time Synchrotron X-ray Scattering Study.* Phys. Rev. B **73**, 205307 (2006).

[83] M. Fendrich, J. Krug. *Ehrlich-Schwoebel Effect for Organic Molecules: Direct Calculation of the Step-Edge Barrier Using Empirical Potentials.* Phys. Rev. B **76**, 121302 (2007).

[84] K. Gl. *Highly Ordered Structures and Submolecular Scanning Tunnelling Microscopy Contrast of {PTCDA} and DM-PBDCI Monolayers on Ag(111) and Ag(110).* Surf. Sci. **405**, 1 (1998).

[85] During discussions Mr. Sokolowski pointed out, that short peaks close to the resolution limit of $4\mu s$ should be handled with reservations, because they might be affected by experimental errors.

[86] Y. Terada, S. Yoshida, O. Takeuchi, H. Shigekawa. *Laser-Combined Scanning Tunnelling Microscopy for Probing Ultrafast Transient Dynamics.* J. Phys. Cond. Matter **22**, 264008 (2010).

[87] M. Anwar, I. Rousso. *Atomic Force Microscopy with Time Resolution of Microseconds.* Appl. Phys. Lett. **86**, 014101 (2005).

[88] G.L. Kellogg. *Field Ion Microscope Studies of Single-Atom Surface Diffusion and Cluster Nucleation on Metal Surfaces.* Surf. Sci. Rep. **21**, 1 (1994).

[89] R. Scott Rowland, R. Taylor. *Intermolecular Nonbonded Contact Distances in Organic Crystal Structures: Comparison with Distances Expected from van der Waals Radii.* J. Phys. Chem. **100**, 7384–7391 (1996).

[90] I. V. Lebedeva, A. A. Knizhnik, A. M. Popov, O. V. Ershova, Y. E. Lozovik, B. V. Potapkin. *Diffusion and Drift of Graphene Flake on Graphite Surface.* J. Chem. Phys. **134**, 104505 (2011).

[91] A. Kusumi, C. Nakada, K. Ritchie, K. Murase, K. Suzuki, H. Murakoshi, R. S. Kasai, J. Kondo, T. Fujiwara. *Paradigm Shift of the Plasma Membrane Concept from the Two-Dimensional Continuum Fluid to the Partitioned Fluid: High-Speed Single-Molecule Tracking of Membrane Molecules.* Annu. Rev. Bioph. Biom. **34**, 351 (2005).

[92] G. Zumofen, J. Hohlbein, C. G. Hübner. *Recurrence and Photon Statistics in Fluorescence Fluctuation Spectroscopy.* Phys. Rev. Lett. **93**, 260601 (2004).

[93] E. P. Petrov, P. Schwille. *State of the Art and Novel Trends in Fluorescence Correlation Spectroscopy.* Springer (2008).

[94] T. Motegi, H. Nabika, K. Murakoshi. *Single-Molecule Observations for Determining the Orientation and Diffusivity of Dye Molecules in Lipid Bilayers.* Phys. Chem. Chem. Phys. **15**, 12895 (2013).

[95] K. Steger, S. Bollmann, F. Noe, S. Doose. *Systematic Evaluation of Fluorescence Correlation Spectroscopy Data Analysis on the Nanosecond Time Scale.* Phys. Chem. Chem. Phys. **15**, 10435 (2013).

[96] G.N. Watson. *A Treatise on the Theory of Bessel Functions.* Cambridge University Press (1922).

[97] D. Gilbarg, N. S. Trudinger. *Elliptic Partial Differential Equations of Second Order.* Springer (1998).

[98] B. Davies. *Integral Transforms and their Applications.* Springer (1978).